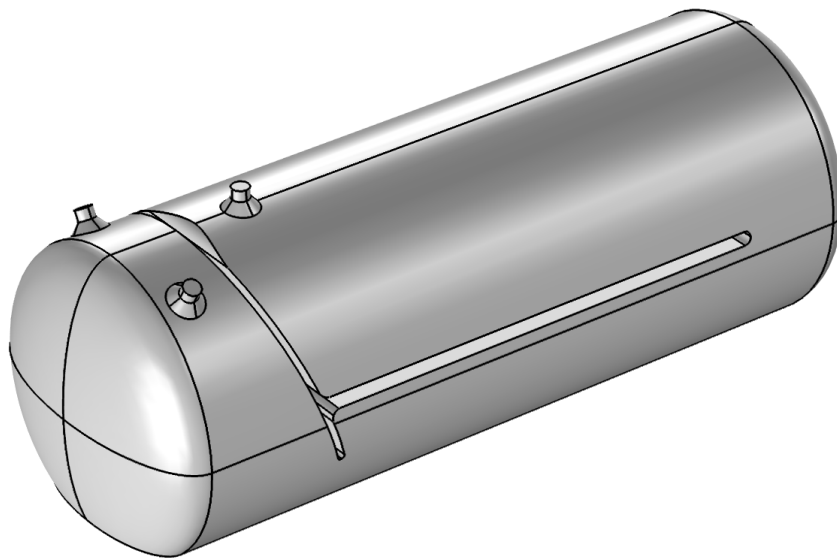


Feasibility Study of a Solids Separator Tank for Water Based Drilling Fluids

Cuttings separation by gravitational settling and pressure filtration

R. Özdemir

Faculty of Civil Engineering & Geosciences



Technical University of Delft

FACULTY OF CIVIL ENGINEERING AND GEOSCIENCES

Feasibility Study of a Solids Separator Tank for Water Based Drilling Fluids

Cuttings separation by gravitational settling and pressure filtration

By

R. Özdemir

in partial fulfilment of the requirements for the degree of

Master of Science

In Civil Engineering

at Delft University of Technology (TU Delft)
Faculty of Civil Engineering and Geosciences (CiTG)
Department of Geoscience & Engineering

to be defended publicly on Wednesday January 18, 2017

Author

Rahman Özdemir, BSc
4103998

Thesis committee

Supervisor	:	Dr. ir. A. Askarinejad	TU Delft, CiTG
Thesis committee	:	Prof. Dr. ir. C. van Rhee	TU Delft, 3ME
	:	Dr. ir. A.M. Talmon	TU Delft, 3ME
	:	Ir. R. El Boubsi	Huisman Well Technology BV
	:	Dr. ir. T. Bakker	Huisman Well Technology BV



An electronic version of this thesis is available at <http://repository.tudelft.nl/>.

Preface

This thesis completes my Master of Science in Civil Engineering at Delft University of Technology. For this thesis a research project is carried out on behalf of Huisman Well Equipment and in collaboration with the Geoscience & engineering and Offshore & Dredging engineering departments of the TU Delft. The thesis work is carried out in eleven months at the research and development department of Huisman equipment in Schiedam, the Netherlands. During this period several experiments have been performed in the laboratories of the Faculty of Civil Engineering and Geosciences at TU Delft.

I would like to thank the my graduation committee for their time invested, continuous constructive feedback and guidance throughout the project. Furthermore, many thanks to Rachid El Boubsi for the inspiring talks regarding the project and extensive feedback, Arno Talmon for the theoretical support and guidance, Cees van Rhee for the valuable feedback and Amin Askarinejad for the constructive meetings.

I would also like to express my gratitude to the lab technicians, Arno Mulder from the Geo-lab and Armand Middeldorp and Mohammed Jafar from the Fluid Mechanics lab. Also special thanks to Anton van Halteren (Well Engineering Partners) for providing the bentonite and Xanthan gum for the experiments.

And finally I would like to thank my friends and family who supported me throughout my entire study.

Rahman Özdemir
Delft, 4 January 2017

Abstract

The pressure on the oil and gas market has challenged drilling companies to develop new techniques to reduce their production costs. When a new well is drilled, a substantial expense is formed by the drilling fluid treatment process. During this process cuttings are removed from the drilling fluid to enable recycling of the drilling fluid. To innovate the treatment process and save on the costs, a feasibility study is carried out for a new cuttings removal method. The studied method involves the separation of cuttings from the drilling fluid by gravitational settling and by pressure filtration inside a pressurized tank.

To understand the effects and effectiveness of cuttings removal by gravitational settling in settling tanks, calculations are performed with Camp's ideal horizontal settling tank model. The results showed a first approximation of the achievable separation efficiency and the effects of various fluid parameters. The predicted separation efficiency was promising however did not satisfy the drilling fluid treatment requirements. As shown by the calculations, enhancements were possible if the drilling fluid viscosity could be reduced throughout the gravitational settling process.

Based on a literature review, vibrations were chosen as a method to reduce the drilling fluid viscosity. Experiments with vertical and horizontal vibrations are performed to study the obtainable viscosity reductions. The results were promising showing viscosity reductions of up to 80%, which could improve the separation efficiency of gravitational settling significantly. Additionally, pressure filtration experiments were carried out to obtain an indication of the applicability and separation efficiency of this separation method. The pressure filtration method was aimed to separate the fine particles from the drilling fluid, however the experiment results showed that this method was not feasible. The drilling fluid was clogging the filter medium instantaneously preventing filtration.

Finally, the information obtained from the calculations and experiments is combined in 2D and 3D simulations to evaluate the feasibility of the new treatment method. Using the finite element method software COMSOL, multiple 2D simulations are carried out to select an effective settling tank design. The selected tank design is then further evaluated using 3D simulations. The tank efficiency is evaluated for multiple parameters including different inflow rates and cutting sizes. The removal ratios obtained from the simulations provide an indication of the achievable separation efficiency by gravitational settling and the effectiveness of the vibrations. While promising, the results showed that complete separation of the fine cuttings (< 1mm) is not possible by only applying gravitational settling in the considered cases. Since pressure filtration was found not feasible to separate the fine cuttings, another complementary separation technique is necessary to meet the drilling fluid treatment separation requirements.

The application of the pressurized gravitational settling tank stays challenging. Further research is necessary to validate the simulation results and verify the applicability of vibrations inside a pressurized tank. Further development and optimization of the settling tank design is also recommended to increase the separation efficiency, while reducing the overall tank complexity.

Table of contents

PREFACE	5
ABSTRACT	7
TABLE OF CONTENTS	9
ABBREVIATIONS	11
NOMENCLATURE	13
LIST OF FIGURES	15
LIST OF TABLES	17
1. INTRODUCTION	19
1.1. BACKGROUND	19
1.2. PROBLEM DESCRIPTION	20
1.3. PROJECT OBJECTIVE	20
1.4. THESIS OUTLINE	20
2. THEORETICAL BACKGROUND	21
2.1. THE DRILLING PROCESS	21
2.2. THE DRILLING FLUIDS	22
2.2.1. Particle size distribution of solids in drilling fluid	22
2.2.2. Rheology of the drilling fluid	23
2.3. THE MUD TREATMENT SYSTEM	24
2.4. SETTLING OF PARTICLES	26
2.4.1. Single particle settling velocity	26
2.4.2. Influence of particle shape	28
2.4.3. Influence of particle concentration	28
2.4.4. Influence of particle size distribution	29
2.4.5. Influence of clay particles	29
2.4.6. Influence of turbulence	31
2.4.7. Influence of temperature and pressure	31
2.5. INFLUENCE OF VIBRATIONS ON NON-NEWTONIAN DRILLING FLUIDS	32
2.6. SETTLING IN HORIZONTAL TANKS	33
2.6.1. Unstable flow conditions	33
2.6.2. Resuspension	33
2.6.3. Flocculation	34
2.7. FILTRATION	34
3. PRELIMINARY CALCULATIONS	36
3.1. IDEAL HORIZONTAL SETTLING TANK MODEL	36
3.2. INPUT PARAMETERS	37
3.3. RESULTS OF PRELIMINARY CALCULATIONS	38
3.3.1. Differences between different particle settling models	38
3.3.2. The effect of particle concentration on settling	39
3.3.3. The effect of flow rate on settling	40
3.3.4. The effect of viscosity on settling	41
3.3.5. Others results	42
3.4. CHAPTER CONCLUSION	42
4. EXPERIMENTS	43
4.1. TEST SAMPLES AND PREPARATION	43
4.1.1. Sample composition and characteristics	43
4.1.2. Sample preparation and storage	44
4.1.3. Replacement for the fine cuttings	44
4.2. TEST SETUP AND TEST PROCEDURE	45
4.2.4. Vibration setups	45
4.2.5. Pressure filtration	47
4.2.6. Fann viscometer calibration	49
4.3. EXPERIMENT RESULTS	49

4.3.7.	Vibration results	49
4.3.8.	Pressure filtration experiment results	61
4.4.	CHAPTER CONCLUSION	63
5.	MODELLING	65
5.1.	THE COMSOL MODEL	65
5.2.	2D AND 3D MODEL GEOMETRY	66
5.3.	MODEL ASSUMPTIONS AND UNCERTAINTY	66
5.4.	SIMULATION RESULTS	67
5.4.1.	2D simulations	68
5.4.2.	3D simulations	72
5.5.	CHAPTER CONCLUSION	78
6.	CONCLUSION AND RECOMMENDATION	79
6.1.	CONCLUSIONS AND EVALUATION OF THE PROJECT	79
6.2.	RECOMMENDATIONS	80
	REFERENCES	81
	APPENDIX A: ADDITIONAL EXPERIMENT PLOTS	83
	APPENDIX B: ADDITIONAL SIMULATION PLOTS	87
B.1.	2D TANK DESIGNS AND RESULTS	87
B.2.	SENSITIVITY ANALYSIS PLOTS	92
B.3.	ADDITIONAL 3D SIMULATION PLOTS	93
	APPENDIX C: REFERENCE DRILLING LOGS	100
	APPENDIX D: DRILLING FLUID COMPONENT DATA SHEETS	104
D.1.	CEBO-GEL WYOMING API BENTONITE	104
D.2.	XANTHAN GUM	106
D.3.	M6 SILVERBOND QUARTZ FLOUR (BARITE REPLACER)	108
D.4.	SIEVED M32 FINE SAND (CUTTINGS REPLACER)	110
	APPENDIX E: MATLAB CODE	112
E.1.	MAIN CODE	112
E.2.	FUNCTIONS	114

Abbreviations

3ME	Faculty of Mechanical, Maritime and Materials Engineering
API	American Petroleum Institute
BOP	Blow Out Preventer
CFD	Computational fluid dynamics
CiTG	Faculty of Civil Engineering and Geosciences
HPHT	High Pressure High Temperature
HWT	Huisman Well Technology
LVDT	Linear variable differential transformer
MPD	Managed Pressure Drilling
OBD	Overbalanced drilling
OBM	Oil Based Mud
PAC	Poly Anionic Cellulose
PCD	Pressure Control Device
PSD	Particle Size Distributions
PV	Plastic viscosity
RANS	Reynolds-averaged Navier-Stokes
RCD	Rotating Control Device
RPM	Revolutions per minute
TU Delft	Delft University of Technology
Vol%	Volume percentage
WBM	Water Based mud
Wt%	Weight percentage
YP	Yield point

Nomenclature

Latin symbols	Description	Unit
B	Width	[m]
C_d	Drag coefficient	[-]
C_{sol}	Solids concentration	[-]
$C_{sol,max}$	Maximum solids concentration	[-]
$C_{sol,total}$	Total solids concentration	[-]
D_*	Particle parameter	[-]
d_p	Particle diameter	[m]
F_b	Buoyancy force	[kg·m/s ²]
F_d	Frictional drag force	[kg·m/s ²]
F_g	Gravitational force	[kg·m/s ²]
Fr	Froude number	[-]
F_{sup}	Support force	[kg·m/s ²]
g	Gravitational constant	[m/s ²]
H	Height	[m]
H_{cake}	Cake thickness	[m]
K	Flow consistency	[Pa·s]
k	Filter permeability	[m ²]
L	Length	[m]
n	Flow behaviour index	[-]
n_{RZ}	Richardson & Zaki index	[-]
$n_{RZ,i}$	Richardson & Zaki index of fraction i	[-]
n_{por}	Porosity	[-]
p	Pressure	[Pa]
Δp	Pressure difference	[Pa]
Q	Flow rate	[m ³ /s]
q	Specific flow rate	[m/s]
R	Hydraulic radius	[m]
r	Cylindrical coordinate	[-]
Re	Reynolds Number	[-]
Re_p	Particle Reynolds number	[-]
s	Relative density	[-]
T	Temperature	[°C]
t	Time	[s]
$v, v_0, v_r, v_z, v_\theta$	Velocity	[m/s]
v^*	Dimensionless parameter	[-]
v_s	Settling velocity	[m/s]
v_{sc}	critical scour velocity	[m/s]
v_{slip}	Slip velocity	[m/s]
$v_{slip,i}$	Slip velocity of fraction i	[m/s]
v_{tsv}	Terminal settling velocity	[m/s]
z	Cylindrical coordinate	[-]

Greek symbols	Description	Unit
α_{cr}	Dimensionless parameter	[-]
α_H	Specific filter resistance	[1/m ²]
β	Mechanical friction factor	[-]
$\dot{\gamma}$	Shear rate	[1/s]
$\dot{\gamma}_{min}$	Minimum shear rate	[1/s]
θ	Cylindrical coordinate	[-]

θ_{Fann}	Fann dial deflection	[lb/100 ft ²]
κ	Geometrical factor	[-]
λ	Hydraulic viscous friction factor	[-]
μ	Dynamic viscosity	[Pa·s]
μ_{app}	Apparent viscosity	[Pa·s]
μ_{eff}	Effective viscosity	[Pa·s]
μ_{pl}	Plastic viscosity	[Pa·s]
ν_{kin}	Kinematic viscosity	[m ² /s]
ρ_f	Fluid density	[kg/m ³]
ρ_p	Particle density	[kg/m ³]
τ	Shear stress	[Pa]
τ_0^b	Bingham yield point	[Pa]
τ_0^{hb}	Herschel-Bulkley yield point	[Pa]
τ_{eff}	Effective yield stress	[Pa]
τ_h	Hydraulic shear	[Pa]
τ_m	Mechanical shear	[Pa]
ψ	Shape factor	[-]
Ω	Angular velocity	[rad/s]
ω_{Fann}	Fann rotor speed	[r/min]

List of figures

FIGURE 1: EXAMPLE OF A DRILLING RIG SETUP WITH A MUD TREATMENT SYSTEM [28]	19
FIGURE 2: ROTARY DRILLING SYSTEM AND FLOW DIRECTIONS IN THE ANNULUS [3].	21
FIGURE 3: BLOW OUT PREVENTER (BOP), ROTATING CONTROL DEVICE (RCD) AND MPD CHOKE MANIFOLD [4].	21
FIGURE 4: TYPICAL WBM COMPOSITION BY VOLUME [7]	22
FIGURE 5: DRILLING FLUID	22
FIGURE 6: TYPICAL PSD OF API BARITE [8]	22
FIGURE 7: PSD OF A 6% WT% BENTONITE SOLUTION [9].	22
FIGURE 8: RHEOLOGY MODELS AND FLUID CONSISTENCY CURVES	23
FIGURE 9: TYPICAL SHALE SHAKER SCHEMATIC [3]	25
FIGURE 10: TYPICAL HYDROCYCLONE SCHEMATIC [10]	25
FIGURE 11: TYPICAL DECANter CENTRIFUGE SCHEMATIC [3]	25
FIGURE 12: COMPLETE MUD TREATMENT SYSTEM (COMPONENTS NEED TO BE INTERCHANGED FOR OPTIMAL SOLIDS REMOVAL)	25
FIGURE 13: FORCES ACTING ON A SUSPENDED PARTICLE	26
FIGURE 14: PARTICLE SETTLING PATTERN [31].	28
FIGURE 15: FORCES ACTING ON A SUSPENDED SPHERE PARTICLE IN A VISCOPLASTIC FLUID	30
FIGURE 16: INFLUENCE OF TEMPERATURE AND PRESSURE ON VISCOSITY AND YIELD STRESS [56]. (Δ , $T = 27^{\circ}\text{C}$. \blacktriangle , $T = 65^{\circ}\text{C}$. \circ , $T = 85^{\circ}\text{C}$.)	31
FIGURE 17: CONSISTENCY CURVE DRILLING FLUID BASED ON CLAY AND BARITE SOLUTION IN WATER [41].	32
FIGURE 18: CONSISTENCY CURVE DRILLING FLUID BASED ON CLAY SOLUTION IN WATER [41].	32
FIGURE 19: CONSISTENCY CURVE OIL BASED DRILLING FLUID [41]	32
FIGURE 20: CONSISTENCY CURVE PAC SOLUTION IN WATER [41]	32
FIGURE 21: BOTTOM SCOUR IN A SEDIMENTATION TANK	33
FIGURE 22: FILTRATION MODELS [26]	34
FIGURE 23: OVERVIEW OF AN IDEAL HORIZONTAL FLOW SETTLING TANK [45]	36
FIGURE 24: SETTLING TRAJECTORY IN HORIZONTAL FLOW SEDIMENTATION ZONE [45]	36
FIGURE 25: DIFFERENCE BETWEEN SETTLING MODELS TERMINAL SETTLING VELOCITY	38
FIGURE 26: DIFFERENCE BETWEEN PARTICLE REYNOLDS NUMBERS	38
FIGURE 27: INFLUENCE OF HINDERED SETTLING ON THE PARTICLE SLIP VELOCITY	39
FIGURE 28: INCREASE OF THE SETTLEABLE PARTICLE SIZE DUE TO INCREASING PARTICLE CONCENTRATION	39
FIGURE 29: INCREASING SETTLING EFFICIENCY WITH DECREASING FLOW RATE	40
FIGURE 30: DECREASE OF SETTLEABLE PARTICLE SIZE DUE TO FLOW RATE REDUCTION	40
FIGURE 31: INCREASING TERMINAL SETTLING VELOCITY WITH DECREASING CARRYING FLUID VISCOSITY	41
FIGURE 32: INCREASE IN SETTLEABLE PARTICLE SIZES DUE TO VISCOSITY REDUCTION	41
FIGURE 33: DRILLING MUD MATERIALS FROM LEFT TO RIGHT: QUARTS FLOUR, BENTONITE AND XANTHAN GUM	43
FIGURE 34: SAMPLE COMPOSITION BY WEIGHT	43
FIGURE 35: SAMPLE COMPOSITION BY VOLUME	43
FIGURE 36: CONSISTENCY CURVE OF CLEAN MUD SAMPLE VERSUS REFERENCE	44
FIGURE 37: FANN MODEL 35SA VISCOMETER	45
FIGURE 38: SCHEMATIC DIAGRAM OF THE DIRECT INDICATING VISCOMETER	45
FIGURE 39: VERTICAL VIBRATION TEST SETUP OVERVIEW	46
FIGURE 40: VERTICAL VIBRATION TEST SETUP	46
FIGURE 41: HORIZONTAL VIBRATION TEST SETUP	46
FIGURE 42: HORIZONTAL VIBRATION TEST SETUP TOP VIEW	46
FIGURE 43: PRESSURE FILTRATION SETUP	48
FIGURE 44: PRESSURE FILTRATION SETUP SCHEMATIC	48
FIGURE 45: MODIFIED STEEL AND NYLON WIRE MESH FILTERS	48
FIGURE 46: RESULTS OF CLEAN DRILLING FLUID – CONSISTENCY CURVES	49
FIGURE 47: CLEAN DRILLING FLUID RESULTS - APPARENT VISCOSITY	50
FIGURE 48: VISCOSITY REDUCTIONS AT 3 RPM ABOVE AND 6 RPM BELOW	52
FIGURE 49: 0.1 PA·S CALIBRATION FLUID - APPARENT VISCOSITY COMPARISON	55
FIGURE 50: 10% GLYCEROL SOLUTION - APPARENT VISCOSITY COMPARISON	55
FIGURE 51: CONSISTENCY CURVES OF GLYCEROL AT VARIOUS TEMPERATURES [15]	56
FIGURE 52: DRILLING FLUID THIXOTROPIC BEHAVIOUR – HYSTERESIS LOOP [21]	56
FIGURE 53: FLUID MOTION – SIDE VIEW OF VERTICAL AND TOP VIEW OF HORIZONTAL VIBRATION SETUPS	57
FIGURE 54: TOP VIEW OF THE ANNULAR SHEAR SPACE BETWEEN THE ROTOR AND BOB [44]	57
FIGURE 55: RIPPED WHATMAN FILTER PAPER	62
FIGURE 56: 250 MM FILTER INSIDE THE PRESSURE FILTRATION APPARATUS	62
FIGURE 57: FILTER CAKE – 20-25 MM FILTER WITH NO ADDITIONAL PARTICLES AT 0.25 BAR	62
FIGURE 58: FILTER CAKE – 63 MM FILTER WITH 17% 150-212 MM PARTICLES AT 1 BAR	62
FIGURE 59: FILTER CAKE – 250 MM FILTER WITH 9% 150-212 MM PARTICLES AT 6 BAR	62
FIGURE 60: FILTER CAKE - 250 FILTER WITH NO ADDITIONAL PARTICLES AT 1 BAR	62

FIGURE 61: FILTER CAKE - 250 FILTER WITH NO ADDITIONAL PARTICLES AT 1 BAR CLOSE UP	62
FIGURE 62: FILTER CAKE PRESSURE VERSUS PERMEABILITY BASED ON ENGELHARDT (1954) [27]	63
FIGURE 63: 2D AND 3D MESHES.....	67
FIGURE 64: 2D SIMULATION - FLOW VELOCITY [m/s] AND FLOW FIELD.....	68
FIGURE 65: 2D SIMULATION - SHEAR RATE [1/s] AND FLOW FIELD	68
FIGURE 66: 2D SIMULATION - APPARENT VISCOSITY [Pa·s] AND STREAM LINES	68
FIGURE 67: 2D SIMULATION - PARTICLE CONCENTRATION [%] AND STREAM LINES	69
FIGURE 68: 2D SIMULATION - AVERAGE PARTICLE DISCHARGE CONCENTRATION AT THE OUTLET [%]	69
FIGURE 69: 2D SIMULATION OF THE FINAL BAFFLED TWO-FLOOR TANK - FLOW VELOCITY [m/s] AND FLOW FIELD	70
FIGURE 70: 2D SIMULATION OF THE FINAL BAFFLED TWO-FLOOR TANK - SHEAR RATE [1/s] AND FLOW FIELD	71
FIGURE 71: 2D SIMULATION OF THE FINAL BAFFLED TWO-FLOOR TANK - APPARENT VISCOSITY [Pa·s] AND STREAM LINES	71
FIGURE 72: 2D SIMULATION OF THE FINAL BAFFLED TWO-FLOOR TANK - PARTICLE CONCENTRATION [%] AND STREAM LINES	71
FIGURE 73: 2D SIMULATION OF THE FINAL BAFFLED TWO-FLOOR TANK - AVERAGE PARTICLE DISCHARGE CONCENTRATION AT THE OUTLET [%].....	71
FIGURE 74: 3D SIMULATIONS - 3D TANK DESIGN OVERVIEW	72
FIGURE 75: 3D SIMULATIONS - 3D TANK DESIGN CROSS SECTION WITH DIMENSIONS [MM].....	73
FIGURE 76: 3D SIMULATIONS - SINGLE INLET FLOW VELOCITY [m/s] SIDE AND MULTI-PLANE VIEW	73
FIGURE 77: 3D SIMULATIONS - DOUBLE INLET FLOW VELOCITY [m/s] SIDE AND MULTI-PLANE VIEW	73
FIGURE 78: 3D SIMULATION POWER-LAW - PARTICLE CONCENTRATIONS [%] FOR AN INFLOW OF 3000 AND 1000 L/MIN AND PARTICLES OF 5 MM	74
FIGURE 79: 3D SIMULATION POWER-LAW - PARTICLE CONCENTRATIONS [%] FOR AN INFLOW OF 3000 AND 1000 L/MIN AND PARTICLES OF 3 MM	74
FIGURE 80: 3D SIMULATION POWER-LAW - PARTICLE CONCENTRATIONS [%] FOR AN INFLOW OF 3000 AND 1000 L/MIN AND PARTICLES OF 1 MM	74
FIGURE 81: 3D SIMULATION POWER-LAW - AVERAGE PARTICLE DISCHARGE CONCENTRATIONS AT THE OUTLET [%].....	75
FIGURE 82: 3D SIMULATION POWER-LAW - REMOVAL RATIO [-]	75
FIGURE 83: 3D SIMULATION FIXED VISCOSITY - PARTICLE CONCENTRATIONS [%] FOR AN INFLOW OF 3000 AND 1000 L/MIN AND PARTICLES OF 5 MM	76
FIGURE 84: 3D SIMULATION FIXED VISCOSITY - PARTICLE CONCENTRATIONS [%] FOR AN INFLOW OF 3000 AND 1000 L/MIN AND PARTICLES OF 3 MM	76
FIGURE 85: 3D SIMULATION FIXED VISCOSITY - PARTICLE CONCENTRATIONS [%] FOR AN INFLOW OF 3000 AND 1000 L/MIN AND PARTICLES OF 1 MM	77
FIGURE 86: 3D SIMULATION FIXED VISCOSITY - AVERAGE PARTICLE DISCHARGE CONCENTRATIONS AT THE OUTLET [%]	77
FIGURE 87: 3D SIMULATION FIXED VISCOSITY - REMOVAL RATIO [-]	77
FIGURE 88: DRILLING FLUID WITH 9% 250-300 MICRON CUTTINGS - CONSISTENCY CURVE	83
FIGURE 89: DRILLING FLUID WITH 9% 250-300 MICRON CUTTINGS - APPARENT VISCOSITY	83
FIGURE 90: DRILLING FLUID WITH 17% 250-300 MICRON CUTTINGS - CONSISTENCY CURVE	84
FIGURE 91: DRILLING FLUID WITH 17% 250-300 MICRON CUTTINGS - APPARENT VISCOSITY	84
FIGURE 92: DRILLING FLUID WITH 9% 150-212 MICRON CUTTINGS - CONSISTENCY CURVE	85
FIGURE 93: DRILLING FLUID WITH 9% 150-212 MICRON CUTTINGS - APPARENT VISCOSITY	85
FIGURE 94: DRILLING FLUID WITH 17% 150-212 MICRON CUTTINGS - CONSISTENCY CURVE	86
FIGURE 95: DRILLING FLUID WITH 17% 150-212 MICRON CUTTINGS - APPARENT VISCOSITY	86
FIGURE 96: 2D SIMULATION DESIGN 1 - PARTICLE CONCENTRATION [%] AND STREAM LINES	87
FIGURE 97: 2D SIMULATION DESIGN 1 - AVERAGE PARTICLE DISCHARGE CONCENTRATION AT THE OUTLET [%]	87
FIGURE 98: 2D SIMULATION DESIGN 2 - PARTICLE CONCENTRATION [%] AND STREAM LINES	87
FIGURE 99: 2D SIMULATION DESIGN 2 - AVERAGE PARTICLE DISCHARGE CONCENTRATION AT THE OUTLET [%]	88
FIGURE 100: 2D SIMULATION DESIGN 3 - PARTICLE CONCENTRATION [%] AND STREAM LINES	88
FIGURE 101: 2D SIMULATION DESIGN 3 - AVERAGE PARTICLE DISCHARGE CONCENTRATION AT THE OUTLET [%]	88
FIGURE 102: 2D SIMULATION DESIGN 4 - PARTICLE CONCENTRATION [%] AND STREAM LINES	89
FIGURE 103: 2D SIMULATION DESIGN 4 - AVERAGE PARTICLE DISCHARGE CONCENTRATION AT THE OUTLET [%]	89
FIGURE 104: 2D SIMULATION DESIGN 5 - PARTICLE CONCENTRATION [%] AND STREAM LINES	89
FIGURE 105: 2D SIMULATION DESIGN 5 - AVERAGE PARTICLE DISCHARGE CONCENTRATION AT THE OUTLET [%]	90
FIGURE 106: 2D SIMULATION DESIGN 6 - PARTICLE CONCENTRATION [%] AND STREAM LINES	90
FIGURE 107: 2D SIMULATION DESIGN 6 - AVERAGE PARTICLE DISCHARGE CONCENTRATION AT THE OUTLET [%]	90
FIGURE 108: 2D SIMULATION DESIGN 7 - PARTICLE CONCENTRATION [%] AND STREAM LINES	91
FIGURE 109: 2D SIMULATION DESIGN 7 - AVERAGE PARTICLE DISCHARGE CONCENTRATION AT THE OUTLET [%]	91
FIGURE 110: 2D SIMULATION BAFFLE SENSITIVITY - GEOMETRY OVERVIEW	92
FIGURE 111: 2D SIMULATION BAFFLE SENSITIVITY - AVERAGE PARTICLE DISCHARGE CONCENTRATION AT THE OUTLET [%]	92
FIGURE 112: 3D SIMULATION POWER-LAW - PARTICLE CONCENTRATIONS [%] FOR PARTICLES OF 5 MM	94
FIGURE 113: 3D SIMULATION POWER-LAW - PARTICLE CONCENTRATIONS [%] FOR PARTICLES OF 3 MM	95
FIGURE 114: 3D SIMULATION POWER-LAW - PARTICLE CONCENTRATIONS [%] FOR PARTICLES OF 1 MM	96
FIGURE 115: 3D SIMULATION POWER-LAW - PARTICLE CONCENTRATIONS [%] FOR PARTICLES OF 5 MM	97
FIGURE 116: 3D SIMULATION POWER-LAW - PARTICLE CONCENTRATIONS [%] FOR PARTICLES OF 3 MM	98
FIGURE 117: 3D SIMULATION POWER-LAW - PARTICLE CONCENTRATIONS [%] FOR PARTICLES OF 1 MM	99

List of tables

TABLE 1: MUD TREATMENT COMPONENTS AND PARTICLE REMOVAL SIZES [3][5]	24
TABLE 2: CLASSIFICATION OF PARTICLES IN DRILLING FLUIDS [3]	24
TABLE 3: LIST OF RELATIONS FOR THE PREDICTION OF THE TERMINAL SETTLING VELOCITY [37]	27
TABLE 4: EMPIRICAL RELATION FOR THE PREDICTION OF THE TERMINAL SETTLING VELOCITY [37][38]	27
TABLE 5: SCHILLER-NAUMANN DRAG MODEL [50]	27
TABLE 6: EMPIRICAL RELATIONS TO SELECT FOR SELECTING SAND SCREENS	35
TABLE 7: INPUT PARAMETERS FOR MATLAB	37
TABLE 8: FLUID CHARACTERISTICS OF THE CLEAN MUD SAMPLE VERSUS REFERENCE DATA	44
TABLE 9: FANN CALIBRATION RESULTS	49
TABLE 10: CLEAN DRILLING FLUID RESULTS - APPARENT VISCOSITY REDUCTION	50
TABLE 11: UNCERTAINTY OF THE FANN VISCOSITY MEASUREMENTS	51
TABLE 12: APPARENT VISCOSITY INCREASE AS A RESULT OF ADDITIONAL PARTICLES IN CLEAN DRILLING FLUID	51
TABLE 13: APPARENT VISCOSITY REDUCTIONS FOR DRILLING FLUID WITH 150-212 MICRON SUSPENDED PARTICLE	51
TABLE 14: APPARENT VISCOSITY REDUCTIONS FOR A DRILLING FLUID WITH 250-300 MICRON SUSPENDED PARTICLE	52
TABLE 15: APPARENT VISCOSITY REDUCTION OF A CLEAN DRILLING FLUID FOR DIFFERENT FREQUENCIES AND AMPLITUDES	53
TABLE 16: APPARENT VISCOSITY REDUCTION OF A CLEAN DRILLING FLUID FOR INCREASING FREQUENCY AND FIXED AMPLITUDE OF 0.15 MM	53
TABLE 17: FANN DEFLECTION READINGS FOR 3 RPM AND 10 SEC GEL STRENGTH	54
TABLE 18: THE RELATIVE VISCOSITY DIFFERENCES BETWEEN THE CONTROL MEASUREMENTS PERFORMED FOR EACH SET OF EXPERIMENTS	54
TABLE 19: THE SPECIFIC GRAVITY MEASUREMENTS PERFORMED FOR EACH SET OF EXPERIMENTS	54
TABLE 20: FILTRATION RESULTS - X = CLOGGED FILTER, R = RIPPED FILTER, O = FLOW THROUGH FILTER, '-' = NOT PERFORMED COMBINATION	61
TABLE 21: FILTER OPENINGS REQUIRED TO RETAIN SAND PARTICLES BASED ON COBERLY AND SAUCIER	61
TABLE 22: COMSOL INPUT PARAMETERS	65
TABLE 23: 2D AND 3D SETTLING TANK DIMENSION	66
TABLE 24: DIMENSIONS OF INTERNAL ELEMENTS 3D MODEL	72

1. Introduction

In this introductory chapter, information is provided about the project background and the problem definition. The project objective and the related secondary objectives are composed in the second part based on the problem definition. The last section includes a reading guide, briefly summarizing the thesis outline.

1.1. Background

The drilling companies in today's oil and gas drilling industry are challenged to reduce their production costs to breakeven in the low-price oil market. As seen in other industries, automatization of the expensive labour intensive processes is a promising approach to achieve this goal.

This thesis focuses on the drilling fluid treatment process, which plays a critical role in drilling process. The drilling fluid treatment process is a labour intensive activity, involving the management of multiple separation equipment. This results in a significant cost contribution to the total well costs of up to 10% [36]. Future development and automatization of the drilling fluid treatment process promises thus an interesting opportunity to save on total well costs. To achieve this development, future understanding of the drilling fluid functions, behaviour, composition and the various mud treatment processes is required.

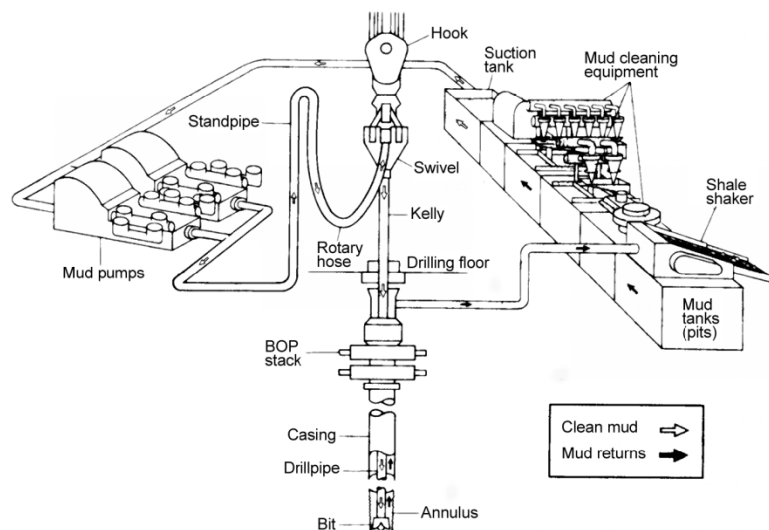


Figure 1: Example of a drilling rig setup with a mud treatment system [28]

Drilling fluids are used all over the world to aid drilling operations into the earth. They come in various types and are used in all kinds of drilling operations ranging from tunnelling with tunnel boring machines to the drilling of oil and gas wells from large offshore drilling platforms. The drilling fluid fulfils important tasks like cooling the drill bits, providing support pressure in the borehole and transporting the drilled solids from downhole to the surface, where it is guided to the mud treatment system by the flowline.

The removal of the large cuttings takes place at the beginning of the mud treatment cycle where the two phase flow is distributed over multiple filtration screens, or so called shale shakers. The liquid is allowed to drain through the filter medium while the cuttings retain on the filter screens. In order to remove silt and finer particles, the drilling fluid is further treated by hydrocyclone units; desander, desilters and centrifuges.

In order to enhance the separation performance of cuttings from the drilling fluid, a thorough understanding of the non-Newtonian drilling fluid and particle interaction is required. Only then future development, with respect to space requirements, efficiency, automation and control is possible.

1.2. Problem description

In the present drilling industry, drilling mud treatment systems consist of many separate components, which make them complicated, labour intensive, largely energy consuming and costly to automate. Research is being carried out by Huisman Well Technology (HWT) to come up with effective measures to improve the cutting separation process and reduce unwanted effects of the traditional system such as cuttings degradation and loss of additives.

The targeted concept is an enclosed pressurized separation tank that uses gravitational settlement as a separation technique to remove larger cuttings from the drilling fluid. The smaller particles that will not settle will be removed from the drilling fluid by regulated and precise filtration. With the development of the enclosed separation tank, it is aimed to simplify the overall system by eliminating components of the traditional treatment system and thereby making automation viable.

1.3. Project objective

The main objective of this thesis is to perform a feasibility study for the pressurized separation tank and the proposed separation techniques. In order to achieve this goal a literature review and experiments have been performed. The results of these studies are combined into a model to simulate the settling efficiency within the proposed separation tank.

In order to structure the research strategy, a clear main objective and five secondary objectives have been defined. The main research goal for the thesis is:

Perform a feasibility study for a pressurized solids separation tank, which uses gravitational settling and precise filtration as separation techniques to separate suspended solids down to 20 microns.

The secondary objectives are as follows:

1. *Perform a literature review on relevant processes that play a role in particle settling and filtration.*
2. *Create a model and include relevant effects to study the parameter influence on particle settling.*
3. *Perform experiments to get an indication of the applicability and to gain realistic input parameters:*
 - a. *Influence of vibrations on the drilling fluid viscosity*
 - b. *Pressure filtration performance*
4. *Perform simulations to evaluate the separation efficiency of the separation tank.*
5. *Evaluate the feasibility and effectiveness of the separation tank.*

1.4. Thesis outline

This reading guide gives an overview of the main part of the thesis report starting from Chapter 2.

- Chapter 2 presents the theoretical background that is relevant for the project. It provides background information and discusses various processes and parameter effects relevant for the gravitational settling of particles in tanks and particle separation by filtration.
- The considered effects influencing the gravitational settling of particles are evaluated in Chapter 3, by assessing them using Camp's ideal settling tank model.
- Chapter 4 focusses on the vibration and filtration experiments. In order to improve the settling rate of particles, the influences of vibrations on the drilling fluid viscosity are verified. Secondly, the achievability to separate fine particles from the drilling fluid is tested using pressure filtration.
- The information obtained from previous chapters is combined into a COMSOL model, which is discussed in Chapter 5. In order to obtain an efficient separation tank, 2D and 3D simulations are evaluated.
- Chapter 6 concludes the thesis by briefly summarizing the main conclusions of the performed work and evaluates the feasibility of the solids separation tank. The recommendations for future research and development are also included in this chapter.

2. Theoretical background

This section of the report will include the theoretical background of drilling fluids and mud treatment systems. It will cover the most important results from the literature study.

2.1. The drilling process

One of the most commonly used and effective methods for drilling into the earth's formations is the rotary drilling method. This method is based on a rotating drill bit which is driven by rotating the entire drill pipe at the surface. By applying a downward force on the rotating bit, the system is able to penetrate even the hardest rock. During operation the bit crushes or shears the rock and cuttings are generated at the contact point between the drilling bit and the formation. These cuttings are subsequently transported to the surface by circulating drilling fluid down the drill pipe, through the drilling bit and up the annular space between the drill pipe and borehole wall. At the surface the suspended cuttings are removed from the drilling fluid and circulation continues by pumping the fresh drilling fluid back downhole.

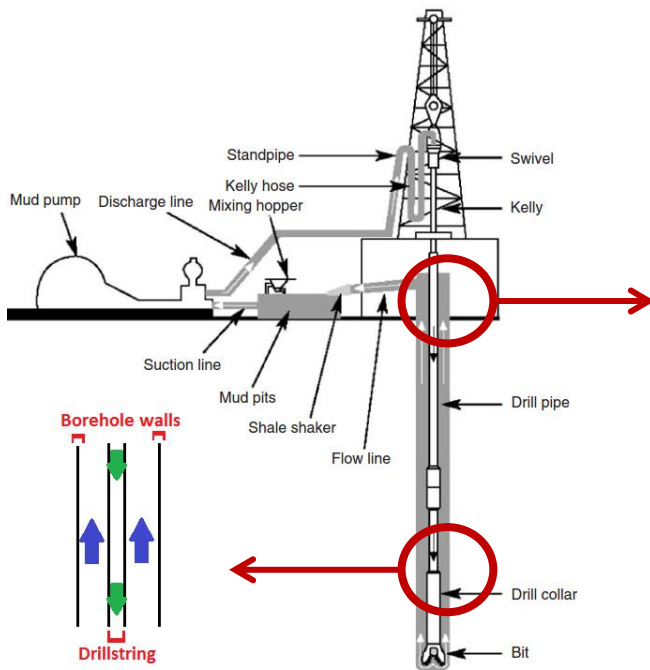


Figure 2: Rotary drilling system and flow directions in the annulus [7].

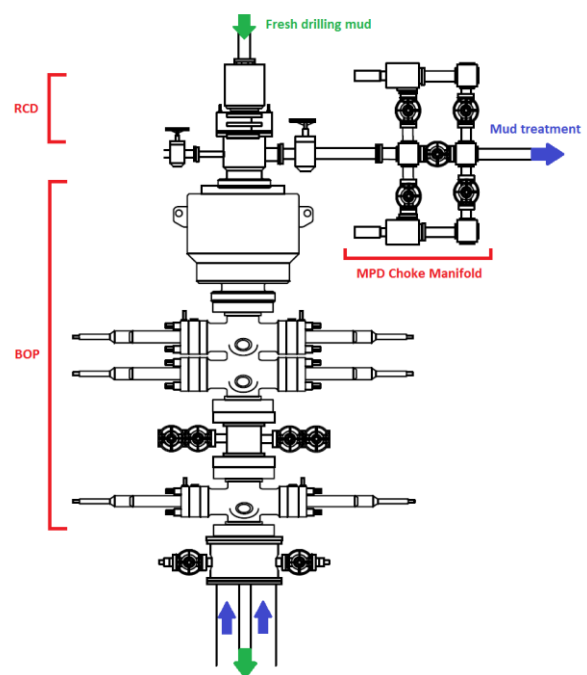


Figure 3: Blow Out Preventer (BOP), Rotating Control Device (RCD) and MPD Choke Manifold [38].

During the drilling process operating pressures are limited to a drilling margin, which is defined as the difference between the maximum pore pressure and the minimum effective fracture pressure of the formation. Staying within this margin prevents influx of formation fluids to the well and unwanted rock fracturing. In overbalanced drilling (OBD), the drilling fluid weight is continuously managed (by weighting agents) to maintain a borehole pressure which exceeds the maximum pore pressure in the formation. However, when the drilling margin becomes narrower, the OBD method becomes more challenging. In this case Managed Pressure Drilling is a more favourable option.

Managed Pressure Drilling (MPD) is defined as: an adaptive drilling process used to precisely control the annular pressure profile throughout the wellbore. The objectives are to ascertain the downhole pressure limits and to manage the annular hydraulic pressure profile accordingly. The pressure in the annulus is controlled by sealing it off near the surface with a Rotating Control Device (RCD) or Pressure Control Device (PCD) as shown in Figure 3. By adjusting the MPD choke the outflow of mud is restricted and pressure is able to build up in the wellbore. While MPD is much safer and more advantageous compared to OBD in most cases, it comes with different drawbacks. One of the drawbacks arises at the MPD choke manifold, as the mud containing suspended solids flows through multiple narrow valves and nozzles in the MPD Choke Manifold. Due to high velocities and narrow gaps, the solids in the drilling fluid are crushed into smaller particles. Since finer particles tend to stay in suspension longer and are harder to separate, crushing the large solids reduces the efficiency of the mud treatment system.

2.2. The drilling fluids

In geotechnical engineering and similar branches, drilling fluids are used to aid the drilling process. The drilling fluid has many important functions including: transport of cuttings to the surface, cooling of the drill bit and multiple borehole stabilization functions. The traditional drilling fluids can be categorized into two main categories: Water Based muds (WBM) and Oil Based Mud (OBM). In this thesis the focus will be on water based drilling fluids composed mainly of water, bentonite and barite, as this is the commonly used drilling fluid type in the drilling industry.

The WBM compositions are flexible and can differ significantly based on the drilled formation. Properties such as weight, viscosity, gel strength, filtration characteristics and many more are manageable by regulating the fluid composition. The overall composition however, can be divided into four main components: fluid base (fresh or sea-water), viscosifiers (e.g. bentonite), weighting agents (e.g. barite) and additives. In Figure 4 an example is shown of a typical WBM composition by volume.

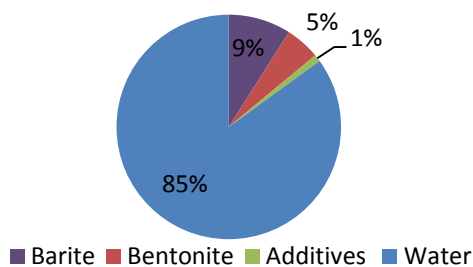


Figure 4: Typical WBM composition by volume [27]



Figure 5: Drilling fluid

2.2.1. Particle size distribution of solids in drilling fluid

Since mud treatment equipment relies greatly on particle size based separation techniques, it is essential to classify the Particle Size Distributions (PSD) of solids in the drilling fluid. Similar to many other drilling fluid components and additives, specifications of drilling grade barite and bentonite are prescribed by the American Petroleum Institute (API) in API 13/ISO 13500.

Due to its high specific gravity, barite is the commonly used weighting agent in the drilling industry. Drilling grade barite is prepared by dry milling to meet the standards, which require that at least 97% wt% of the material, can pass through a 200-mesh (74- μm) screen, while no more than 30% wt%, can be smaller than 6 μm diameter, and the specific gravity needs to be 4.1 or greater [5]. Figure 6 shows the PSD of API barite.

Bentonite is a naturally occurring clay consisting mostly of smectite and other accessory minerals, such as quartz, mica, feldspar and calcite. The smectite minerals in bentonite are by definition clays, meaning they have a mean particle diameter of <2 μm . However when mixed with water the smectite forms structures (flocs) that can have larger particle sizes. Figure 7 shows the PSD of a 6% wt%, bentonite suspension obtained from wet sieving. Natural drilling grade bentonite requires that at least 96% wt%, can pass through a 200-mesh (74- μm) screen during a wet sieving test [5].

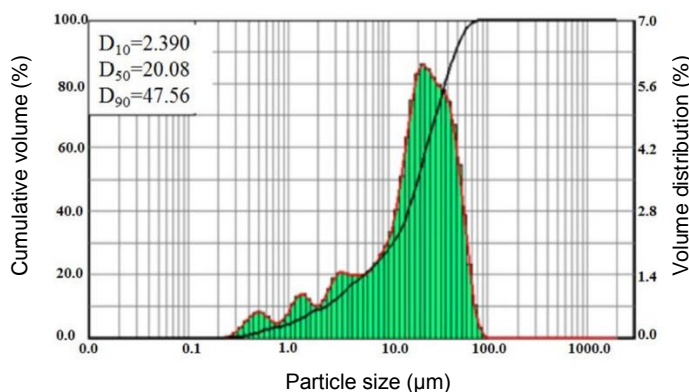


Figure 6: Typical PSD of API barite [15]

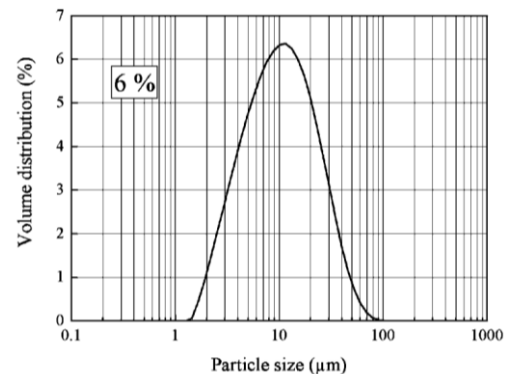


Figure 7: PSD of a 6% wt% bentonite solution [9]

2.2.2. Rheology of the drilling fluid

The drilling fluid rheology forms an important parameter in drilling operations, since it describes the flow and deformation characteristics of the drilling fluid. Most drilling fluids used in today's industry are categorised by a viscoplastic non-Newtonian rheology and are described by a combination of the Bingham and Power law rheology models also known as the Herschel-Bulkley model. The consistency curves (or flow models) of these models are shown in Figure 8 and are described by the following equations [19]:

$$\text{Power law:} \quad \tau = K \cdot \dot{\gamma}^n \quad (1)$$

$$\text{Bingham:} \quad \tau = \tau_0^b + \mu_{pl}^B \cdot \dot{\gamma} \quad (2)$$

$$\text{Herschel-Bulkley:} \quad \tau = \tau_0^{hb} + K \cdot \dot{\gamma}^n \quad (3)$$

Where τ = shear stress [Pa], $\dot{\gamma}$ = shear rate [s^{-1}], K = flow consistency [$\text{Pa}\cdot\text{s}$], n = flow behaviour index [-], τ_0^b = Bingham yield point [Pa], μ_{pl}^B = Bingham plastic viscosity [$\text{Pa}\cdot\text{s}$] and τ_0^{hb} = Herschel-Bulkley yield point [Pa]

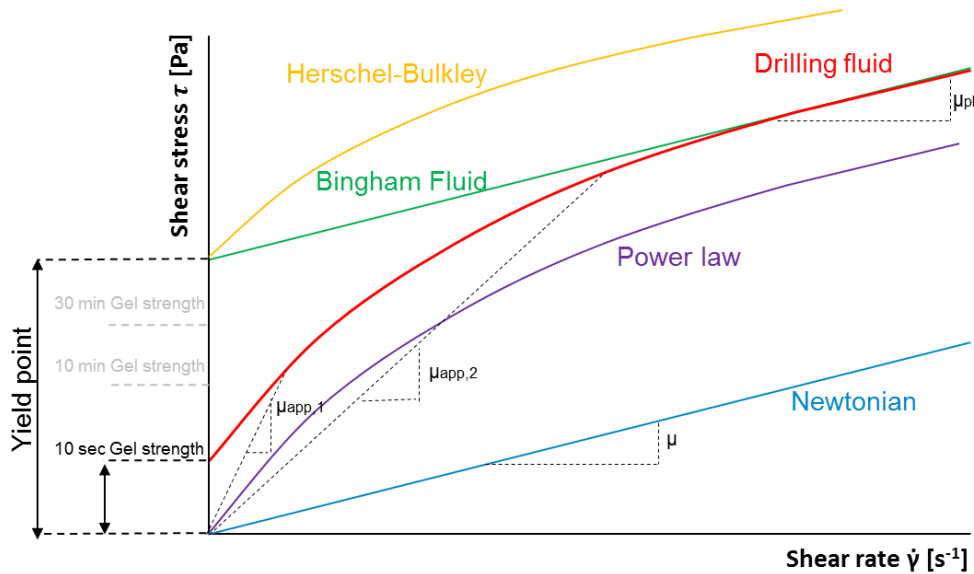


Figure 8: Rheology models and fluid consistency curves

Retention of cuttings in the drilling fluid is considered to be a function of the yield point, gel strength and viscosity. These fluid characteristics can be determined based on the consistency curves. The yield point ($\bar{Y}\bar{P}$) of the drilling fluid is the resistance of initial flow and is formed by attractive forces among colloidal particles in the drilling fluid. The gel strength is the shear stress measured at low shear rates after the drilling fluid has been static for a certain period of time. It indicates the ability of the drilling fluid to carry cuttings in a static condition. The viscosity forms a measure for the resistance to deformation by shear stresses. The dynamic or shear viscosity (μ) [$\text{Pa}\cdot\text{s}$] is defined by the ratio of shear stress (τ) [Pa] to shear rate ($\dot{\gamma}$) [s^{-1}]:

$$\mu = \frac{\tau}{\dot{\gamma}} \quad (4)$$

The Newtonian fluids like water have a linear relationship between the shear stress and shear rate, which results in a single constant viscosity and is often called the Newtonian viscosity (μ). The viscosity of non-Newtonian fluids, on the other hand, are shear rate dependent. The viscosity of these fluids is therefore specific for different shear rates and is defined as the apparent viscosity (μ_{app}). At high shear rates the fluid reaches plastic (remoulded) behaviour, this is represented by the plastic viscosity (μ_{pl}) or by the Bingham plastic viscosity. Figure 8 gives an example of the different viscosities that can be determined based on the consistency curve of a fluid.

The non-Newtonian behaviour of drilling fluids is related to the structural changes in the micro- and nanostructure of the material. The breakdown and rearrangement of the internal structure by physical or chemical processes leads to viscosity changes. When a drilling fluid experiences high shear rates the viscosity reduces, which is known as the shear-thinning behaviour of a non-Newtonian fluid. All commonly used drilling fluids are considered to be shear-thinning. When the drilling fluid is at rest and shear rates are minimal the internal structure rebuilds and gel strength starts to develop. This time dependent behaviour is known as thixotropic behaviour of a non-Newtonian fluid.

2.3. The mud treatment system

During the drilling of a well, drilling fluid is supplied through the drill pipe to the bottom of the well. The fluid together with the cuttings then flows upwards to the surface. At the surface the fluid is pumped through a series of filter screens, hydrocyclones and centrifuges which represent the mud treatment system. During this process, cuttings are removed from the fluid and new additives are supplied. The treated fluid is collected in the mud tanks, where powerful centrifugal pumps are used to pump the fluid up through the standpipe and back into the drill pipe for another drilling fluid cycle.

The mud treatment separates solids, while retaining the additives in the drilling fluid. Traditional mud treatments are open to the atmosphere and consist of multiple components, with each component having a specific particle size removal range, see Table 1.

Table 1: Mud treatment components and particle removal sizes [7][11].

	Size of particles removed [μm]	Cut point is based on:
Shale shakers	> 400 – 74	Filter screen mesh
De-sander (6 in.)	> 40	Centrifugal force, cone diameter and inflow pressure
De-silter (4 in.)	> 20	Centrifugal force, cone diameter and inflow pressure
Mud cleaner	> 74	Filter screen mesh
Centrifuge	> 2	Centrifugal force, RPM and inflow pressure

To obtain optimal fluid processing, it is favourable to have larger cuttings than the drilling fluid PSD. This makes separation of the cuttings possible without removing any of the drilling fluid components. However, during drilling operations fine cuttings are always created. Separating these cuttings is difficult since they overlap with the barite particles in weighted WBMs, see Table 2. In these cases, multiple combinations of mud treatment equipment have to be used to achieve the optimal solids removal, without removing the essential drilling fluid components.

Table 2: Classification of particles in drilling fluids [7]

Category	Size (μm)	Types of Particles
Colloidal	< 2	Bentonite, clays, ultra-fine drilled solids
Silt	2–74	Barite, silt, fine drilled solids
Sand	74–2,000	Sand, drilled solids
Gravel	> 2000	Drilled solids, gravel, cobble

The first and most important apparatus in the mud treatment system is composed of multiple parallel arranged shale shakers (vibrating filter screens). The shale shakers have a wide range of applicability due to the exchangeable screens, which makes them suitable for almost all types of drilling fluids. The drilling fluid containing a high concentration of solids flows from the flowline on top of the filter screens, where a linear vibration motion conveys the cuttings towards the discharge end. The acceleration applied on the screens can vary from 2g up to 7-8g's on the newer models. Higher g values lead to greater solids processing, but increases the wear on the screens. The drilling fluid passing through the shale shaker screens is then collected in the mud tanks for further processing. The first mud tank is usually a settling compartment (often called a sand trap). Large particles that might clog the equipment downstream, are settled in this tank. With the current fine screen capabilities of shale shakers, the sand trap mainly serves as a back-up, should the shakers be operated with damaged screens or get bypassed.

The de-sanders and de-silters are hydrocyclone separators usually operating parallel to the mud tanks. They can be distinguished from each other by the different cone sizes associated with different particle cut-off points. The hydrocyclones are accelerated settling based separators as particles settle in an increased gravitational field. The gravitational field, which can reach 200g's, is formed by centrifugal forces through pumping fluid at a high velocity from the mud tanks into the hydrocyclones. The large particles are forced against the wall and downwards to the solids discharge, while the fluid with fine particles can leave the hydrocyclone through the fluid discharge. To operate properly, pre-treatment is required to remove large particles before the drilling fluid is fed into the hydrocyclones, since large cuttings can block the exits. In practice pre-treatment by shale shakers is sufficient, however blocking of the hydrocyclones can still occur if the shale shaker screens are damaged or bypassed. The applicability of hydrocyclones in practice is limited to unweighted muds since the particle cut-off overlaps with the barite PSD or additives in weighted muds. Using hydrocyclones in the treatment processes of weighted muds would therefore result in removal of large barite quantities, which is unwanted as barite is one of the most expensive components in the drilling fluid.

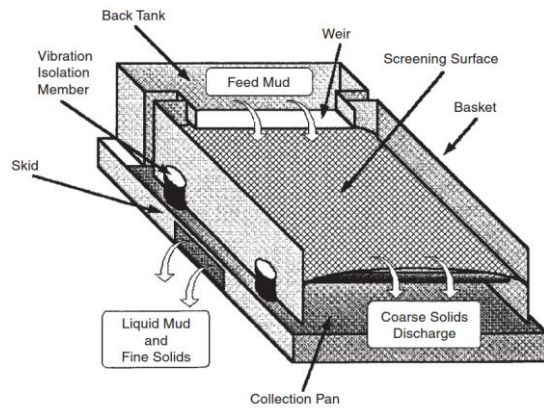


Figure 9: Typical shale shaker schematic [7]

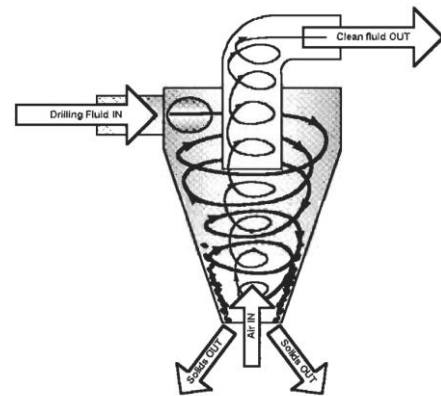


Figure 10: Typical hydrocyclone schematic [3]

The mud cleaners are separation equipment operating parallel to the mud tanks and are made up from hydrocyclones positioned above the shale shakers. This combination enables the use of hydrocyclones with weighted mud, since large barite particles separated out by the hydrocyclones can be recovered by sieving with fine screens. However, the recovered material is not pure barite, as cuttings within the barite PSD range are also recovered. This results in a lower bulk specific gravity and thus a lower quality of weighting agent.

The decanter centrifuge is generally the last apparatus in the mud treatment system and is suitable for both weighted and unweighted drilling fluid. The centrifuge aims to separate the colloidal particles from the fluid, which is accomplished by discharging the fluid rather than the solids. Separation is based on accelerated sedimentation as centrifugal forces drive the heavy particles against the centrifuge wall where they get scraped towards the solids discharge. The fluid containing the colloidal solids is discharged where larger solids are mixed back into the drilling fluid inside the mud tanks.

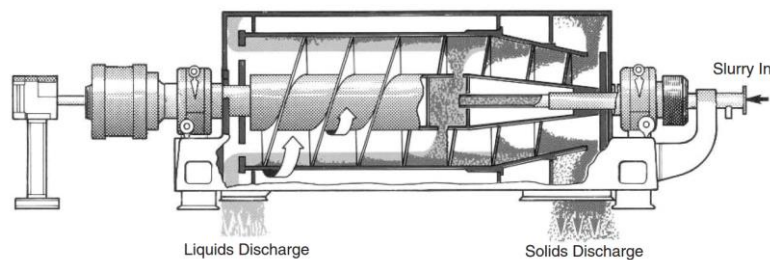


Figure 11: Typical decanter centrifuge schematic [7]

The mud treatment system separates a large portion of the unwanted particles from the drilling fluid, however during this process essential additives are also partially removed. To sustain the required drilling fluid characteristics, the removed additives are resupplied to the recycled fluid in the mixing tank. After mixing the drilling fluid is ready to be pumped back into the borehole by the mud pumps for the next cycle. Figure 12 shows the complete mud treatment system including all traditional mud treatment equipment.

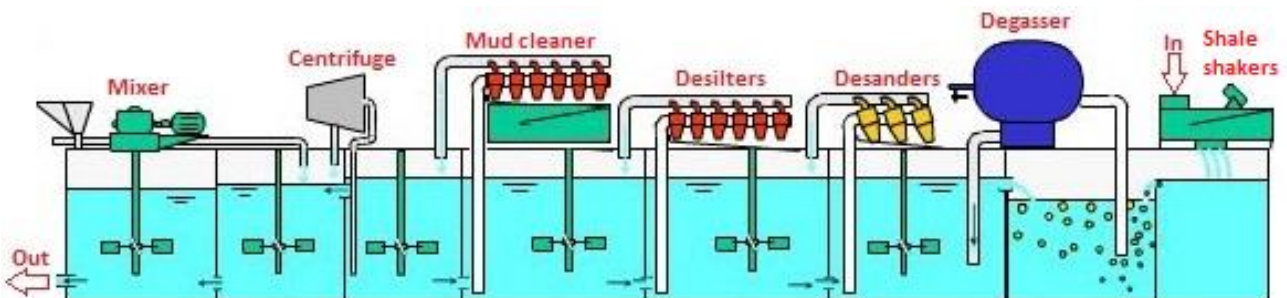


Figure 12: Complete mud treatment system (components need to be interchanged for optimal solids removal)

2.4. Settling of particles

Until now numerous studies have been performed in order to understand and describe particle settlement in Newtonian and non-Newtonian fluids. While most of these experiments are primarily focusing on defining new or validating old terminal settling velocity formulations, several of them also focus on understanding the related effects which influence the settling process. This section includes an overview of the commonly used settling formulas and the fundamental settling effects.

2.4.1. Single particle settling velocity

The settling of particles depends on the forces that are acting on the grains, which are primarily related to the grain size, grain shape, grain specific density, fluid density and fluid viscosity. The operative forces during settling have their source either in particle-liquid interaction or in particle-particle interactions. When the solids concentration is low, the particle-liquid forces dominate, whereas at high solids concentrations the particle-particle forces play a significant role. It is assumed in this study that no granular structures form since the solutions of solids in the drilling fluid stays dilute. The active forces are considered to be related mainly to the particle-liquid interactions.

The settling process of a sphere particle suspended in a liquid can be described by the forces acting on the particle, being gravity (F_g), buoyancy (F_b) and the frictional drag force (F_d), as shown in Figure 13. As the particle accelerates, the drag force increases till equilibrium is reached where the particle settles at a constant vertical velocity called the terminal settling velocity. The time required to reach the terminal settling velocity is assumed to be short as inertial effects are assumed to be negligible. This is valid for a laminar settling regime indicated by a low particle Reynolds number (Re_p).

Equilibrium is reached when:

$$F_g - F_b = F_d \quad (5)$$

The net gravitational force acting on the sphere particle can be written as [13]:

$$F_g - F_b = \pi(\rho_p - \rho_f)g \frac{d_p^3}{6} \quad (6)$$

Where: ρ_p = particle density [kg/m³], ρ_f = fluid density [kg/m³] and d_p = particle diameter [m]

The drag force on a sphere particle is defined as [13]:

$$F_d = \frac{1}{8} C_d \pi d_p^2 \rho_f v_{tsv}^2 \quad (7)$$

Where: C_d = drag coefficient [-] and v_{tsv} = terminal settling velocity [m/s]

Combining the equations above, the drag coefficient can be rewritten as [13]:

$$C_d = \frac{4(\rho_p - \rho_f)}{3\rho_f} g \frac{d_p}{v_{tsv}^2} \text{ or } v_{tsv} = \sqrt{\frac{4g(\rho_p - \rho_f)d_p}{3C_d\rho_f}} \quad (8)$$

For creeping flows (also called Stokes flow) associated with a small Reynolds number ($Re \ll 1$) and small spherical particles ($d_p \ll 1$ mm), inertial effects are negligible. Stoke (1851) derived the drag equation for these flows, presented by equation (9). Combining Stokes expression for drag force with the equations (5) and (6)(8), the famous Stokes' settling velocity for sphere particles in creeping flow can be derived as follows:

Stokes expression for the drag force of a sphere particle in creeping flow [13]:

$$F_d = 3\pi\mu_{app}d_p v_{tsv} \text{ or } C_d = \frac{24}{Re_p} \quad (9)$$

Where: μ_{app} = Apparent fluid viscosity [Pa·s]

The particle Reynolds number is defined as [13]:

$$Re_p = \frac{\rho_f v_{tsv} d_p}{\mu_{app}} \quad (10)$$

Combining the equations results in the Stoke' settling velocity for $Re_p \ll 1$ [13]:

$$v_{tsv} = \frac{g(\rho_p - \rho_f)d_p^2}{18\mu_{app}} \quad (11)$$

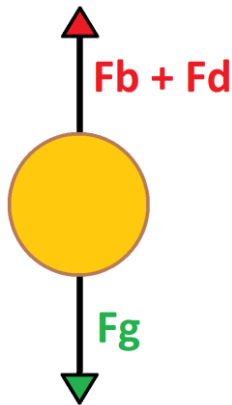


Figure 13: Forces acting on a suspended particle

When the inertial effects cannot be neglected, the drag force (or drag coefficient) cannot be predicted theoretically. Researches like Ruby (1933), Zanke (1977), Cheng (1997), Van Rijn (1989) and many others tried to experimentally determine the drag coefficient and thereby the terminal settling velocity of various particles in fluids. Different experiments have been performed with a wide range of particle sizes in Newtonian and non-Newtonian fluids, resulting in multiple formulations describing the settling velocity of particles. Table 3 shows an overview of some of these formulas which are used in this thesis.

Table 3: List of relations for the prediction of the terminal settling velocity [44]

Author	Equation	For	
Rubby (1933)	$v_{tsv} = F \sqrt{d_p g (s - 1)}$	$d_p > 0.2 \text{ mm}$	(12)
	$F = \sqrt{\frac{2}{3} + \frac{36v_{kin}^2}{g(s-1)d_p^3}} - \sqrt{\frac{36v_{kin}^2}{g(s-1)d_p^3}}$		(13)
Zanke (1977)	$v_{tsv} = \left(\frac{10v_{kin}}{d_p} \right) \left(\sqrt{1 + 0.01 \frac{g(s-1)d_p^3}{v_{kin}^2}} - 1 \right)$	$0.1 \text{ mm} \leq d_p \leq 1 \text{ mm}$	(14)
Van Rijn (1989)	$v_{tsv} = \frac{g(s-1)d_p^2}{18v_{kin}}$	$d_p < 0.1 \text{ mm}$	(15)
	$v_{tsv} = 1.1 \sqrt{g(s-1)d_p}$	$d_p > 1 \text{ mm}$	(16)
	$v_{tsv} = \left(\frac{10v_{kin}}{d_p} \right) \left(\sqrt{1 + 0.01d^3} - 1 \right)$	$0.1 \text{ mm} \leq d_p \leq 1 \text{ mm}$	(17)
Cheng (1997)	$v_{tsv} = \frac{v_{kin}}{d_p} \left(\sqrt{25 + 1.2D_*^2} - 5 \right)^{1.5}$	Natural particles (shape factor 0.5 – 0.7)	(18)
	$D_* = d_p \left(\frac{g(s-1)}{v_{kin}^2} \right)^{\frac{1}{3}}$		(19)

Where: s = relative density $(\rho_p/\rho_f)[-]$, v_{kin} = kinematic viscosity $[\text{m}^2/\text{s}]$ and D_* = particle parameter $[-]$

More recently, Sadat et al (2009), Zhiyao et al. (2008) and others tried to increase the accuracy and application range of the theoretical formulas by fitting empirical relations on the available experimental data. This resulted in empirical formulas, which are applicable on a wider range of particle diameters and shapes.

Table 4: Empirical relation for the prediction of the terminal settling velocity [44][56]

Sadat et al (2009)	$v_{tsv} = 0.033 \frac{v_{kin}}{d_p} \left(\frac{g(s-1)d_p^3}{v_{kin}^2} \right)^{0.963}$	$D_* \leq 10$	(20)
	$v_{tsv} = 0.51 \frac{v_{kin}}{d_p} \left(\frac{g(s-1)d_p^3}{v_{kin}^2} \right)^{0.553}$	$D_* > 10$	(21)
Zhiyao et al. (2008)	$v_{tsv} = D_*^3 \frac{v_{kin}}{d_p} \left(38.1 + 0.93D_*^{\frac{12}{7}} \right)^{-\frac{7}{8}}$	Spherical and natural particles	(22)

The terminal settling formulas shown in the two tables above are applied and compared in the next chapter. For the COMSOL modelling part in Chapter 5, the built in semi-empirical Schiller-Naumann drag model has been used to define the drag coefficient and thereby to determine the terminal settling velocity of particles. The Schiller-Naumann formulation is shown below and is also included in the preliminary calculations discussed in the next chapter.

Table 5: Schiller-Naumann drag model [46]

Schiller and Naumann (1933)	$C_d = \frac{24}{Re_p} (1 + 0.15Re_p^{0.687})$	$Re_p \leq 1000$	(23)
	$C_d = 0.44$	$Re_p > 1000$	(24)

2.4.2. Influence of particle shape

The majority of natural particles and cuttings created during the drilling process have irregular shapes rather than the assumed perfect sphere shape. The effect of particle morphology on settling velocity is often neglected in most settling models due to their empirical nature. The non-spherical particle shape influences the drag on the particles and makes the drag expressions less trivial. During the settling process particles orientate themselves to maximize the drag force by having their maximum area horizontal. This increase in the drag force results in a lower particle settling velocity based on eq. (8). To account for this reduction in settling velocity, a defined shape factor (ψ [-]) is often introduced in eq. (8) resulting in:

Terminal settling velocity of a particle including the shape factor[53]:

$$v_{tsv} = \sqrt{\frac{4g(\rho_s - \rho_f)d_p\psi}{3C_d\rho_f}} \quad (25)$$

The shape factor takes the deviations from a perfect sphere and non-spherical particle into account. For natural sediments like sand the shape factor is generally chosen to be 0.7.

Fang (1992) concluded that particle morphology also influences the settling patterns of the particles. By performing settling experiments in viscous fluids with various cuttings, he was able to observe two settling patterns being stable and swinging fall as shown in Figure 14.

The two observed fall patterns have been found to be related to the particle Reynolds number. For $Re_p < 100$ the fall pattern was observed as stable and for $Re_p > 100$ the fall pattern being swinging.

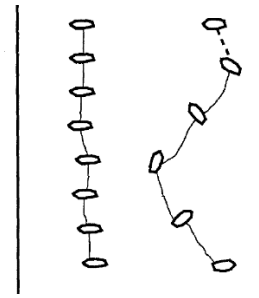


Figure 14: Particle settling pattern [24]

2.4.3. Influence of particle concentration

The previous discussed formulations were related to single particle settling behaviour. When the settling of multiple particles is considered, inter particle influences decrease the settling velocity of the individual particles. This effect is known as hindered settling and is caused by the returning fluid flow, the increased pressure gradient in the fluid and the inter-particle effects. The effects of hindered settling is generally taken into account by equation (26), where the terminal settling velocity v_{tsv} is multiplied with the hindered settling function $f(c)$:

$$v_{slip} = f(C_{sol}) \cdot v_{tsv} \quad (26)$$

Where: v_{slip} = the difference between the average velocities of the fluid and particles [m/s] and C_{sol} = the solids concentration [-]

The hindered settling function $f(C_{sol})$ is often described by the following well known empirical Richardson & Zaki (1954) equation [40]:

$$f(C_{sol}) = \begin{cases} (1 - C_{sol})^{n_{RZ}-1} & \text{For } C_{sol} < C_{sol,max} \\ 0 & \text{For } C_{sol} = C_{sol,max} \end{cases} \quad (27)$$

Where: n_{RZ} = Richardson & Zaki index [-] and $C_{sol,max}$ = maximum solids concentration [-]

The Richardson & Zaki index is a function of the particle Reynolds number and has been determined based on experiments performed with solids concentrations between $0.05 < C_{sol} < 0.65$. The following Richardson & Zaki index expressions are reported by Richardson & Zaki.

$$\begin{array}{llll} Re_p < 0.2 & \text{for} & n_{RZ} = 4.65 & \\ 0.2 \leq Re_p < 1 & \text{for} & n_{RZ} = 4.35Re_p^{-0.03} & \\ 1 \leq Re_p < 200 & \text{for} & n_{RZ} = 4.45Re_p^{-0.1} & \\ Re_p \geq 200 & \text{for} & n_{RZ} = 2.39 & \end{array} \quad (28)$$

To obtain a single expression for determining n_{RZ} , Rowe (1987) modified the four Richardson & Zaki index expressions into a single smoothed logarithmic expression as shown in eq. (29). The equation is valid for particle Reynolds numbers between $0.2 < Re_p < 10^3$ and solid concentrations between $0.04 < C_{sol} < 0.55$ [43].

$$n_{RZ} = \frac{4.7 + 0.41Re_p^{0.75}}{1 + 0.175Re_p^{0.75}} \quad (29)$$

For the simulations in chapter 5, the Krieger & Dougherty (1959) viscosity model is used to account for particle concentration effects. This model includes the effects of particle concentration by adjusting the carrying fluid viscosity based on solids concentration in the solution. A higher concentration of solids results in a higher apparent viscosity and thereby a lower slip velocity. The Krieger & Dougherty model is defined as [30]:

$$\mu_{eff} = \mu_{app} \left(1 - \frac{C_{sol}}{C_{sol,max}} \right)^{-2.5C_{sol,max} v^*} \quad (30)$$

Where: μ_{eff} = the effective viscosity of the carrying fluid [Pa·s] and v^* = a dimensionless parameter [-]

This model uses a maximum solids concentration of $C_{sol,max} = 0.62$ and a parameter value of $v^* = 1$ for solids.

2.4.4. Influence of particle size distribution

The previous formulations for settling were associated with particles having the same particle diameter. However when multiple particles with different diameters are present in the solution, a different approach is considered. Large particles for example can create strong return flows during settling which can drag smaller particles upwards. A possible simple approach is determining the slip velocity of each particle size fraction i separately as described by Mirza and Richardson (1979) [41]:

$$v_{slip,i} = v_{tsv} \cdot (1 - C_{sol,total})^{n_{RZ,i}-1} \quad (31)$$

Where: $v_{slip,i}$ = slip velocity of fraction i [m/s], $n_{RZ,i}$ = Richardson and Zaki index of fraction i [-] and $C_{sol,total}$ = total solids concentration [-]

This approach however is not suited for particle size distributions where large differences in particle size or particle density are present.

Since the particles entering the critical settling zone of the settling tank have small variety in particle sizes (approx. $d_p < 1 \text{ cm}$), particle size distribution effects are neglected in the preliminary calculations. For the COMSOL Multiphysics simulations only one particle size is used for each simulation.

2.4.5. Influence of clay particles

Clay particles are very fine particles ($d_p < 2\mu\text{m}$) and can be considered as non-settling, however they can influence the settling of relatively larger particles. When a significant amount of clay is mixed with water, the clay particles can change the density and fluid behaviour of the clay-water mixture.

The fluid density change is related to the addition of the heavier clay material resulting in a mixture with a higher density than water. The density of WBM composes of a mixture of water and bentonite clay is generally around 1100-1200 kg/m³. The density can be higher when weighting materials such as barite are used. A higher density of the carrying fluid results directly in a lower settling velocity according equation (8) the terminal settling.

A significant concentration of clay in water can influence the fluid behaviour by changing it from a Newtonian fluid to a non-Newtonian fluid. The non-Newtonian drilling fluid behaviour has been briefly introduced in section 2.2.2. Non-Newtonian fluids like WBM have a yield point and a shear dependent viscosity, which is in general higher than the viscosity of water. A higher viscosity of the carrying fluid results in more drag according to equation (9) and therefore a lower terminal settling velocity.

2.4.5.1 Influence of yield stress, gel strength and shear thinning

Viscoplastic non-Newtonian fluids exhibit a yield stress throughout their unshared state. This yield stress is able to support a particle in the fluid for indefinite time, without letting it settle in the carrying fluid. The question if a particle will settle in such fluids is dependent on the static equilibrium of the forces acting on the submerged particle. The force equilibrium is shown in Figure 15 for a spherical particle. For simplification it is assumed that the support force (F_{sup}), is the result of the fluid yield on a cylindrical surface around the particle.

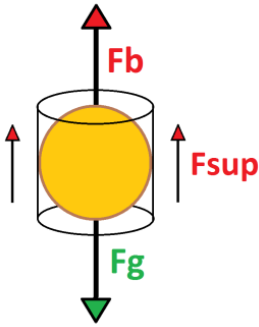


Figure 15: Forces acting on a suspended sphere particle in a viscoplastic fluid

Static equilibrium is reached when:

$$F_g - F_b = F_{sup} \quad (32)$$

Where: F_g = gravitational force [$\text{kg}\cdot\text{m}/\text{s}^2$] and F_b = buoyancy force [$\text{kg}\cdot\text{m}/\text{s}^2$]

The net gravitational force acting on the spherical particle:

$$F_g - F_b = \pi(\rho_p - \rho_f)g \frac{d_p^3}{6} \quad (33)$$

Where: ρ_p = particle density [kg/m^3], ρ_f = fluid density [kg/m^3] and d_p = particle diameter [m]

The support force acting on cylindrical surface around the particle:

$$F_{sup} = d_p^2 \cdot \pi \cdot \tau_{eff} \quad (34)$$

Where: τ_{eff} = effective yield stress [Pa]

The equations (32)-(34) represent a static equilibrium, which is considered by many researchers resulting in the following critical yield stress criterion:

$$\tau_{eff} \geq \alpha_{cr}(\rho_p - \rho_f) d_p g \quad (35)$$

Where: α_{cr} = dimensionless parameter [-]

When the effective yield stress exceeds the critical yield stress, particles will be supported by the carrying fluid and will not settle. The practical values used for the dimensionless parameter α_{cr} range between 0.048 and 0.2 as reported by Chhabra (1993).

The gel strength of WBMs can be seen as the effective yield stress. When the gel strength of a water based drilling fluid is measured directly after being sheared, and repeatedly measured after increasing longer time periods, the values obtained will be found to be increasing at a decreasing rate until a maximum value of gel strength is reached. The gel strength becomes the fluid yield stress, since the fluid will not flow until the applied stress exceeds the gel strength.

The build-up of gel strength is a thixotropic behaviour and is caused by the clay platelets arranging themselves in the fluid. When the fluid is subjected to a constant rate of shear after being at rest, the gel strength breaks down until equilibrium between the structure-building and structure-disrupting is reached.

Drilling fluids are characterized by a shear-thinning region in the low shear range, which is represented by the exponential part of the consistency curve shown in Figure 8. Shear-thinning behaviour depends on the balance between the Brownian and hydrodynamic forces influencing the build-up, breakdown and shear ordering of the clay microstructure. With increasing shear, the viscosity decreases gradually until maximum shear ordering is reached and build-up of clay structures can be neglected. At this point the viscosity attains its minimum value and becomes independent of the shear. The region where this phenomenon starts occurring is characterized by the straight part of the consistency curve shown in Figure 8.

Researchers like Ansley & Smith (1967) studied the settling of particle in non-Newtonian fluids and described methods to implement the viscoplastic behaviour in the settling velocity equations. This resulted in almost similar settling equations as for Newtonian fluids. Other studies suggested that the viscoplastic behaviour is weakened or destroyed by shear stresses due to flow or turbulence Song and Chiew (1997).

Since no stationary cases are evaluated in this thesis and the drilling fluid is assumed to be flowing in all situations, it can be presumed that gel strength build-up in the drilling fluid will be limited. Therefore, the influence of the non-Newtonian behaviour is limited to an increased shear dependent apparent viscosity.

2.4.6. Influence of turbulence

The vertical settling of particles towards the bottom of a tank is in the previous sections only described by the settling velocity of the suspended particles. However, turbulent flow and settling conditions can influence this process by introducing diffusive transport of particles. Particles can be carried in different direction due to these forces and thereby increase the time required to settle. These effects are generally accounted by using advection and diffusion equations.

The settling velocity of particles relative to the fluid is also influenced by turbulent fluctuations. A particle subjected to these fluctuations will oscillate, resulting in a different average vertical velocity. This difference can either be positive or negative and therefore increase or decrease the particle settling velocity. The influence of turbulent fluctuations is generally expressed in a variation of particle drag coefficients.

Turbulence also leads to the creation of additional shear in the fluid. The additional shear can influence the viscosity of non-Newtonian fluids. Shear-thickening fluid will have an increased viscosity, while the viscosity of shear-thinning fluids like drilling fluid is reduced. A lower fluid viscosity directly influences the terminal settling velocity by equation (8), resulting in an increased particle settling rate.

2.4.7. Influence of temperature and pressure

During a drilling operation, the drilling fluid is exposed to varying temperatures and pressure conditions. These variations can influence the rheological properties of the drilling fluid significantly and need to be considered. The downhole conditions for example, can vary drastically from the ambient conditions at the surface reaching over 1400 bars of pressure while temperatures can pass 200°C. Both influences are also important for the drilling fluid treatment process, especially when the pressurized separation tank is studied.

The temperature and pressure differences can influence the state and viscosity of the drilling fluid, but also particle-particle interactions within the suspension can change. These changes all together can result in an altered flow behaviour, which will influence the settling of particles in the separation tank.

Briscoe et al. (1994) studied the influence of pressure and temperature on water based drilling fluids, using the High Pressure High Temperature (HPHT) rolling ball viscometer. Since the Bingham model is used to describe the drilling fluids, the influence of temperature and pressure are only presented for the yield point and plastic (Bingham) viscosity. Figure 16 presents the Influence of temperature and pressure on plastic viscosity and yield stress for a weighted drilling fluid (clay 6%, barite 60%, mass).

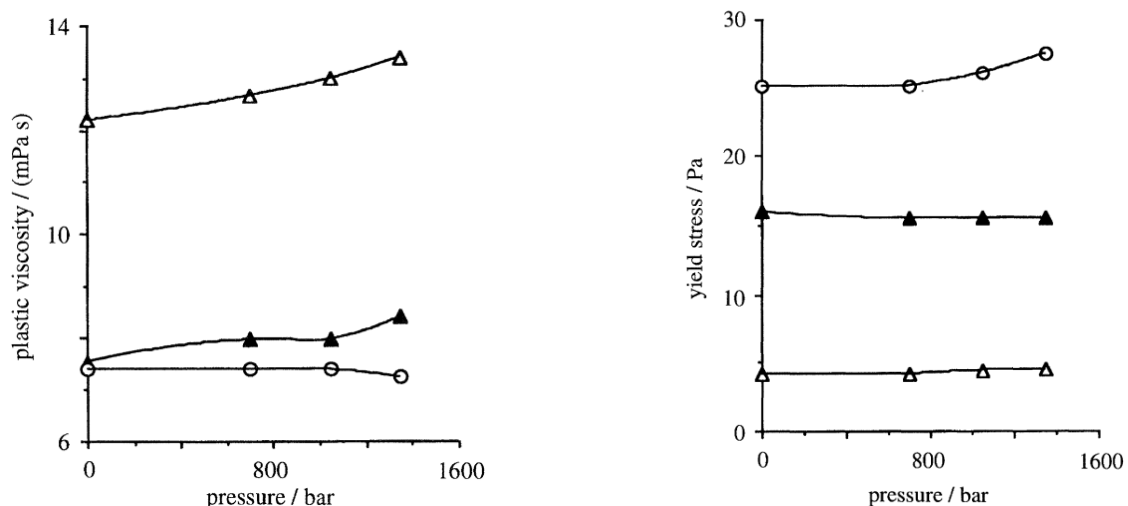


Figure 16: Influence of temperature and pressure on viscosity and yield stress [12]. (Δ, T = 27°C. ▲, T = 65°C. ○, T = 85°C.)

Briscoe et al. concluded that the plastic viscosity and apparent viscosity decreased with increasing temperature. The plastic viscosity on the other hand, increased slightly with increasing pressure at low temperatures, this increase was greater compared to the unweighted drilling fluids. The yield stress observations showed that the yield stress is independent of pressure at low temperatures, but increases with higher pressure at high temperatures.

2.5. Influence of vibrations on non-Newtonian drilling fluids

Deshpande & Barigou (2001), Lapin et al (2010) and others studied the effects of vibrations on non-Newtonian fluid in pipes. The results of these studies showed that introducing vibrations to non-Newtonian fluids can increase or decrease the flow rate, depending on if the fluid has shear thinning or shear thickening characteristics. While Newtonian fluids showed no change in flow rate, a significant difference in flow rates was observed in non-Newtonian fluids. The observed enhancing effects were even greater when extremely shear thinning fluids were used. The enhancing effect increased with increasing frequencies and amplitude, however different combination of both corresponding to the same peak acceleration showed no significant changes on the enhancing effects.

Imposing an external pressure gradient and thereby increasing the flow rate in the experiments of Deshpande & Barigou, resulted in a reduction of the vibrational enhancing effects. It is suggested that under a higher pressure gradient the steady-state flow in the pipe is high and the extra flow generated by the oscillations becomes small in comparison. These observations are supportable by considering the shear related viscosity behaviour of shear thinning fluids as shown in the consistency curves in Figure 8. The additional shear rate induced by the vibrations becomes relatively smaller compared to the high shear rate generated by the high flow rates. The viscosity decrease will therefore be smaller, resulting in a relative smaller increase of flow rate.

The enhancing effects of vibrations on non-Newtonian fluids can also be found in the study of Frad et al (2007). In this study the viscous properties of different types of drilling fluids were measured in a Fann viscometer, as they were imposed to horizontal vibrations of different frequencies (40, 80, 120 Hz) and fixed amplitude of around 0.75 mm. The obtained results showed significant changes in the rheological properties of the drilling fluids related to changes in the particle structure. The largest viscosity changes are observed for bentonite based solutions, while the polymer (Poly Anionic Cellulose, PAC) based solutions did not show any changes.

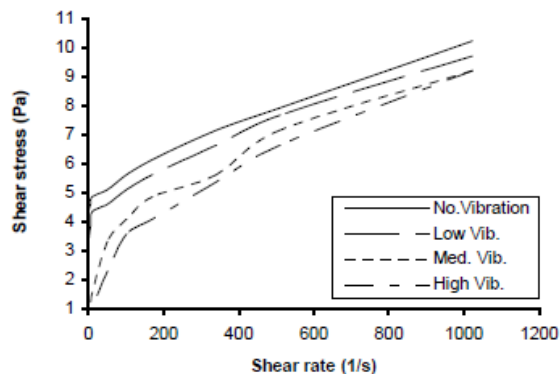


Figure 17: Consistency curve drilling fluid based on clay and barite solution in water [26]

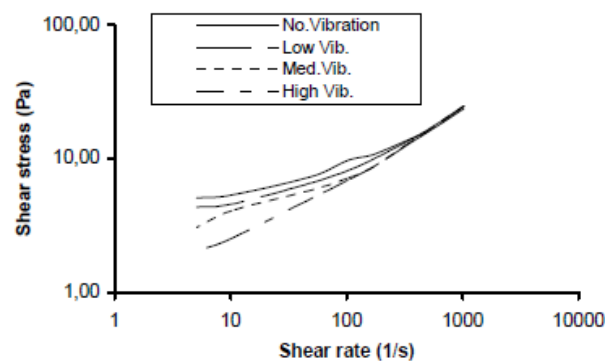


Figure 18: Consistency curve drilling fluid based on clay solution in water [26]

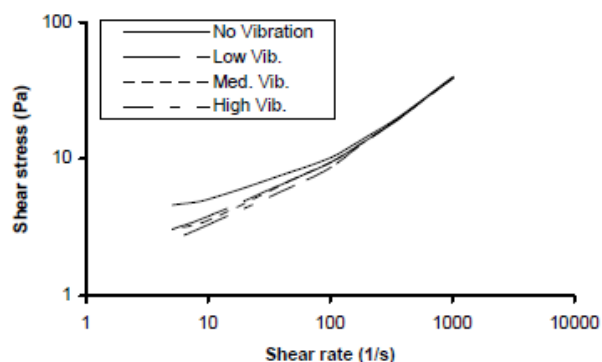


Figure 19: Consistency curve oil based drilling fluid [26]

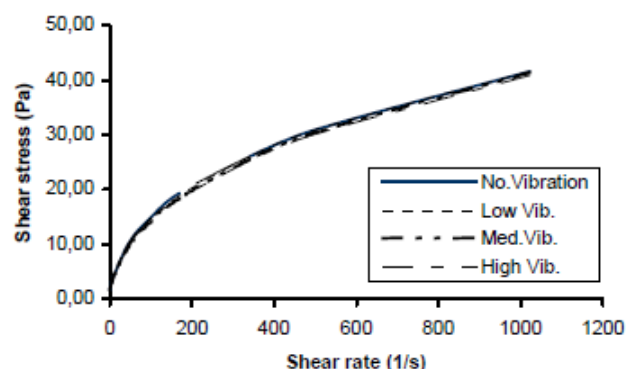


Figure 20: Consistency curve PAC solution in water [26]

2.6. Settling in horizontal tanks

Sedimentation is one of the oldest and commonly used treatment processes in the waste water treatment industry. This technique is excessively used in water treatment plants for waste water treatment in large rectangular or circular sedimentation tanks. A brief literature review is included in this paragraph, since these tanks show many similarities with our separator tank. The main focus is on hydrodynamic phenomena, which is essential for the design of a proper functioning settling tank.

2.6.1. Unstable flow conditions

Unstable flow conditions in settling tanks reduce the particle settling efficiency due to the movement of particles in different directions rather than the desired settling direction. Turbulence, density flows and return currents are often the reason behind the instable flow conditions.

2.6.1.1 Turbulence

A turbulent flow regime will cause short-term pressure fluctuations in the settling tank. These fluctuations can lead to oscillation of particles and thereby influence the settling of particles. The small particles are more sensitive to these oscillations since the response is faster than the response of the large particle. Avoiding turbulent flow conditions near the sedimentation bed and in the settling zone is therefore an important aspect when designing a sedimentation tank. Flow diffusers or baffles are often used to reduce the turbulence at the inlets of sedimentation tanks.

2.6.1.2 Density flows

When a high density fluid enters a tank containing a lower density fluid, density flows will cause the fluid to flow to the bottom due to gravity. This phenomenon is present in sedimentation tanks and is referenced to as density flows. The occurrence of these flows is preferred and often amplified by adding baffles in the tank, since density flows enhance the initial settling.

2.6.1.3 Return currents

Return currents are undesired flows that generally occur in open sedimentation tanks, where wind blows on the water surface and causes a return flow. Other sources for return flows are turbulence and density flows. When a return current occurs the flow in the tank circulates instead of flowing from the inlet to the outlet. Particles caught in these currents can be dragged in undesired directions and thereby reduce the settling efficiency of the sedimentation tank. The stability of flow can be expressed in the Froude number [37]:

$$Fr = \frac{v_0^2}{g \cdot R} \quad (36)$$

Where: Fr = Froude number [-], v_0 = fluid velocity [m/s] and R = the hydraulic radius [m]

$Fr > 1 \cdot 10^{-5}$ for Stable flow
 $Fr < 1 \cdot 10^{-5}$ for Unstable flow

2.6.2. Resuspension

The resuspension of particles is an undesired effect, which occurs near the sedimentation bed in the tank. High flow velocities near the bed caused by high inlet velocities or turbulence are the common causes of resuspension. Resuspension of particles or so called bottom scour occurs when the shear forces of the carrying fluid on a particle exceed the resisting frictional forces. The critical scour velocity initiating scour of deposited particles is given by the Camp (1946) based on to the force equilibrium in Figure 21.

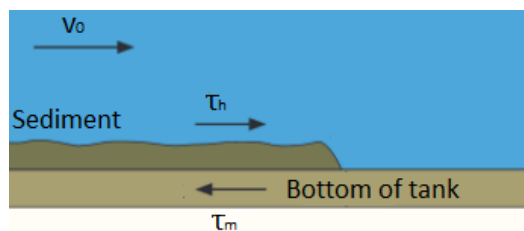


Figure 21: Bottom scour in a sedimentation tank

The hydraulic shear of water on a spherical particle is defined as [22]:

$$\tau_h = \frac{\lambda}{8} \cdot \rho_f \cdot v_{sc}^2 \quad (37)$$

The mechanical shear of particles is defined as [22]:

$$\tau_m = \beta \cdot (1 - n_{por}) \cdot (\rho_s - \rho_f) \cdot g \cdot d_p \quad (38)$$

Combining equations (37) and (38) results in the Camp expression for the critical scour velocity [22]:

$$v_{sc} = \sqrt{\frac{8 \cdot \beta \cdot (1 - n_{por}) \cdot (\rho_s - \rho_f) \cdot g \cdot d_p}{\lambda \cdot \rho_f}} \quad (39)$$

Where: v_{sc} = critical scour velocity [m/s], τ_h = hydraulic shear [N/m²], τ_m = mechanical shear [N/m²], λ = hydraulic viscous friction factor (0.03)[-], β = mechanical friction factor 0.1[-] n_{por} = porosity 0.5[-] and d_p = particle diameter [m]

2.6.3. Flocculation

Flocculated settling is a commonly used settling method in the wastewater treatment industry. Small flocs bind together forming larger flocs, which can settle much faster. This method is often enhanced by mixing additives into the wastewater. The additives increase the flocculation rate of the particles and thereby increase the efficiency of the sedimentation tank. Using flocculated settling in the drilling fluid separator is however not preferred, since additives can influence the drilling fluid rheology.

2.7. Filtration

Filtration is a commonly used separation method in today's industries. Filtration processes are capable of removing solids particles, microorganisms or droplets from liquids and gasses by depositing them on a filter medium. The filter medium is only permeable to the fluid phase in the mixture, causing the fluid to pass while the particles retain on the surface or within the filter medium. The permeation of the fluid phase through the filter medium is related to a pressure gradient. This pressure difference can be produced by a pressurized fluid, vacuum, gravity or centrifugal force and is often called pressure filtration.

Filtration of a mixture can be described by four filtration techniques presented in Figure 22.

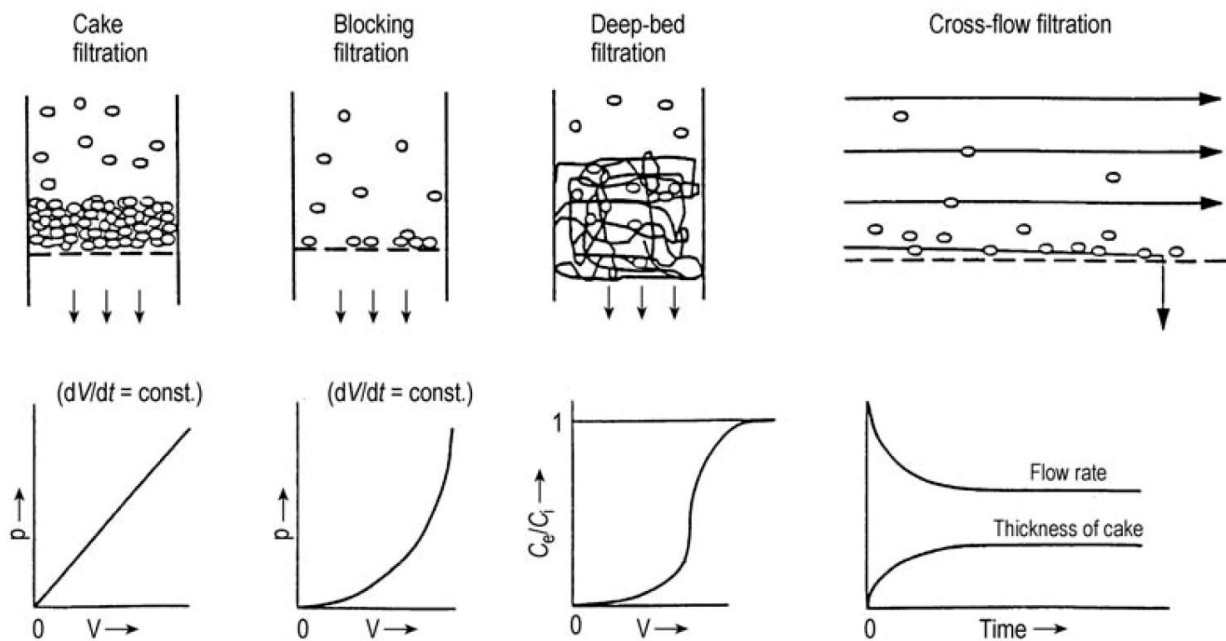


Figure 22: Filtration models [42]

Cake filtration is the most common filtration techniques where the suspended particles are deposited on the upstream of the filter medium. As soon as the filter cake forms, the subsequent part of the filtration will take place on top of the cake. The filter medium will only provide support to the filter cake on top of the filter medium. With increasing deposition of particles on top of the filter medium, the pressure drop will increase linearly, proportional to the quantity of the deposited particles.

Blocking filtration is another technique that is used in many applications. In this model, the pressure drop is caused by particles blocking the filter medium pores. Blocking of pores can also occur in the filter cake instead of the filter medium causing the same effect. The pressure drop increases exponentially with the quantity of particles filtered, while the number of open pores approaches zero.

Deep bed filtration occurs when the particles are retained in the deep filter layer. Deep bed filtration is commonly seen in sand filters used in wastewater treatment and drinking water clarification processes. The separation effectiveness of these filters is related to the quantity of retained particles in the sand filter bed. As the quantity of these particles increases, the filtration effectiveness decreases eventually causing inflow concentration of particles approaching the outflow concentration.

In cross filtration the mixture flows at high velocities tangentially to the filter medium, preventing the formation of filter cake. During this process, only a small flow of fluid passes the filter medium creating a certain layer of particles on top of the filter. After the initial deposition of particles, equilibrium is formed between the deposition and removal of particles due to hydrodynamic forces acting on the particles.

The Darcy's law describes the resistance of flow of a porous medium, being a filter medium or filter cake. Considering Darcy's law and a flow through a filter cake, the pressure drop through the filter can be described as [54]:

$$\Delta p = q \cdot H_{cake} \cdot \mu \cdot \alpha_H \quad (40)$$

Where: Δp = pressure difference [Pa], q = specific flow rate [m/s], H_{cake} = cake thickness [m], μ = dynamic viscosity [Pa·s] and α_H = specific filter resistance [1/m²]

The filter resistance is often written as the filter permeability k [m²]:

$$k = \frac{1}{\alpha_H} \quad (41)$$

There are many studies where researches have looked into ways of improving the filter effectiveness. Most of these studies are performed considering Newtonian fluids however their results can also be useful for the filtration of non-Newtonian fluids.

An example of a study on non-Newtonian fluid based filtration is the study of Hoberock (1980). In his study, the influence of the filter orientation and vibrations on the filter performance have been evaluated. The results indicate that a greater flow capacity can be realized by optimizing the filter orientation and vibration frequency.

The so called sand screens are filter screens or gravel beds used to separate sand from many different kinds of flows. These kinds of screens are commonly used in the industry and are therefore well known. To select the right filter screen openings, several empirical formulations are available to predict the required filter openings based on the sand PSD. These formulations might not be accurate for clay suspension, but can still give an indication of the required filter screen openings. The various criterions listed in Table 6, describing the required filter openings to separate the sand particles from the flow:

Table 6: Empirical relations to select for selecting sand screens

Coberly (1937)	$2 \cdot d_{90}$
Saucier (1974)	$5 \sim 6 \cdot d_{50}$

Where: d_x = refers to the particle size diameter for which x percent of the sample by weight passes a sieve with an opening equal to d . The d_{50} is for example the median grain size and d_{90} indicates the sieve opening retaining the largest 10%.

3. Preliminary calculations

Based on the performed literature review, preliminary calculations have been carried out to model the effects and effectiveness of solids removal by gravitational settling in settling tanks. This section summarises the performed calculations in MATLAB and the obtained results.

3.1. Ideal horizontal settling tank model

The ideal horizontal settling tank model is used to simplify the processes in the settling tank and thereby reduce the complexity of the calculations. The ideal settling tank is defined by Camp (1946) as a tank that can be divided into four zones:

1. The inlet zone where the inflow is uniformly distributed over the available cross-sectional area of the tank resulting in a uniform concentration of particles at the left side of the sedimentation zone.
2. The sedimentation zone where a laminar uniform horizontal flow is present in all parts of the sedimentation zone.
3. The outlet zone where the treated fluid is collected and directed to the outlet without causing resuspension of particles.
4. The sludge zone where settled particles are accumulated and are removed from the system continuously. When a particle reaches the sludge zone it is definitively removed from the system.

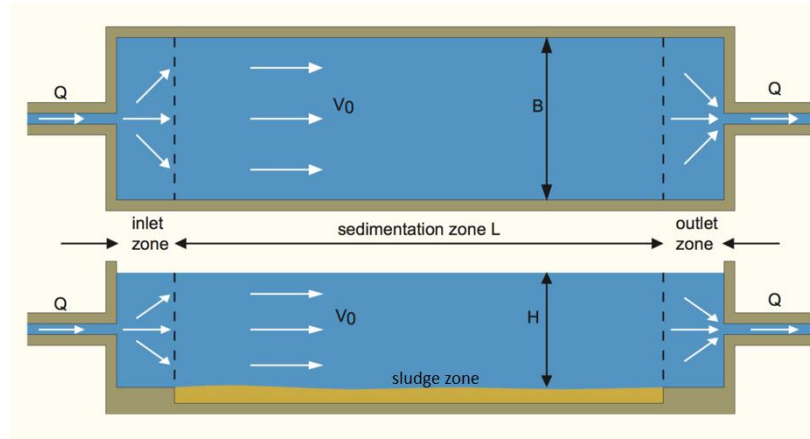


Figure 23: Overview of an ideal horizontal flow settling tank [22]

Since the horizontal flow in the sedimentation zone is assumed to be uniform, particles settling in this zone will have straight settling trajectories as shown in Figure 24.

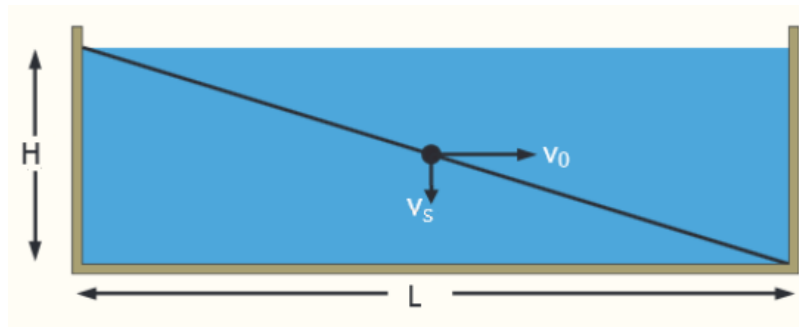


Figure 24: Settling trajectory in horizontal flow sedimentation zone [22]

A particle entering the sedimentation zone from the top left corner can settle if it reaches the sludge zone at the bottom before reaching the outlet zone on the right side. This criterion for complete settlement of particles in an ideal settling tank can be written as [22]:

$$\frac{H}{v_s} \leq \frac{L}{v_0} \quad (42)$$

Simplification of this criterion is possible by substituting the equations for the horizontal flow in a rectangular tank and the surface loading of a settling tank [22]:

$$v_0 = \frac{Q}{B \cdot H} \quad (43)$$

$$q = \frac{Q}{B \cdot L} \quad (44)$$

Resulting in:

$$\frac{H}{v_s} \leq \frac{B \cdot H \cdot L}{Q} \Rightarrow \frac{1}{v_s} \leq \frac{1}{q} \Rightarrow v_s \geq q \quad (45)$$

Where: v_s = settling velocity [m/s], v_0 = horizontal flow velocity [m/s], q = surface loading [m/s], Q = flow rate [m³/s] and H, B, L is the height, width and length of the sedimentation zone in [m]

Particles having a smaller settling velocity than q can still settle in the settling tank if they enter the sedimentation zone at a lower height. These cases have been neglected and only the complete removal of particles is considered in the calculations.

The characteristics of the ideal settling tanks are validated by the calculation of the Camp stability number for stable flow, section 2.6.1.3. The absence of resuspension is validated by verifying the criterion for bottom scour, section 2.6.2. The laminar flow condition in the settling zone are verified by determining the flow Reynolds Number in the sedimentation tank [22]:

$$Re = \frac{v_0 \cdot R}{\nu_{kin}} \quad (46)$$

Where ν_{kin} = kinematic viscosity [m²/s] and R = hydraulic radius [m] defined for a completely filled tank as:

$$R = \frac{B \cdot H}{2(B + H)} \quad (47)$$

The settling velocities of the particles in the sedimentation tank are determined by using the settling models described in section 2.4.1. The particle concentration effect reducing the settling rate is also included in the calculation using the Richardson & Zaki formulation described in section 2.4.3.

The MATLAB code including the calculation model is attached in Appendix E.

3.2. Input parameters

The input parameters used in the MATLAB calculations are shown in Table 7.

Table 7: Input parameters for MATLAB

Component	Parameter	Values	Unit
Tank	Length	5	[m]
	Height	2.5	[m]
	Width	2	[m]
Particles	Diameter	0.01 – 10	[mm]
	Specific weight	2650	[kg/m ³]
	Particle concentration	5, 10 and 20	[%]
Fluid	Inflow	1000, 2000, 3000 and 4000	[L/min]
	Specific weight	1300	[kg/m ³]
	Apparent viscosity	0.1, 0.2, 0.4, 0.6 and 0.8	[Pa·s]

The chosen parameter values are based on a variety of assumptions and boundary conditions:

- The settling tank dimensions are chosen based on the standardized container sizes.
- The particle diameter range is chosen based on the expected settling range.
- The specific weight of the particles is chosen to match the specific weight of sand.
- The particle concentration and sedimentation bed thickness are assumed based on practice.
- The inflow rate is based on the reference drilling logs extended with parallel tank options.
- The specific weight of the drilling fluid is based on a general weighted drilling mud.
- The apparent viscosity is derived from reference drilling logs.

The reference drilling logs are attached in Appendix C.

3.3. Results of preliminary calculations

This section presents the results of the MATLAB model describing an ideal horizontal settling tank. The results are presented in graphs where the tank surface loading parameter q is plotted against the slip velocity (v_{slip}). Complete settlement of particles occurs when $v_{slip} \geq q$.

3.3.1. Differences between different particle settling models

The particle settling models covered in the literature review (Chapter 2) have been used to predict the terminal settling velocity of the submerged particles. As expected, the obtained results showed differences in the predicted terminal settling velocities. As shown in Figure 25, the differences are negligible for small particles, but become larger with increasing particle diameter.

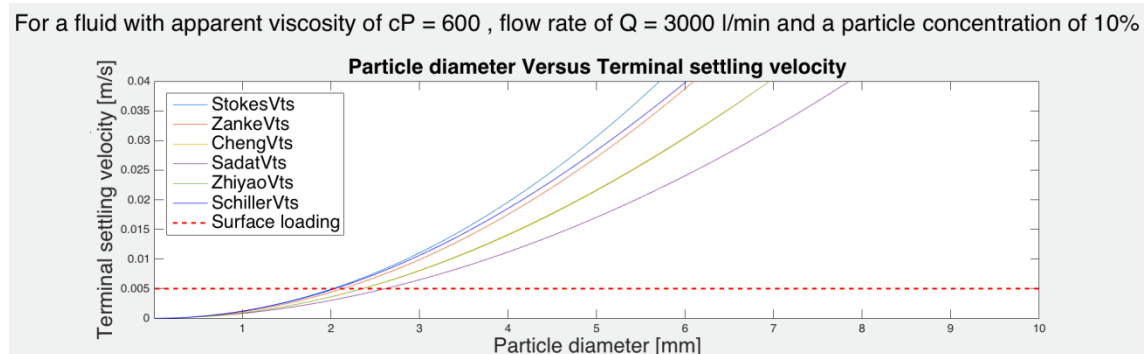


Figure 25: Difference between settling models terminal settling velocity

Calculations performed with different parameter sets showed that the Stokes settling model predicts the highest terminal settling velocity, whereas the empirical model from Sadat et al. shows the lowest prediction.

Based on the results shown in Figure 25, it can be seen that the settling model choice significantly affects the prediction of the settleable particle diameter. The sensitivity of the chosen settling model on the terminal settling velocity prediction can therefore be assumed to be high.

The Schiller & Naumann drag model used by COMSOL to predict the settling behaviour of particles has been included in the results shown in Figure 25. The value of terminal settling velocity from the Stokes model is used as an input and is iterated five times to obtain stable prediction from the Schiller & Naumann drag model. The model predicts comparable terminal settling velocities as the Stokes model in the small diameter range, whereas the predictions approaches the Zanke model for larger diameters.

The particle Reynolds numbers obtained from the calculations were within the laminar regime. The same trend as seen in the terminal settling velocity plots can be observed. The particle Reynolds number plot for the complete particle range is shown in Figure 26.

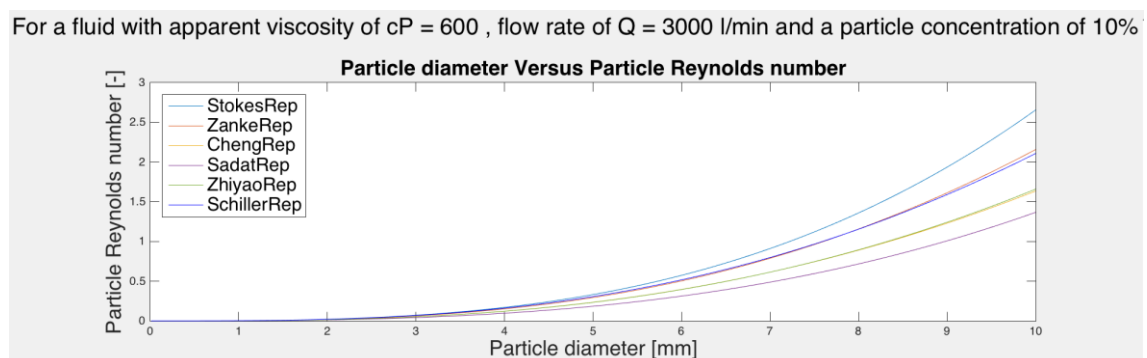


Figure 26: Difference between particle Reynolds numbers

3.3.2. The effect of particle concentration on settling

The Richardson & Zaki equations have been used to correct the terminal settling velocity and obtain the particle slip velocity. As expected this correction resulted in a reduction of the terminal settling velocity as shown in Figure 27. As the particle concentration is reduced the slip velocity approached the terminal settling velocity predicted in Figure 25.

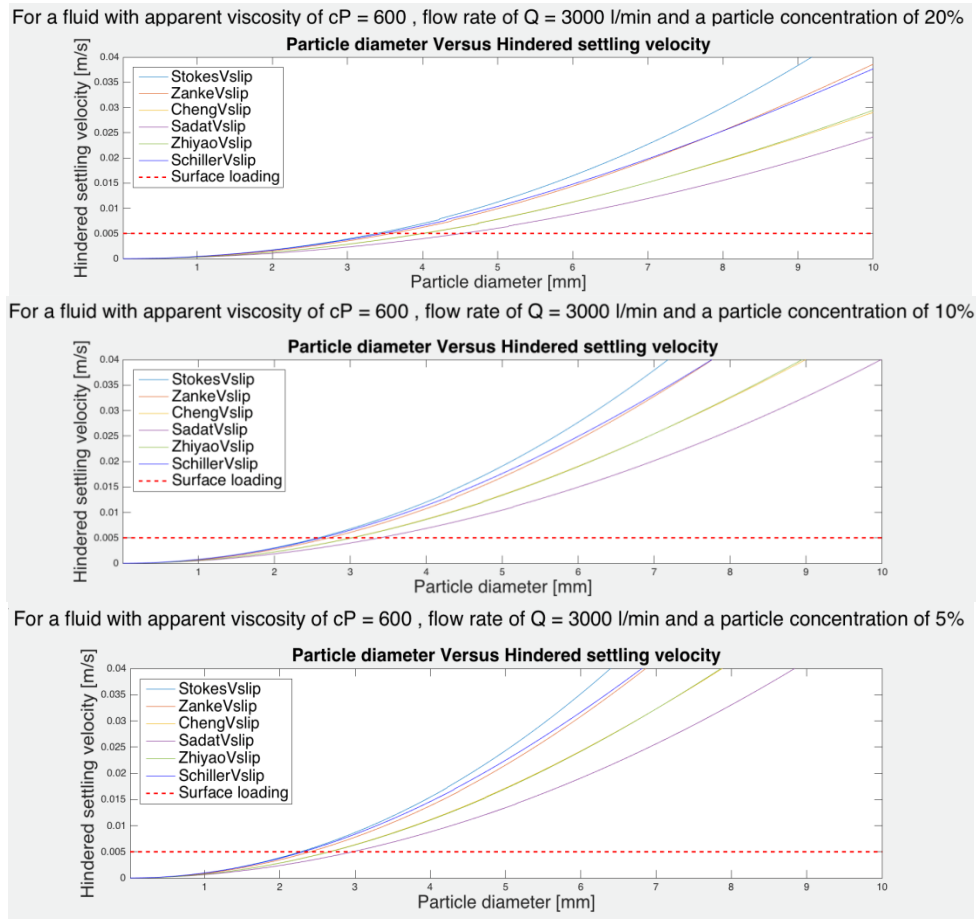


Figure 27: Influence of hindered settling on the particle slip velocity

The results point out that the particle slip velocity and thereby the particle settling is sensitive to fluctuations of the particle concentration. High particle concentrations can reduce the slip velocity significantly, increasing the minimal settleable particle diameter. Figure 28 summarizes the decrease in minimal settleable particle size with increasing particle concentration, based on the specified model parameters in Figure 27.

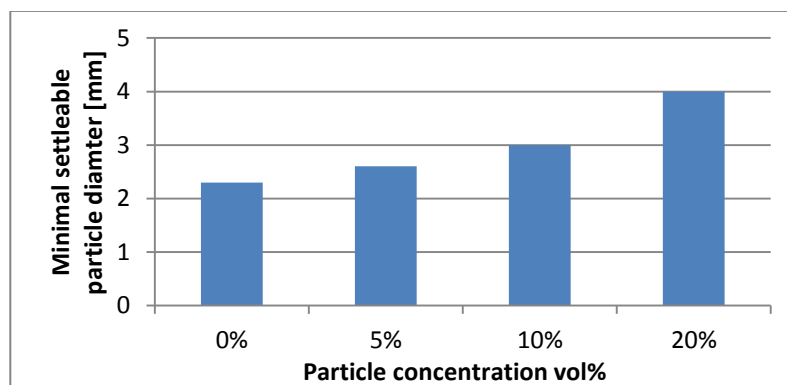


Figure 28: Increase of the settleable particle size due to increasing particle concentration

3.3.3. The effect of flow rate on settling

The flow rate in the settling tank characterizes the retention time of the particles in the settling tank. Fluctuations in flow rate can therefore influence the settling efficiency in the tank. The effects of flow rate on the settling efficiency have been studied and are shown in Figure 29.

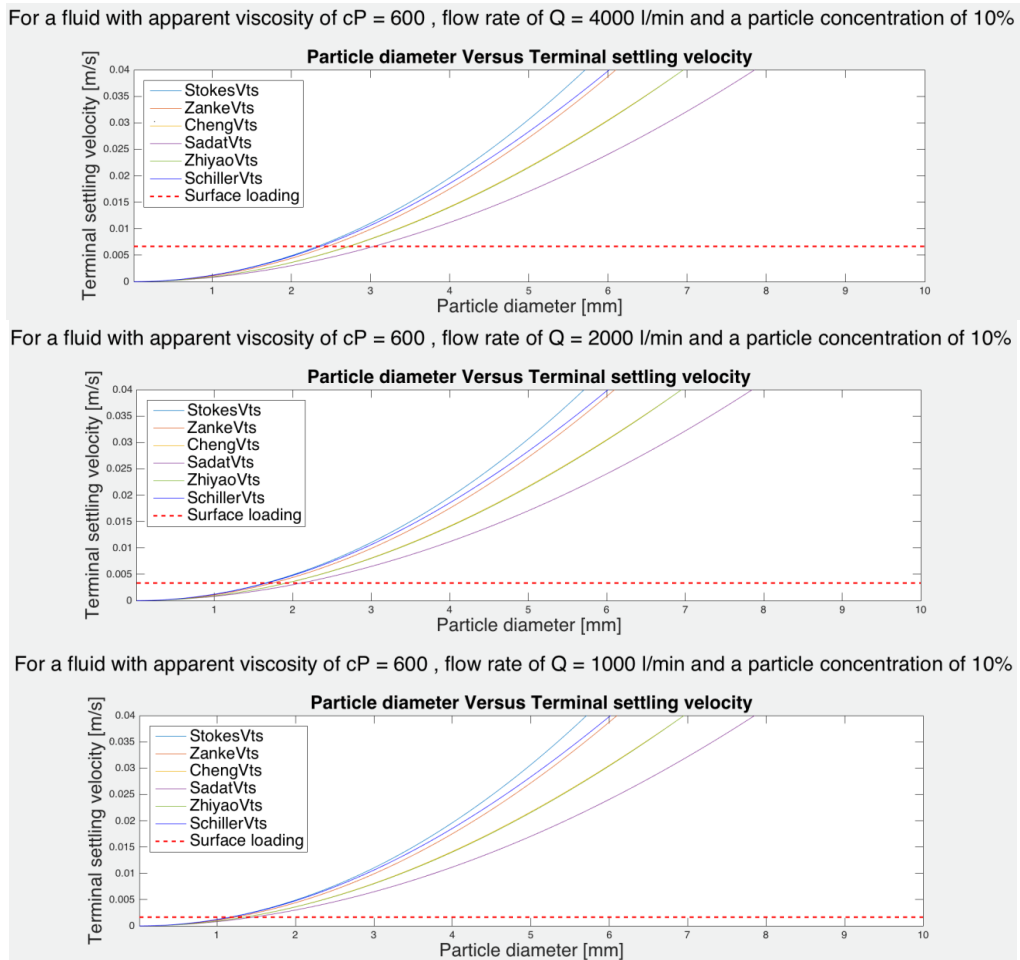


Figure 29: Increasing settling efficiency with decreasing flow rate

The results indicate that reducing the flow rate in the tank increases the settling efficiency. This increase in minimal settleable particle size through reducing the flow rate, is summarized in Figure 30 for the specified model parameters presented in Figure 29.

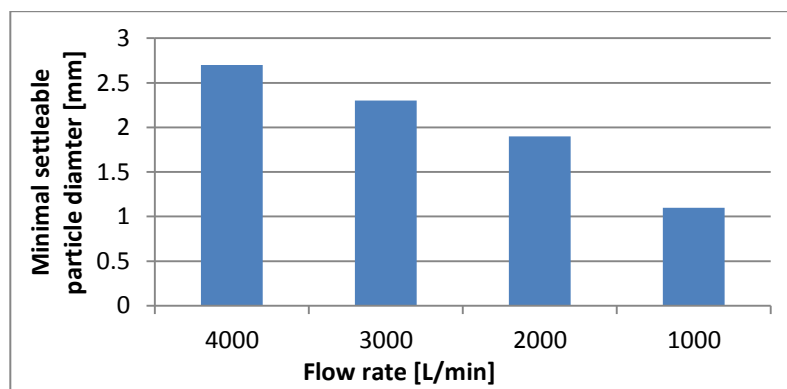
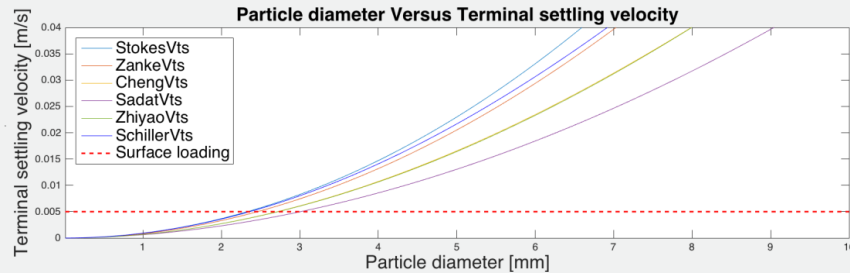


Figure 30: Decrease of settleable particle size due to flow rate reduction

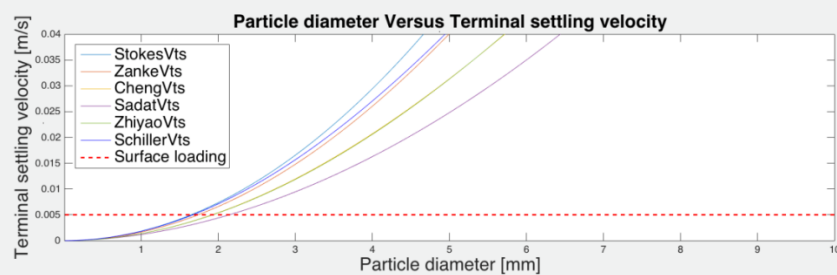
3.3.4. The effect of viscosity on settling

The viscosity fluctuations due to additional shear or temperature changes can influence settling efficiency. The sensitivity of viscosity changes has been studied in the ideal settling tank model. The effects of several viscosity values are shown in Figure 31.

For a fluid with apparent viscosity of $cP = 800$, flow rate of $Q = 3000$ l/min and a particle concentration of 10%



For a fluid with apparent viscosity of $cP = 400$, flow rate of $Q = 3000$ l/min and a particle concentration of 10%



For a fluid with apparent viscosity of $cP = 100$, flow rate of $Q = 3000$ l/min and a particle concentration of 10%

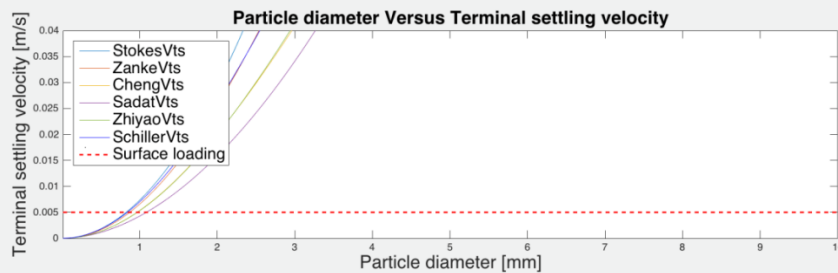


Figure 31: Increasing Terminal settling velocity with decreasing carrying fluid viscosity

The obtainable increase in settleable particles is presented in Figure 32 and points out that decreasing the viscosity significantly increases the settling efficiency.

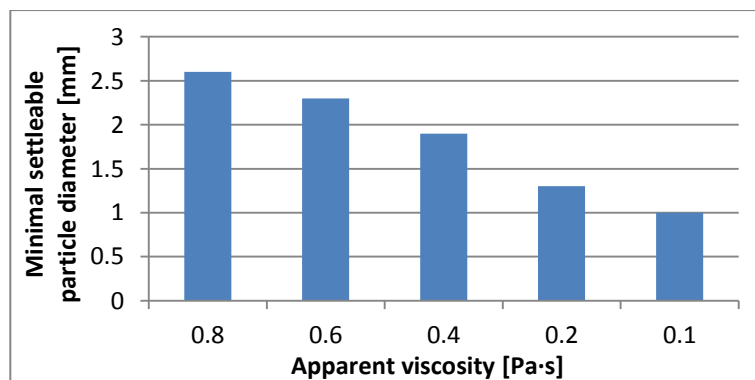


Figure 32: Increase in settleable particle sizes due to viscosity reduction

3.3.5. Others results

Laminar flow and settling conditions in the ideal settling tank are verified with the obtained Reynolds numbers for flow and particle settling. The Reynolds number obtained for flow fluctuated around 10-50, with peaks of 100 for high flow rates. The particle Reynolds numbers fluctuated around 0.01-5, with peaks of 50 for particles with high settling velocities. All obtained Reynolds numbers are within the laminar flow and settling conditions.

The obtained values for the Froude number indicated that the flow was unstable in all calculations except for an inflow rate of 4000 L/min. The unstable flow conditions are caused by the wide and high tank dimensions used in the calculations.

The critical scour velocity obtained from the calculations resulted in no bottom scour for all parameter combinations.

3.4. Chapter conclusion

The literature review covered in chapter 2 summarized multiple fluid and tank related effects, which influence the gravitational settling of particles. These effects are studied using Camp's ideal horizontal settling tank model and resulted in the following main conclusions:

- For a representative case, complete settling of particles between 2.5-3.5 mm and larger is achievable. This case includes a 20ft container sized tank, a common WBM with an apparent viscosity of 0.6 Pa·s and an inflow rate of 3000 L/min containing a particle concentration of 10%.
- Potential options which are identified to increase the settling efficiency are:
 - Optimizing settling tank design
 - Increasing settling tank size
 - Reducing the inflow rate
 - Reducing the WBDF viscosity
- When an optimistic case is considered, complete settling of particles between 0.6-0.8 mm and larger is achievable. This case includes a 20ft container sized tank, a WBM with a reduced apparent viscosity of 0.1 Pa·s and a reduced inflow rate of 1000 L/min containing a particle concentration of 10%.

The actual tank efficiency is expected to be lower than predicted by the calculations, since the ideal settling tank model makes use of a simplified approach with advantageous settling conditions.

The design of the settling tank can be optimized to create optimal settling conditions by maximizing the Froude number and minimizing the Reynolds number. To obtain lower Froude numbers, the tank has to be narrow and low in height. With respect to turbulence, the demand for a high Froude number conflicts with the demand for a small Reynolds number, which is associated with a wide settling tank.

Increasing the tank dimensions by a significant amount is a relevant solution to increase the settling efficiency. However, this is avoided since a larger tank makes handling and transportation of the settling tank difficult.

Managing the flow rate parameter is a promising option to increase the settling efficiency of the tank. The potential way to do this is by splitting the main flow into multiple settling tanks. Dividing the main flow of 3000 L/min over three settling tanks with 1000 L/min each, allows complete settlement of particles larger than 1.5-2 mm rather than the previous obtained 2.5-3.5 mm for 3000 L/min. This increase in efficiency is valid when three tanks of the same dimensions as in the MATLAB calculations are used.

Reducing the fluid viscosity is another promising option to increase the settling efficiency. This can be achieved by changing the drilling fluid composition or by making use of the shear thinning characteristics. When the apparent viscosity is reduced from 0.6 to 0.1 Pa·s, complete settlement of particle larger than 1.1-1.4 mm becomes achievable rather than the 2.5-3.5 mm for 600 Pa·s.

Combining the settling enhancements allows the settling of particles larger than 0.6-0.8 mm (1000 L/min, 0.1 Pa·s and 10% particle concentration). Since the ideal settling tank makes use of advantageous settling condition, achieving this settling efficiency will be challenging. Therefore, it can be concluded that the separation of the particles from a WBM in a settling tank is not sufficient enough to achieve the project objective. To increase the separation efficiency, the discussed enhancement options need to be considered or other separation techniques have to be considered to separate the remaining fine solids.

4. Experiments

This chapter of the report includes information regarding performed experiments. The preliminary calculations presented in chapter 3, indicated that the separation efficiency of the separation tank was not sufficient enough to meet the separation requirements. One of the suggested options to increase the separation efficiency is by reducing the drilling fluid viscosity through the introduction of vibrations and thereby increase the settling rate of particles. This chapter includes the vibrations experiments, which have been performed to quantify the obtainable viscosity reduction by introducing vibrations. In addition to the vibrational experiments, pressure filtration experiments are performed to get an indication of the applicability and separation efficiency, as a complementary separation technique.

4.1. Test samples and preparation

The water based drilling fluid used in the experiments is prepared in the laboratory by mixing raw materials with tap water. The selected components where: Cebo-gel Wyoming API bentonite, Xanthan gum and M6 Silverbond quartz flour (barite replacer). Additional information regarding these ingredients is attached in Appendix D.



Figure 33: Drilling mud materials from left to right: Quarts flour, bentonite and Xanthan gum

To compensate for the unavailability of barite, Sibelco M6 Silverbond quartz flour has been used, which has a comparable particle size distribution as barite. The amount of quartz flour is based on a volume comparison to barite, resulting in the same amount of suspended solids. The lower specific density of quartz flour is also advantageous, since it reduced the settling of solids during the experiments. For consistency, all experiments have been performed using the same drilling fluid composition.

4.1.1. Sample composition and characteristics

The water based drilling fluid composition is different for each drilled well, since the drilling fluid is engineered to have the required characteristics for the onsite situation. To obtain a realistic drilling fluid composition with field characteristics, different sources have been used. The overall composition is based on the compositions found in literature, which has been adjusted to match the drilling fluid characteristic of reference drilling logs attached in Appendix C. The final composition for the drilling fluid samples is shown in the figures below and referred to as clean mud:

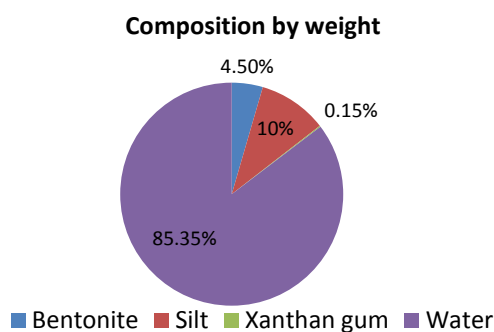


Figure 34: Sample composition by weight

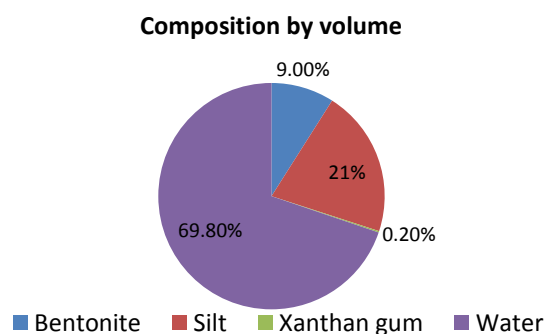


Figure 35: Sample composition by volume

Since quarts flour is used instead of barite, the composition by weight does not represent a drilling fluid used in practice. On the other hand, the composition by volume is comparable with a weighted water based drilling fluid.

The characteristics of the prepared drilling fluid are obtained by performing Fann viscometer measurements and plotting the consistency curve. Figure 36 shows the consistency curve of the prepared drilling fluid and the reference data obtained from the drilling logs.

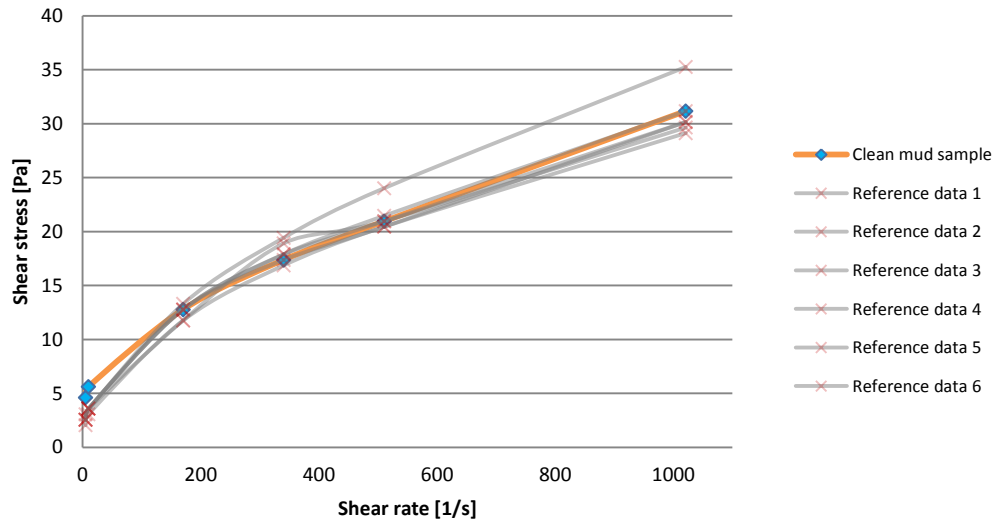


Figure 36: Consistency curve of clean mud sample versus reference

Figure 36 points out that the clean mud sample shows similar behaviour compared to the reference drilling fluids. To prevent the settling of the quarts flour particles during the experiments, stronger fluid characteristics are chosen for the low shear range of the clean mud samples. In Table 8 a comparison is presented of the yield point and plastic viscosity for the clean mud sample and the reference drilling fluids.

Table 8: Fluid characteristics of the clean mud sample versus reference data

	Yield point (YP)		Plastic viscosity (PV)	
Reference data	10-12	[Pa]	0.017-0.022	[Pa·s]
Clean mud sample	10	[Pa]	0.020	[Pa·s]

4.1.2. Sample preparation and storage

The clean mud samples have been prepared in batches of 1.5 litres using a high velocity blender attachment on top of a Kenwood major prime mixer. The materials have been added slowly to the water from the top of the blender in the following order: bentonite, xanthan gum and quarts flour. Mixing each batch for approximately 15 min resulted in a homogenous material without any bentonite lumps.

Each batch is prepared one day prior to the experiments and stored closed in a 15°C climate room. Cold storage was necessary to prevent degradation of the biological xanthan gum. Batches stored for several days in normal room conditions showed a large viscosity reduction and are therefore excluded from the experiments.

4.1.3. Replacement for the fine cuttings

The fine sized cuttings that are generated during drilling operations, are replicated by using fine sand. The associated material data sheet is attached in Appendix D. The sand is sieved to separate the particles into two size ranges 150-212 µm and 250-300 µm. These two batches are mixed with the WBM to study the effects of fine size cuttings during the experiments.

4.2. Test setup and test procedure

This section covers the three different test setups and the associated procedures used to perform the experiments. Two of the test setups are used for vibrations and one setup is used for filtration.

4.2.4. Vibration setups

Vibration related setups are used to understand the effects of vibrations on the drilling fluid viscosity. Based on the literature review it is known that vibrations reduce the viscosity of drilling fluids. The vibration experiments are aimed to get an indication of the viscosity reduction when vibrations are introduced to the water based drilling fluids. Multiple mud samples have been tested with different particle sizes and concentrations using vertical and horizontal vibrations.

The main equipment used for the vibration test setups include:

- Fann viscometer 35 SA (6 speed)
- A vertical vibration table
- Detla Physics Signalforce shaker
- Detla Physics Signalforce 100 Watt Amplifier
- Agilent 33522A waveform generator
- $\pm 5\text{mm}$ Linear variable differential transformer (LVDT)

4.2.4.1 The Fann Model 35 SA viscometer

The viscosity measurements during the experiments have been performed with a Fann Model 35SA direct indicating viscometer. These viscometers are commonly used by mud engineers and are recommended for evaluating the rheological properties of Newtonian and non-Newtonian fluids. The default configuration, which has been used during the experiments, includes a R1 Rotor Sleeve, B1 Bob, F1 Torsion Spring, and a stainless steel sample cup. This configuration is also recommended for field testing of water based drilling fluids by the American Petroleum Institute, API RP 13B-1/ISO 10414-1 Specification.

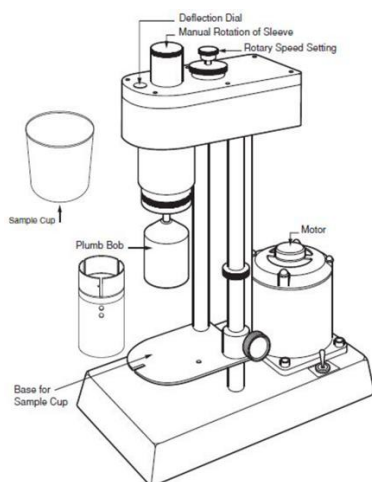


Figure 37: Fann Model 35SA viscometer

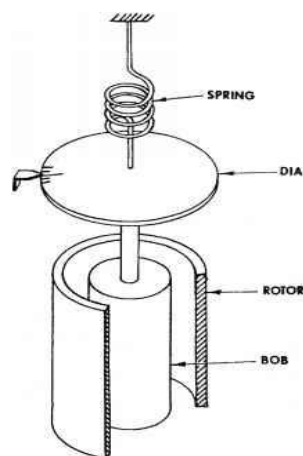


Figure 38: Schematic diagram of the direct indicating viscometer

The Fann viscometer measures the shear stress caused by a given shear rate. This is done by containing the test fluid in the shear gap (annular space) between the outer cylinder (rotor) and the inner cylinder (bob). The viscosity measurements are made by rotating the rotor at a known speed, which causes a viscous drag applied on the fluid. This drag creates torque on the bob, which results in a measurable deflection at the precision spring.

The shear gap between the rotor and bob in the standard configurations is limited to 1.17 mm. Using particles with a particle diameter close to this annular gap size can cause inaccurate measurements or damage the viscometer.

The accuracy of the Fann viscometer viscosity measurements is not specified in the manual. To account for this, an accuracy of $\pm 1^\circ$ deflection on the full scale is maintained. The chosen accuracy is comparable to the dead weight calibration accuracy ($\pm 0.5^\circ$) and fluid calibration accuracy (± 1.5) prescribed in the Fann manual.

4.2.4.2 Vertical vibration setup

The vertical vibration test setup is shown in Figure 39 and Figure 40. The setup consists of the Fann viscometer, vertical vibration table and a ± 5 mm LVDT connected to a computer.

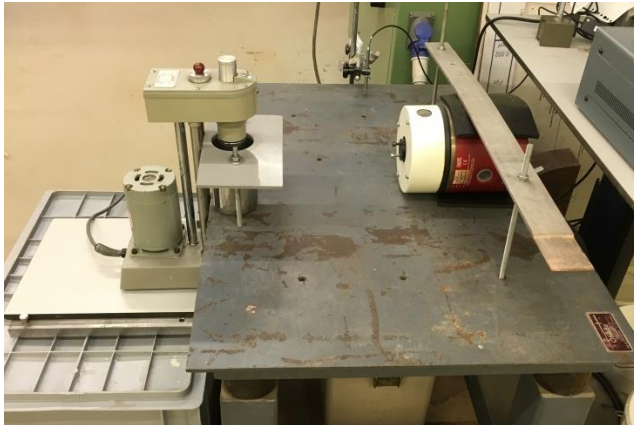


Figure 39: Vertical vibration test setup overview



Figure 40: Vertical vibration test setup

In this setup the default Fann fluid container is bolted to the vibrating table by using a PVC plate, as shown in Figure 40. This stiff connection allows the fluid container to follow the same vibrations as the vibrating table.

To prevent the Fann viscometer from vibrating during the experiments, a separate platform is used next to the vibrating table. To reduce the vibrations to a minimum, the Fann viscometer is placed on this platform ensuring a small gap between the Fann viscometer and the vibrating elements.

The height of the Fann viscometer is adjusted to meet the required space between the bob and bottom of the fluid container. According to the user manual this space has to be 1.27 mm or greater. During the experiments a gap of 3.7 cm is maintained.

The vertical vibrating table was able to create vibrations with a frequency of 50Hz and adjustable amplitude. The applied amplitudes and frequency are validated and continuously measured during the experiments using a ± 5 mm pre-calibrated LVDT connected to a computer. The sample rate of the LVDT was set to 2 kHz, which is 40 times higher than the vibrating frequency of the table. This resulted in 40 measurements points for each vibrational oscillation, allowing a distinction of the peak to peak table amplitude.

4.2.4.3 Horizontal vibration setup

The horizontal vibration test setup is shown in Figure 41 and Figure 42. The setup consists of the Fann viscometer, horizontal vibration element and a ± 5 mm LVDT connected to a computer. The power amplifier and wave form generator are not shown in the figures below.



Figure 41: Horizontal vibration test setup



Figure 42: Horizontal vibration test setup top view

In the horizontal vibration test setup, a Detla Physics Signalforce vibration element is used to create the horizontal vibrations. The frequency and amplitude of these vibrations could be varied by using a waveform generator and a power amplifier.

Similar to the vertical test setup, the Fann viscometer is placed on a separate platform to minimize the vibrations on the Fann viscometer. The height of the viscometer is also adjusted to match the same gap size between the bob and bottom of the fluid container of 3.7 cm.

The vibrations are carried from the vibration element to the fluid container by a stainless steel rod attached to the fluid container using a pipe bracket. To reduce the friction between the fluid container and table, oiled plastic foil is used.

4.2.4.4 Testing procedure of the vibration setups

The testing procedure for each sample included testing with the vertical and horizontal test setup. The procedure for testing one sample (approximately 340 ml) was done as follows:

1. Specific gravity determination of the sample
2. Shear the sample for 15 min at 600 RPM in the Fann viscometer
3. Perform Fann measurements with no vibrations in vertical setup
4. Perform Fann measurements with vertical vibrations (50 Hz, 0.4 mm, 2g acceleration)
5. Perform Fann measurements with vertical vibrations (50 Hz, 0.6 mm, 3g acceleration)
6. Perform Fann measurements with no vibrations in vertical setup
7. Specific gravity determination of the sample
8. Remixing of the sample
9. Specific gravity determination of the sample
10. Shear the sample for 15 min at 600 RPM in the Fann viscometer
11. Perform Fann measurements with no vibrations in horizontal setup
12. Perform Fann measurements with horizontal vibrations (50 Hz, 0.4 mm, 2g acceleration)
13. Perform Fann measurements with horizontal vibrations (50 Hz, 0.6 mm, 3g acceleration)
14. Perform Fann measurements with no vibrations in horizontal setup
15. Specific gravity determination of the sample

The Fann viscometer measurements have been performed according to the API Recommended Practice 13B-1 for field testing water based drilling fluids. This includes shearing the fluid between each measurement for 10s at 600 RPM. The Fann viscometer measurements have been performed at 3, 6, 100, 200, 300, 600 RPM.

The specific gravity of each test sample is determined before and after the Fann measurements using a 100 ml measuring cylinder. For the measurements, 100 ml of the 300 ml sample is used. The results of the specific gravity measurements are used to verify the fluid composition and as an indication if particles had been settling during the experiment, see section 4.3.7.5.

An analogue thermometer has been used to measure the fluid temperature during each set of Fann measurements. Since temperature influences the fluid viscosity, it was necessary to validate that no large temperature differences were present between each experiment.

4.2.5. Pressure filtration

The pressure filtration test setup has been used to investigate the possibilities of separating fine particles from water based drilling fluid using a pressure gradient. Based on literature it is known that bentonite suspensions have hole sealing properties, which makes them excellent support fluids in multiple drilling operations. The bentonite suspension forms a filter cake on the borehole wall to prevent inflow of formation fluids. By performing the pressure filtration experiments it is aimed to verify if pressure filtration is feasible for separating fine particles from the water based drilling fluid. Multiple mud samples with different particle sizes and filters with different sized opening have been used.

4.2.5.1 Pressure filtration test setup

In the drilling industry pressure filtration tests are performed using the API/Fann filter press setup. These tests are used to measure the filter cake performance created by the drilling fluid, which is specified as the fluid loss in drilling logs. A comparable setup to the API/Fann filter press has been used for the pressure filtration experiments. However instead of having a small fluid loss, it was aimed to have a large flow rate through the filter while fine solids remained on the filter. The used pressure filtration setup is shown in Figure 43 and Figure 44.

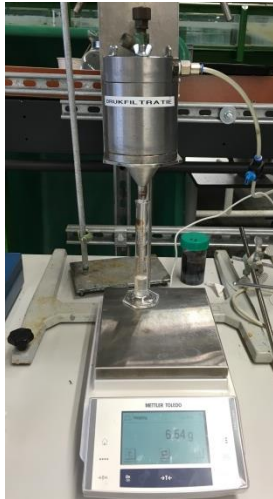


Figure 43: Pressure filtration setup

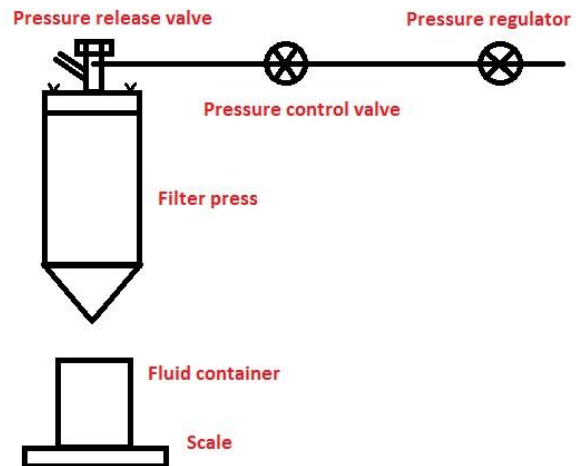


Figure 44: Pressure filtration setup schematic

The pressure filtration setup consists of a 70 mm diameter filter press located directly above a Mettler Toledo Excellence scale. The filtrate leaving the filter press during filtration is collected in a fluid container resting on the scale. A camera is used to capture the scale and the digital stopwatch readings, for determination of the flowrate through the filter medium. The setup was capable of performing pressure filtration test up to 10 bars. The pressure in the setup is regulated using a pressure regulator and a pressure control valve as shown in Figure 44.

The filters used in the experiments were:

- 1) Whatman grade 4 filter paper with openings of 20-25 μm
- 2) Steel wire mesh with openings of 63 μm
- 3) Nylon wire mesh with openings of 105 μm
- 4) Nylon wire mesh with openings of 250 μm

Modifications have been made to the steel and nylon filters to simplify the removal of the filters from the press without damaging the filter cake. Figure 45 shows the modified steel and nylon wire mesh filters used in the experiments.

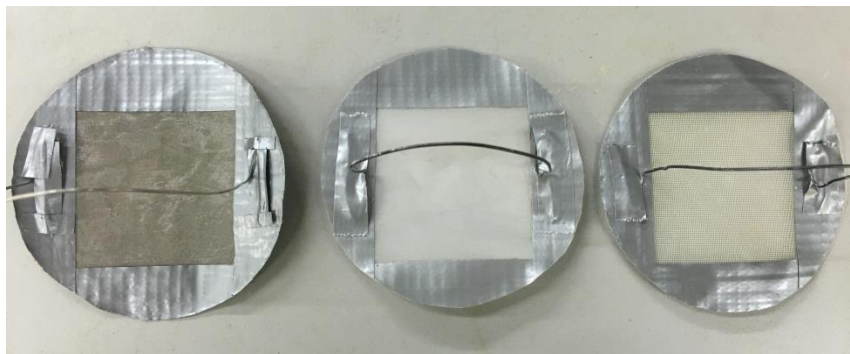


Figure 45: Modified steel and nylon wire mesh filters

4.2.5.2 Testing procedure pressure filtration

The testing procedure for each sample was as follows:

- Specific gravity determination of the batch drilling fluid
- Perform Fann measurements of the batch drilling fluid
- Perform pressure filtration experiment for samples of approximately 250 ml

The specific gravity determination and a standard Fann measurement are performed prior to the experiment to validate the drilling fluid characteristics. The pressure filtration experiment is performed in the following order: Adjust the pressure regulator to the required pressure, filling the filter press with drilling fluid, applying the redefined pressure in one go by opening the pressure control valve and simultaneously starting the stopwatch. The test is stopped if no fluid is left in the filter press or when the filter gets clogged.

4.2.6. Fann viscometer calibration

Prior to the experiments the Fann viscometer has been calibrated using the Fann 0.1 Pa·s calibration fluid and a prepared 90% glycerine solution in water. Both fluids are characterized as Newtonian fluids and have a linear relation between shear rate and shear stress. The calibration was difficult, since the viscosity of both fluids are sensitive to temperature fluctuations. The fluid temperature increased during calibration, resulting in lower viscosity measurements.

The calibration of the Fann viscometer has been performing prior and after the main experiments. The obtained results are presented in Table 9.

Table 9: Fann calibration results

	Fluid temperature [°C]	Fann viscometer readings						
		600 RPM	300 RPM	200 RPM	100 RPM	6 RPM	3 RPM	
Before – 0.1 Pa·s Calibration fluid	24.5	192	98	66	33	2	1	
Before – 0.2 Pa·s Glycerine solution	26.5	-	197	132	66	4	2	
After – 0.1 Pa·s Calibration fluid	27	184	93	62	32	2	1	
After – 0.2 Pa·s Glycerine solution	26.5	-	197	132	66	4	2	

The Fann calibration manual requires that the 300 RPM reading correspond to the calibration fluid viscosity within a ± 0.002 Pa·s margin, taking temperature dependent viscosity into account. The results from Table 9 verify that the Fann viscometer calibration is valid prior and after performing the main experiments.

4.3. Experiment results

This section presents the results obtained from the vibration and filter experiments.

4.3.7. Vibration results

4.3.7.1 Results of experiments with clean mud

Results from the Fann viscometer experiment with clean drilling fluid are shown in the consistency curves in Figure 46. The observable downwards shift of the lines indicate that vibrations influence the rheological properties of the clean drilling fluid. When the vibrations are interrupted and another measurement is performed, the consistency curve moves back to the starting conditions. This behaviour of the drilling fluid is related to the shear-thinning behaviour of the drilling fluids discussed in section 2.4.5.1.

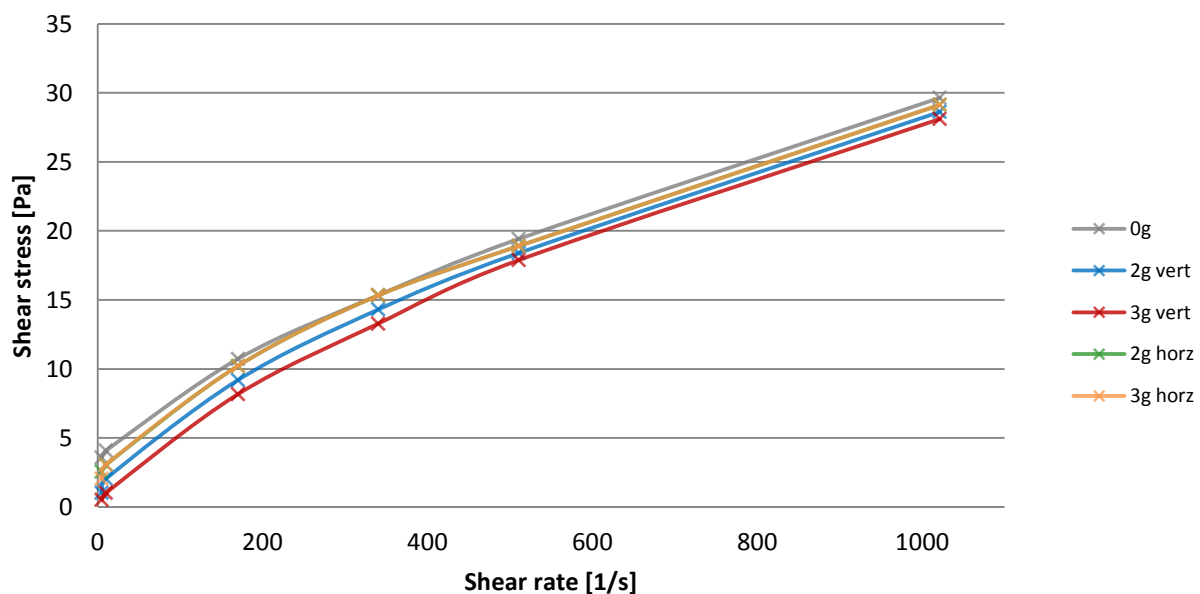


Figure 46: Results of clean drilling fluid – Consistency curves

The additional shear introduced by the vibrations does reduce the apparent viscosity of the drilling fluid. The apparent viscosity of the clean drilling fluid measurements is presented in Figure 47.

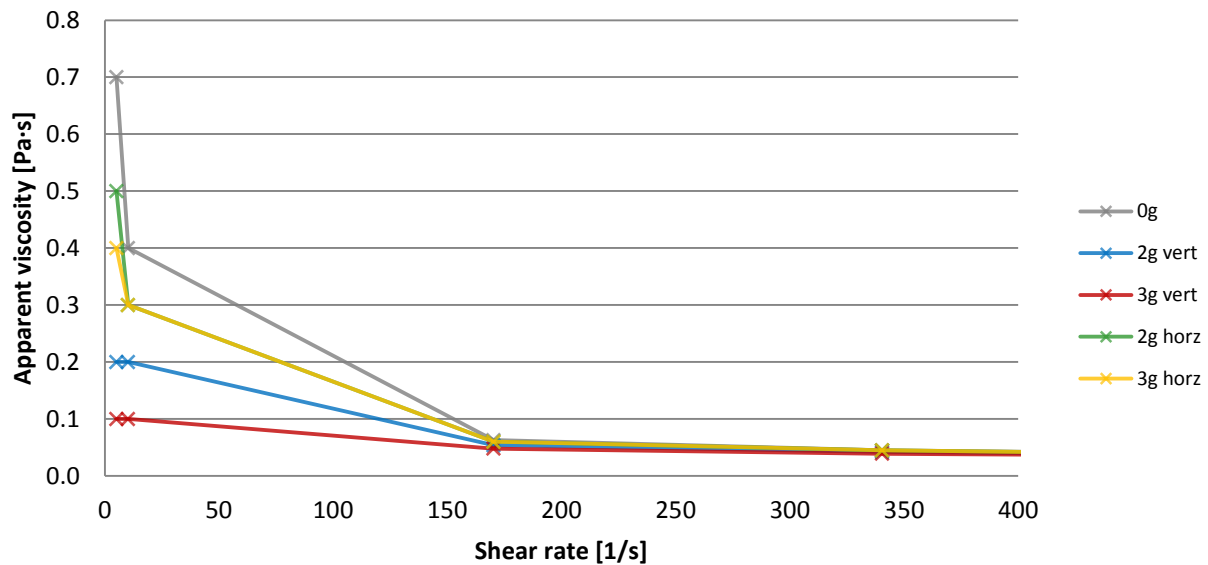


Figure 47: Clean drilling fluid results - Apparent viscosity

The results point out that the reduction of apparent viscosity is much greater at lower shear rates. This outcome could be related to the exponential shape of the consistency curve at low shear rates.

The steep exponential consistency curve at low shear rates indicates a strong shear thinning behaviour, which decreases with increasing shear rate. With increasing shear rate, the consistency curve flattens out and approaches a stable slope, which is defined as the plastic (Bingham) viscosity. The shear thinning behaviour of the drilling fluid in this high shear region is minimized and negligible, because the breakdown of the clay structures is larger than the build-up rate, as described in 2.4.5. Future increase of the shear rate by introducing vibrations, does not lead to significant viscosity reductions for the same reason.

The obtained reductions of apparent viscosity for clean drilling fluid are summarized in Table 10. The results point out that the viscosity reduction caused by vibrations indeed decrease in effectiveness with increasing Fann shear rates. Increasing the vibrations intensity from 2g to 3g acceleration shows a greater viscosity reduction. This result can be related to the relative greater additional shear introduced by the vibrations with higher acceleration. The vertical vibration setup also shows greater viscosity reductions than the horizontal vibration setup, this is further discussed in section 4.3.7.7.

Table 10: Clean drilling fluid results - Apparent viscosity reduction

Shear rate	No vibrations	2g vertical		3g vertical		2g horizontal		3g horizontal	
[1/s]	[Pa·s]	[Pa·s]	%	[Pa·s]	%	[Pa·s]	%	[Pa·s]	%
5	0.7	0.2	-71	0.1	-86	0.5	-29	0.4	-43
10	0.4	0.2	-50	0.1	-75	0.3	-25	0.3	-25
170	0.063	0.054	-14	0.048	-24	0.06	-5	0.06	-5
340	0.045	0.042	-7	0.039	-13	0.045	0	0.045	0
511	0.038	0.036	-5	0.035	-8	0.037	-3	0.037	-3
1021	0.029	0.028	-3	0.028	-5	0.029	-2	0.029	-2

The Fann viscometer measurements performed at low shear rates result in a small deflection on the dial. These low deflection readings have a relative small difference with the assumed accuracy of the Fann viscometer causing an uncertainty in the obtained reductions of viscosity. The steep exponential shape of the consistency curve in the low shear region increases this uncertainty. For higher shear rates, the uncertainty becomes smaller since the relative difference between the Fann viscometer dial readings becomes greater. By assuming the Fann viscometer accuracy defined in section 4.2.4.1, a fixed uncertainty for all performed Fann viscosity measurements can be described as presented in Table 11.

Table 11: Uncertainty of the Fann viscosity measurements

	Fann RPM and shear rate [1/s]					
	3 RPM 5 [1/s]	6 RPM 10 [1/s]	100 RPM 170 [1/s]	200 RPM 340 [1/s]	300 RPM 511 [1/s]	600 RPM 1021 [1/s]
Uncertainty	± 0.1 [Pa·s]	± 0.05 [Pa·s]	± 0.003 [Pa·s]	± 0.0015 [Pa·s]	± 0.001 [Pa·s]	± 0.0005 [Pa·s]

4.3.7.2 Particle size and concentration effects

To investigate the influence of small sized particles on the drilling fluid characteristics, samples with different particle sizes and particle concentrations are considered. The corresponding results are presented in this section.

By adding particles to the clean drilling fluid changes in rheology occur in the form of an increase in apparent viscosity. This increase is compared to the clean drilling fluid measurements in Table 12. The results point out that the addition of small particles lead to a greater viscosity increase in comparison to adding larger particles. The increase is greater in the high shear region.

Table 12: Apparent viscosity increase as a result of additional particles in clean drilling fluid

Shear rate	Clean mud	150-212 micron 9% vol. con.		150-212 micron 17% vol. con.		Clean mud	250-300 micron 9% vol. con.		250-300 micron 17% vol. con.	
[1/s]	[Pa·s]	[Pa·s]	[%]	[Pa·s]	[%]	[Pa·s]	[Pa·s]	[%]	[Pa·s]	[%]
5	0.8	0.9	+13	1	+25	0.9	1	+11	1.1	+22
10	0.5	0.55	+10	0.6	+20	0.55	0.55	0	0.65	+18
170	0.072	0.087	+21	0.108	+50	0.075	0.087	+16	0.108	+44
340	0.051	0.062	+21	0.0795	+56	0.051	0.059	+15	0.077	+50
511	0.042	0.051	+21	0.066	+57	0.041	0.047	+15	0.062	+51
1021	0.032	0.040	+25	0.052	+65	0.031	0.036	+18	0.047	+54

Comparable increases in viscosity could be predicted using the Krieger & Dougherty model described in section 2.4.3. Calculations performed with this model and particle volume concentrations of 9% and 17% lead to a viscosity increase of respectively 27% and 64%, which is comparable to the results listed above.

The Krieger & Dougherty model predicts the obtained apparent viscosity values good at high shear rates while giving an over estimation at low shear values. This suggests that the Krieger & Dougherty model is not accurate at low shear rates. Willenbacher N. and Georgieva K. (2013) verifies this suggestion by pointing out that the maximum packing fraction has different values at low and high shear rates. An increase of the shear rate causes particle to align in the flow direction resulting in a more efficient packing than the random close packed structure at low shear rates or at rest. The viscosity in the shear-thinning region is also influenced by the hydrodynamic interactions resulting in more shear with increasing particle surface area.

The apparent viscosity reductions obtained from measurements with suspended solids and vibrations are presented in Table 13 and Table 14 for respectively 150-212 particles and for 250-300 particles.

Table 13: Apparent viscosity reductions for drilling fluid with 150-212 micron suspended particle

Drilling fluid with 9% by volume 150-212 micron suspended particles										
Shear rate	No vibrations	2g vertical		3g vertical		No vibrations	2g horizontal		3g horizontal	
[1/s]	[Pa·s]	[Pa·s]	[%]	[Pa·s]	[%]	[Pa·s]	[Pa·s]	[%]	[Pa·s]	[%]
5	0.9	0.3	-67	0.2	-78	0.9	0.6	-33	0.4	-56
10	0.55	0.25	-55	0.15	-73	0.55	0.4	-27	0.3	-45
170	0.087	0.078	-10	0.066	-24	0.087	0.084	-3	0.081	-7
340	0.0615	0.0585	-5	0.054	-12	0.062	0.0615	0	0.0615	0
511	0.051	0.049	-4	0.047	-8	0.051	0.051	0	0.051	0
1021	0.0395	0.039	-1	0.0385	-3	0.040	0.0395	0	0.0395	0
Drilling fluid with 17% by volume 150-212 micron suspended particles										
5	1	0.3	-70	0.2	-80	1	0.7	-30	0.4	-60
10	0.6	0.25	-58	0.2	-67	0.6	0.45	-25	0.3	-50
170	0.108	0.090	-17	0.078	-28	0.111	0.108	-3	0.102	-8
340	0.0795	0.0735	-8	0.0675	-15	0.081	0.0795	-2	0.078	-4
511	0.066	0.064	-3	0.06	-9	0.068	0.067	-1	0.066	-3
1021	0.052	0.051	-2	0.05	-4	0.053	0.052	-2	0.0515	-3

Table 14: Apparent viscosity reductions for a drilling fluid with 250-300 micron suspended particle

Drilling fluid with 9% by volume 250-300 micron suspended particles										
Shear rate	No vibrations	2g vertical		3g vertical		No vibrations	2g horizontal		3g horizontal	
[1/s]	[Pa·s]	[Pa·s]	[%]	[Pa·s]	[%]	[Pa·s]	[Pa·s]	[%]	[Pa·s]	[%]
5	1	0.3	-70	0.2	-80	0.9	0.6	-33	0.5	-44
10	0.55	0.25	-55	0.15	-73	0.55	0.4	-27	0.3	-45
170	0.087	0.069	-21	0.060	-31	0.090	0.087	-3	0.081	-10
340	0.0585	0.054	-8	0.0495	-15	0.060	0.0585	-3	0.057	-5
511	0.047	0.045	-4	0.043	-9	0.049	0.049	0	0.047	-4
1021	0.036	0.035	-3	0.034	-6	0.037	0.0365	-1	0.036	-3
Drilling fluid with 17% by volume 250-300 micron suspended particles										
5	1.1	0.3	-73	0.2	-82	1.1	0.7	-36	0.6	-45
10	0.65	0.25	-62	0.15	-77	0.65	0.45	-31	0.4	-38
170	0.108	0.087	-19	0.069	-36	0.114	0.108	-5	0.102	-11
340	0.0765	0.071	-8	0.0585	-24	0.081	0.078	-4	0.075	-7
511	0.062	0.059	-5	0.051	-18	0.066	0.065	-2	0.065	-2
1021	0.047	0.046	-2	0.042	-11	0.051	0.049	-4	0.0485	-5

Fann measurements performed for the drilling fluid samples with suspended particles show similar results to those obtained from the experiments on clean drilling fluid. The obtained apparent viscosity reductions are also comparable, but take place at higher viscosity values. The additional shear created by the vibrations is most effective in the low shear region, where strong shear-thinning behaviour is present.

The low shear rates in the settling tank can be assumed to be comparable with the low shear region of the Fann viscometer. The obtained viscosity reductions at the low shear region of the Fann viscometer are therefore interesting for this study and are shown in Figure 48 for shear rates of 5 (3 RPM) and 10 (6 RPM).

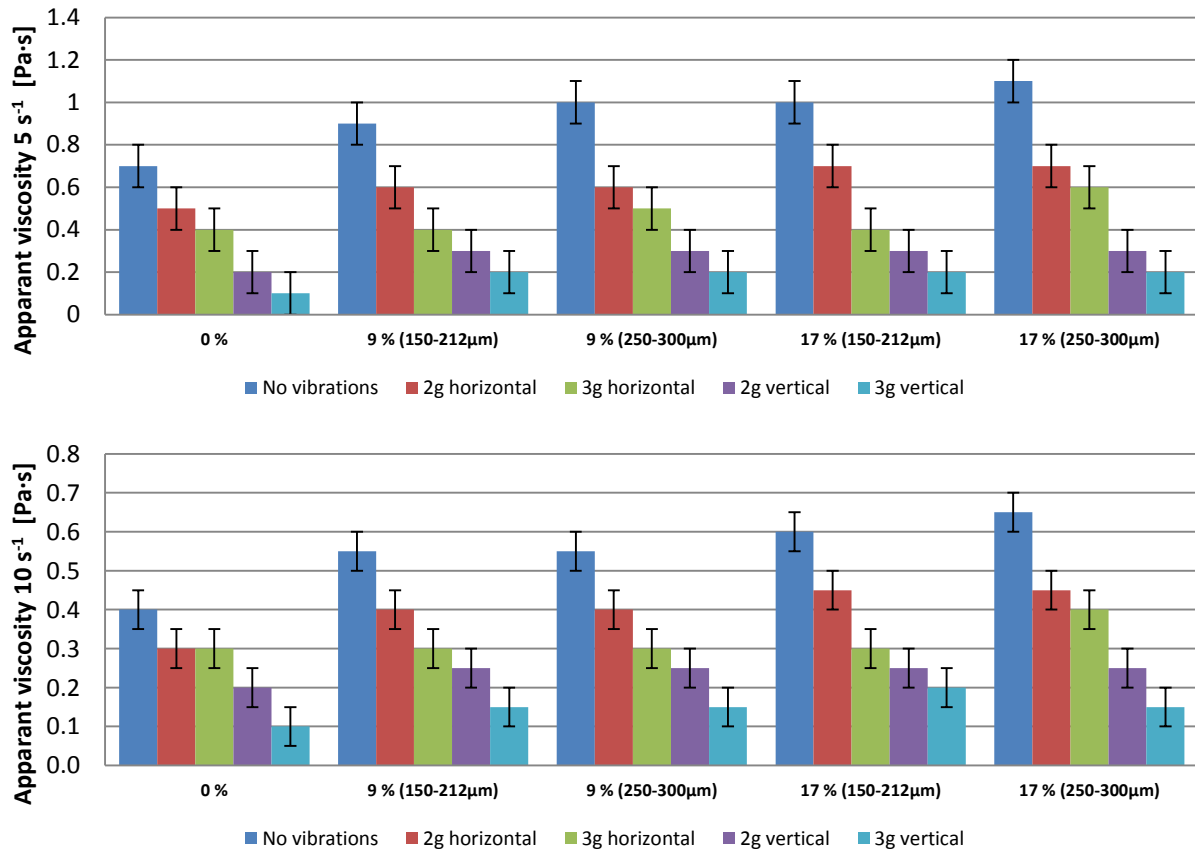


Figure 48: viscosity reductions at 3 RPM above and 6 RPM below

4.3.7.3 Amplitude and frequency tests

Multiple experiments have been performed to understand the influence of vibration frequency and amplitude on the drilling fluid viscosity. Vibrations with accelerations of 3g and 5g have been created using two different combinations of frequency and amplitude. Due to the setup limitations, only given frequency and amplitude combinations were possible. The obtained apparent viscosity reductions for experiments with accelerations of 3g and 5g are presented in Table 15.

Table 15: Apparent viscosity reduction of a clean drilling fluid for different frequencies and amplitudes

Shear rate	No vibrations	3g 50 Hz/0.6 mm		3g 100 Hz/0.15 mm		No vibrations	5g 50 Hz/1 mm		5g 100 Hz/0.25 mm	
[1/s]	[Pa·s]	[Pa·s]	[%]	[Pa·s]	[%]	[Pa·s]	[Pa·s]	[%]	[Pa·s]	[%]
5	0.8	0.5	-38	0.6	-25	0.8	0.4	-50	0.5	-38
10	0.5	0.350	-30	0.4	-20	0.5	0.3	-40	0.350	-30
170	0.075	0.072	-4	0.072	-4	0.075	0.072	-4	0.069	-8
340	0.0525	0.051	-3	0.051	-3	0.0525	0.0525	0	0.051	-3
511	0.044	0.043	-2	0.043	-2	0.044	0.044	0	0.042	-5
1021	0.032	0.032	0	0.032	0	0.032	0.0325	+2	0.0315	-2

The results in Table 15 indicate that vibrations with a lower frequency and a larger amplitude lead to a greater viscosity reduction than obtainable by vibrations with the same acceleration but with a higher frequency and lower amplitude. The differences between the results are however small and have the same magnitude as the assumed Fann measurement uncertainty. A trend can be noticed in the results, however, it is difficult to confirm this trend since the uncertainty is high.

As mentioned in section 2.5, Deshpande & Barigou (2001) studied the vibrational flow of non-Newtonian fluids in pipes. They performed a similar study where the flow enhancement effect of a shear-thinning fluid is determined, while being subjected to vibrations with different amplitude and frequencies corresponding to the same acceleration. Their results also showed almost identical enhancement ratios for different combinations of frequencies and amplitude. They assumed that the results were practically identical and concluded that different amplitude and frequencies corresponding to the same acceleration resulting in the same enhancement effect.

Additional experiments have been performed to understand the effectiveness of increasing the vibration frequency. During these experiments, the amplitude is kept at 0.15 mm while the frequency is increased from 10 to 100 Hz in steps of 10 Hz. The obtained results are presented in Table 16. The results indicate that a vibration with a small intensity is sufficient to create a viscosity reduction in the low shear region. The results also indicate that the effectiveness of the vibrations decrease with increasing intensity.

Table 16: Apparent viscosity reduction of a clean drilling fluid for increasing frequency and fixed amplitude of 0.15 mm

Shear rate	10 Hz (0.03g)	20 Hz (0.12g)	30 Hz (0.27g)	40 Hz (0.48g)	50 Hz (0.75g)	60 Hz (1.09g)	70 Hz (1.48g)	80 Hz (1.93g)	90 Hz (2.45g)	100 Hz (3.02g)
[1/s]	[%]	[%]	[%]	[%]	[%]	[%]	[%]	[%]	[%]	[%]
5	0	0	0	-13	-25	-25	-38	-38	-38	-50
10	0	0	-10	-20	-20	-20	-30	-30	-30	-40
170	0	0	0	0	0	-4	-4	-8	-8	-12
340	0	0	0	0	0	0	0	-3	-3	-6
511	0	0	0	0	0	0	0	-2	-2	-7
1021	0	0	0	0	0	+2	0	0	0	-2

4.3.7.4 Gel strength development during experiments

Gel strength measurements have been performed with Fann viscometer during the vibrational experiments. To reduce the duration of each experiment and prevent the test setups/samples from exposure to long lasting vibrations, it is decided to perform only the 10 sec gel strength measurement. The obtained Fann deflections readings for the standard API gel strength test at a shear rate of 5 [1/s] and the 10 sec gel strength are presented in Table 17. The results indicate that the vibrations prevent the build-up of the gel strength for the drilling fluid samples with the large suspended particles.

The gel strength is in generally measured as a peak deflection on the Fann viscometer dial after turning the viscometer on at the lowest shear rate of 5 [1/s]. The measured peak deflection gives an indication of the required shear to reach the breaking point of the formed gel structure. However, the observation of this peak deflection was absent in several measurements as the dial deflection did not bypass the standard test deflection obtained at a shear rate of 5 [1/s]. For these situations, it can be concluded that the additional shear created by the vibrations is large enough to prevent the build-up of gel strength in the first 10 seconds

of drilling fluid being at rest. Extra measurements at 10 min and 30 min gel strength are required to verify if the gel strength is absent for longer time periods of rest.

Table 17: Fann deflection readings for 3 RPM and 10 sec gel strength

Particle concentration	Fann deflection readings [°]									
	No vibrations		2g vertical		3g vertical		2g horizontal		3g horizontal	
	3 RPM	10 sec gel	3 RPM	10 sec gel	3 RPM	10 sec gel	3 RPM	10 sec gel	3 RPM	10 sec gel
0 %	7	8	2	3	1	2	5	6	4	5
9 % (150-212µm)	9	11	3	4	2	3	6	7	4	5
9 % (250-300µm)	9	11	3	3	2	2	6	6	5	5
17 % (150-212µm)	10	12	3	3	2	2	7	8	4	5
17 % (250-300µm)	11	13	3	3	2	2	7	7	6	6

The other measurements performed with vibrations show a smaller deflection difference between the gel strength deflection and the standard test deflection at 3 RPM. The smaller difference indicates a slower gel strength build-up for the samples exposed to vibrations.

A significant uncertainty is present in the gel strength measurements since the deflection differences are of the same size as the assumed Fann viscometer accuracy of 1°.

4.3.7.5 Verification of no settling during experiments

The settling of particles during the Fann viscometer experiments is unwanted since it causes rheology changes during the experiments. To verify that no settling has taken place and the fluid rheology is persistent during the experiments, the specific gravity and viscosity has been measured before and after the experiments. Table 18 presents the relative viscosity differences between the performed measurements for each set of experiments.

Table 18: The relative viscosity differences between the control measurements performed for each set of experiments

Shear rate	150-212 micron particles				250-300 micron particles			
	Vertical 9%	Horizontal 9%	Vertical 17%	Horizontal 17%	Vertical 9%	Horizontal 9%	Vertical 17%	Horizontal 17%
[1/s]	[%]	[%]	[%]	[%]	[%]	[%]	[%]	[%]
5	0	0	0	0	0	0	0	0
10	0	0	0	+8	0	0	0	0
170	0	0	0	0	-7	-3	-6	-5
340	0	+2	0	+2	-5	-3	-6	-6
511	0	+2	+2	+1	-2	0	-7	0
1021	0	0	+1	-1	-4	-1	-4	-3

The control measurements indicate that the measurement differences are relatively small suggesting a limited rheology change during the experiments. The experiments performed with the 250-300 micron particles clearly show a small viscosity loss, which is related to particle settling. This can be confirmed by comparing the specific gravity measurement, presented in Table 19.

Table 19: The specific gravity measurements performed for each set of experiments

Particle concentration	Vertical experiments			Horizontal experiments		
	SG before	SG after	Difference [%]	SG before	SG after	Difference [%]
9 % (150-212µm)	1.23	1.21	-2	1.23	1.20	-2
9 % (250-300µm)	1.22	1.13	-7	1.22	1.14	-7
17 % (150-212µm)	1.34	1.30	-3	1.34	1.29	-4
17 % (250-300µm)	1.33	1.25	-6	1.34	1.25	-7

The specific gravity measurements show that settling of particles occurred during the Fann measurements. The settling effects are greater for the drilling fluid suspensions with large particles. This is as expected since particles with larger diameters settle much quicker than smaller particles.

The rheology changes due to the settling of the particles are relatively small and can be assumed negligible when the Fann measurement uncertainty is considered.

4.3.7.6 Verification of shear thinning

Complementary vibrational experiments are performed to verify that the previous presented results are indeed related to the shear-thinning behaviour of the drilling fluids. As the obtained results could also be related to additional shear created by the vibrations in the annular space between the bob and rotor. This would influence the Fann viscometer measurement method and thereby make the results invalid.

The verification experiments are performed with the previously used 0.1 Pa·s Fann calibration fluid and the 10% glycerol solution. The experiments are done according to the same testing procedure as the drilling fluid samples. Since both verification fluids have Newtonian properties, viscosity reductions due to shear-thinning were excluded from the experiments. To verify that the Fann viscometer was not influenced by the vibrations, no change in viscosity had to be proven at the fixed Fann measurement points (shear rates). Since Newtonian fluids have a constant viscosity, the apparent viscosity calculation should give the same viscosity for each measurement point. If the vibrations create additional shear on the bob, the experiments with vibrations should give higher viscosity measurements than the experiments without vibrations, since a higher shear stress will be measured for the same Fann rotation speed (shear rate).

The processed results of the experiments are presented in Figure 49 for the 0.1 Pa·s Fann calibration fluid and in Figure 50 for the 10% glycerol solution. The obtained consistency curves were linear and therefore confirm that both verification fluids are Newtonian fluids.

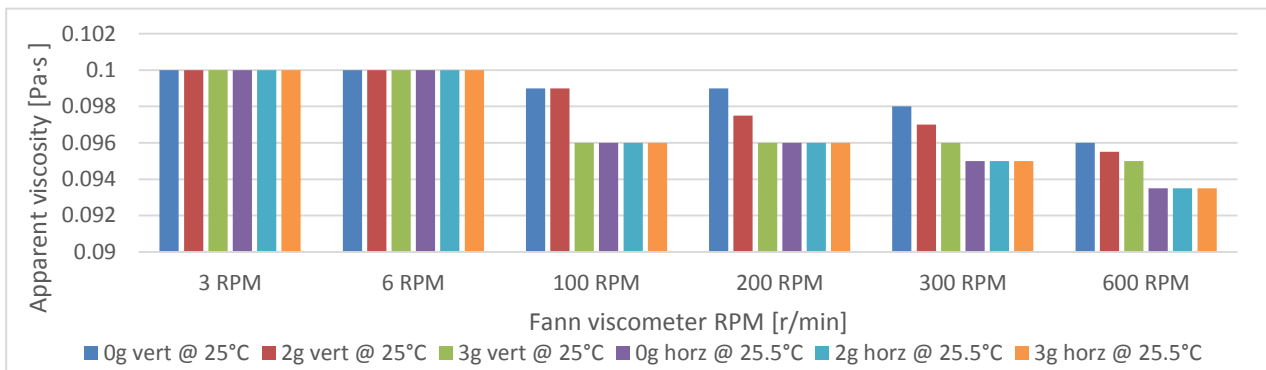


Figure 49: 0.1 Pa·s calibration fluid - Apparent viscosity comparison

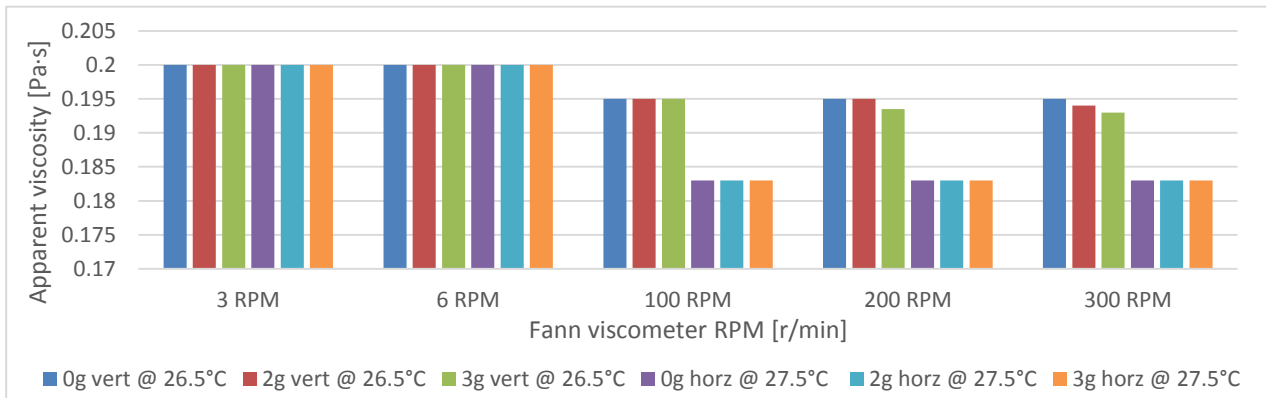


Figure 50: 10% glycerol solution - Apparent viscosity comparison

The results obtained from the verification experiments point out that there is no or a negligible small viscosity difference between the experiments performed with and without vibrations. This indicates that additional shear created by the vibrations does not influence the Fann measurements for both horizontal and vertical vibrations.

However, the results also show significant viscosity reductions at high shear rates compared to the measured viscosities at the low shear rates. This finding could be related to a reduced shear rate in the annular space between the bob and rotor due to the flow disturbance caused by the vibrations. This is however unlikely, since the experiments without vibrations also show the same viscosity reduction. Therefore, a more realistic explanation would be the influence of temperature on the verification fluids.

Similar to many other viscous fluids, the viscosity of the verification fluids are sensitive to temperature changes, especially the 10% glycerol solution. The viscosity of glycerol for example, can vary drastically with relative small temperature fluctuations. Figure 51 shows the consistency curves of glycerol at various temperatures, the slope of the linear consistency curves represents the dynamic viscosity of the Newtonian fluid. As the figure points out, the viscosity of glycerol can decrease significantly for relative small temperature rises.

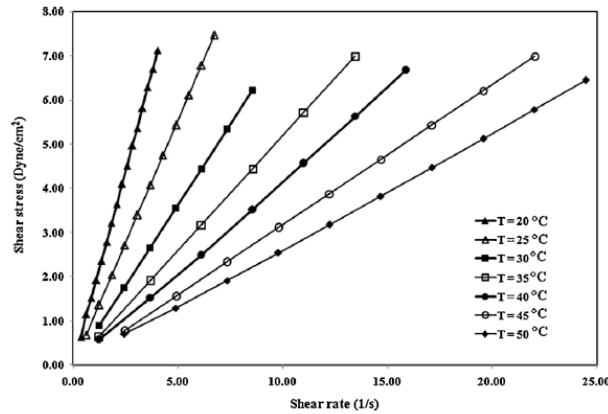


Figure 51: Consistency curves of glycerol at various temperatures [48]

Since the shear created by the Fann apparatus increases the fluid temperature, a viscosity reduction at high shear rates becomes supportable. The temperature increase can be local between the bob and rotor or global increasing the temperature of the sample. A significant global temperature increase was measured for the 10% glycerol solution. Since the glycerol solution has a higher viscosity, the shear forces becomes greater resulting in a faster temperature increase compared to the 0.1 Pa·s Fann calibration fluid.

4.3.7.7 Difference between vertical and horizontal vibrations

The vibrational experiments performed with drilling fluid which are presented in the various paragraphs of this chapter, included a difference in the achievable viscosity reduction between the horizontal and vertical vibrations. The measurements obtained from the vertical vibrations resulted in a greater viscosity reduction compared to the horizontal vibration results. Since the verification experiments showed that that additional shear created by the vibrations had no significant influence on the Fann viscometer measurement method, therefore another explanation was necessary to clarify these differences. A clarification of the differences can be found in the thixotropic shear history dependent behaviour of the drilling fluid and the different exposure methods of the vibrations on the drilling fluid.

Drilling fluids are known to exhibit a noticeable thixotropic behaviour, which is time and shear history dependent. Tehrani (2008) performed various experiments to describe this thixotropic behaviour with equations. During his experiments, the test samples have been exposed to multiple cycles of increasing and decreasing shear rates. The results obtained from the experiments showed clear hysteresis loops in the consistency curves. Figure 52 shows the hysteresis loop that were obtained and the shear rate step change graph.

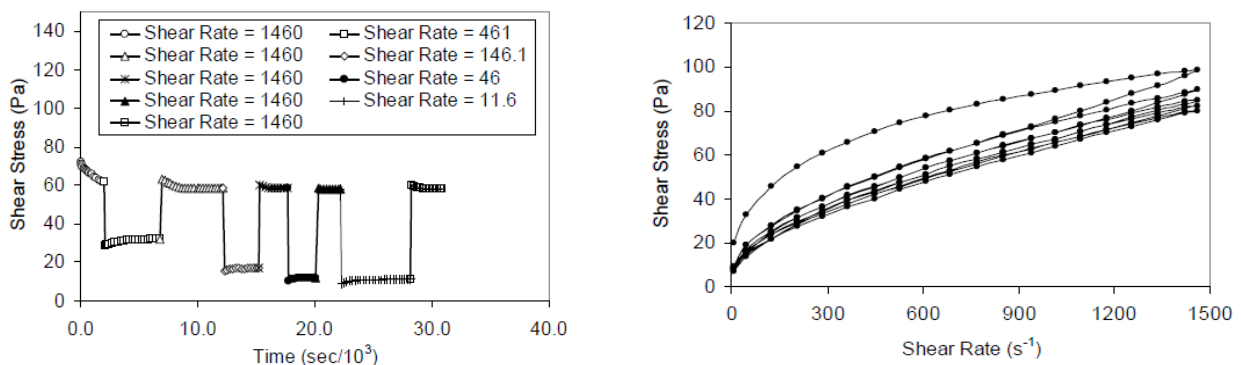


Figure 52: Drilling fluid thixotropic behaviour – hysteresis loop [51]

Since each set of vibrational experiments carried out in this thesis, is executed after each other using the same drilling fluid batch, a hysteresis loop might have been influencing the experiment results. This could explain the observed differences between the experiments, because in each set the vertical experiments were performed before the horizontal experiments. The drilling fluid used in the horizontal experiments is therefore more sheared compared to the drilling fluid used in the vertical experiments. As shown in Figure 52, the effects of the hysteresis loop are still present after multiple shearing cycles.

The influence of the hysteresis loop on the shear-thinning behaviour in the low shear region is also interesting. The shear cycles reduce the shear-thinning properties of the drilling fluid, as the consistency curve becomes more linear after each shearing cycle. Since the shear-thinning properties of the drilling fluid decreases, the influence of the vibrations on the viscosity also decreases.

Another explanation for the differences in the achievable viscosity reduction between the horizontal and vertical vibrations can be related to the exposure method of the vibrations on the drilling fluid. The intensity of the horizontal and vertical vibrations was measured with the LVDT near the source of the vibrations, which represented the vibration intensity of the Fann fluid container cup. However, these vibrations are carried over differently to the drilling fluid sample due to the shape of the fluid container and vibration direction.

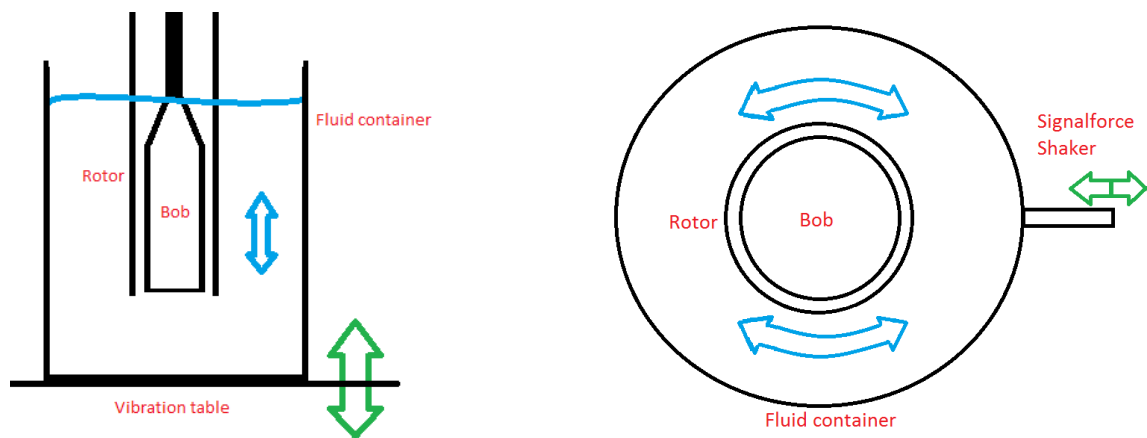


Figure 53: Fluid motion – side view of vertical and top view of horizontal vibration setups

During the vertical vibration experiments, the fluid is vibrated vertically creating a homogeneous fluid motion, while in the horizontal setup the fluid motion is occurring around the round boundaries of the fluid container and the Fann rotor. Figure 53 presents the fluid motion in the vertical and horizontal test setups. The differences in fluid motion can result in different shear stresses and therefore cause different viscosity reductions.

The tangential fluid flow in the annular space between the rotor and bob of the viscometer can be described analytically using the equations of continuity and motion in cylindrical coordinates (r, θ, z) . The equations given by Bird et al. (2007) are considered to evaluate the problem for a typical Couette viscometer without the influence of vibrations and a Newtonian fluid with constant density and viscosity.

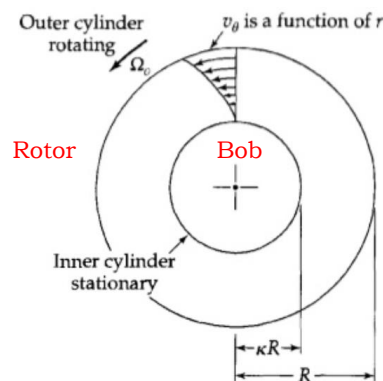


Figure 54: Top view of the annular shear space between the rotor and bob [10]

The equation of continuity for cylindrical coordinates is defined as [10]:

$$\frac{\partial \rho_f}{\partial t} + \frac{1}{r} \frac{\partial(\rho_f r v_r)}{\partial r} + \frac{1}{r} \frac{\partial(\rho_f v_\theta)}{\partial \theta} + \frac{\partial(\rho_f v_z)}{\partial z} = 0 \quad (48)$$

Where: ρ_f = fluid density [kg/m³] and v = fluid velocity [m/s]

When the end effects near the top and bottom of the shear gap are neglected, the fluid flow can be assumed to be occurring mainly in the angular direction and depending on the radial coordinate (r), see Figure 54. With this assumption the radial (v_r) and axial (v_z) components of the velocity vector become negligible $v_r = 0$, $v_z = 0$ and $v_\theta = v_\theta(r)$. In addition, the fluid density is assumed to be constant and the pressure (p) is assumed to be dependent on z because of gravity and on r because of the centrifugal force. With these assumptions, the equation of continuity can be reduced to:

$$\frac{\rho_f}{r} \frac{\partial(v_\theta)}{\partial \theta} = 0 \quad (49)$$

Using the same assumptions, the equations of motion given by Bird et al. (2007) can be simplified.

The complete equations of motion are defined in cylindrical coordinates (r, θ, z) as [10]:

r – component:

$$\rho_f \left(\frac{\partial v_r}{\partial t} + v_r \frac{\partial v_r}{\partial r} + \frac{v_\theta}{r} \frac{\partial v_r}{\partial \theta} + v_z \frac{\partial v_r}{\partial z} - \frac{v_\theta^2}{r} \right) = - \frac{\partial p(r, z)}{\partial r} + \rho_f g_r + \mu \left[\frac{\partial}{\partial r} \left(\frac{1}{r} \frac{\partial(r v_r)}{\partial r} \right) + \frac{1}{r^2} \frac{\partial^2 v_r}{\partial \theta^2} + \frac{\partial^2 v_r}{\partial z^2} - \frac{2}{r^2} \frac{\partial v_\theta}{\partial \theta} \right] \quad (50)$$

θ – component:

$$\rho_f \left(\frac{\partial v_\theta}{\partial t} + v_r \frac{\partial v_\theta}{\partial r} + \frac{v_\theta}{r} \frac{\partial v_\theta}{\partial \theta} + v_z \frac{\partial v_\theta}{\partial z} + \frac{v_r v_\theta}{r} \right) = - \frac{1}{r} \frac{\partial p(r, z)}{\partial \theta} + \rho_f g_\theta + \mu \left[\frac{\partial}{\partial r} \left(\frac{1}{r} \frac{\partial(r v_\theta)}{\partial r} \right) + \frac{1}{r^2} \frac{\partial^2 v_\theta}{\partial \theta^2} + \frac{\partial^2 v_\theta}{\partial z^2} - \frac{2}{r^2} \frac{\partial v_r}{\partial \theta} \right] \quad (51)$$

z – component:

$$\rho_f \left(\frac{\partial v_z}{\partial t} + v_r \frac{\partial v_z}{\partial r} + \frac{v_\theta}{r} \frac{\partial v_z}{\partial \theta} + v_z \frac{\partial v_z}{\partial z} \right) = - \frac{\partial p(r, z)}{\partial z} + \rho_f g_z + \mu \left[\frac{1}{r} \frac{\partial}{\partial r} \left(r \frac{\partial(v_z)}{\partial r} \right) + \frac{1}{r^2} \frac{\partial^2 v_z}{\partial \theta^2} + \frac{\partial^2 v_z}{\partial z^2} \right] \quad (52)$$

The equations of motion in reduced form:

r – component:

$$\frac{\rho_f v_\theta^2}{r} = \frac{\partial p(r, z)}{\partial r} \quad (53)$$

θ – component:

$$\mu \left(\frac{\partial}{\partial r} \left(\frac{1}{r} \frac{\partial(r v_\theta)}{\partial r} \right) \right) = 0 \quad (54)$$

z – component:

$$\frac{\partial p(r, z)}{\partial z} - \rho_f g_z = 0 \quad (55)$$

In the reduced equations, the r – component describes the effects of the centrifugal force on the pressure and the z – component describes the effect of gravity on the pressure (hydrostatic pressure). The θ – component gives the velocity distribution, which can be solved for applying boundary conditions. The used boundary conditions are based on the assumption that the fluid does not slip at the surface of both cylinders.

Boundary conditions:

$$\text{Inner cylinder:} \quad \text{At } r = \kappa R \quad v_\theta = 0 \quad (56)$$

$$\text{Outer cylinder:} \quad \text{At } r = R \quad v_\theta = \Omega R \quad (57)$$

Where: Ω = the angular velocity of the outer cylinder [rad/s], R = the distance of the cylinder to the rotation centre [m] and κ = geometrical factor (see Figure 54) [-].

Solving the θ – component using the boundary conditions gives the velocity distribution:

$$v_{\theta}(r) = \Omega R \left(\frac{\frac{r}{\kappa R} - \frac{\kappa R}{r}}{\frac{1}{\kappa} - \kappa} \right) \quad (58)$$

From the velocity distribution the momentum flux can be defined as [10]:

$$\tau_{r\theta} = -\mu \frac{d}{dr} \left(\frac{v_{\theta}}{r} \right) = -2\mu\Omega \left(\frac{R}{r} \right)^2 \left(\frac{\kappa^2}{1 - \kappa^2} \right) \quad (59)$$

The torque created by the fluid acting on the inner cylinder is given as the product of the total force acting on the surface of the inner cylinder and the lever arm. For the assumed Newtonian fluid this results in:

$$T_z = (-\tau_{r\theta})|_{r=\kappa R} (2\pi\kappa RL)(\kappa R) = 4\pi\mu\Omega R^2 L \left(\frac{\kappa^2}{1 - \kappa^2} \right) \quad (60)$$

Where: L = the height of the cylinder [m]

When the same set of equations is solved for a power-law fluid the equation becomes:

$$T_z = 2\pi K \Omega (\kappa R)^2 L \left(\frac{\frac{2}{n}}{1 - \kappa^{\frac{2}{n}}} \right) \quad (61)$$

Where: K = flow consistency [Pa·s], n = flow behaviour index [-]

And for a Bingham fluid the equation becomes:

$$T_z = 4\pi\mu_{pl}^B \Omega R^2 L \left(\frac{\kappa^2}{1 - \kappa^2} \right) - \frac{\tau_0^b}{\mu_{pl}^B} \ln \kappa \quad (62)$$

Where: τ_0^b = Bingham yield point [Pa], μ_{pl}^B = Bingham plastic viscosity [Pa·s]

The power-law and Bingham equations convert to the Newtonian solution when Newtonian parameters are considered, $n = 1$ and $\tau_0^b = 0$.

By using the equations (60)-(62), the viscosity of a fluid can be approached in a Couette viscometer such as the Fann 35 SA. The viscosity or viscosity model parameters can be solved from the equations for a measured torque value and a known angular velocity of the outer cylinder. However, since the end effects are neglected, the obtained viscosity will include an uncertainty.

When vibrations are included, the assumptions made in this approach become very inaccurate since the fluid motion in vertical (z) and rectangular direction (r) cannot be neglected. This results in a complex set of equations that have to be solved. However, based on the verification experiments performed in section 4.3.7.6, it can be assumed that the fluid motion in the z and r directions have a negligible influence when a Newtonian fluid is considered. This however changes when a non-Newtonian fluid is considered. The additional fluid motion created by the vibrations leads to a greater fluid velocity vector and causes the velocity distribution in the shear gap to change, because the terms v_r and v_z become non-zero. The greater velocity vector causes higher shear rates in the fluid, reducing the drilling fluid viscosity due to shear-thinning effects. The additional shear created by the vertical and rectangular velocity also effects the gel strength build-up, as presented in the experiment results in section 4.3.7.4.

When the vertical and horizontal vibration setups are compared, it can be assumed that the vibrations in the vertical setup will result in a greater vertical velocity component v_z , since the vibrations are in the same direction as the position of the shear gap, see Figure 54. The vibrations created in the horizontal setup on the other hand are perpendicular to the shear gap and are screened off from the gap by the rotor. The vibrations are therefore less effective in creating a vertical velocity component in the shear gap, resulting in a smaller velocity vector, less additional shear and finally a smaller viscosity reduction. This phenomenon is expected to be the main cause leading to the different viscosity reductions obtained from the vertical and horizontal experiments.

4.3.7.8 Uncertainty and application

The Fann 35 SA viscometer is an industry standard for testing the drilling fluids characteristics on site. It is a fast and reliable apparatus to measure the important parameters of drilling fluids. However, since there is no strictly defined accuracy for the Fann viscometer, the accuracy of this apparatus and repeatability of the tests is often debatable. By performing multiple calibration, verification and zero measurements during the experiments these uncertainties have been restricted as much as possible.

Since the annular space between the bob and rotor is small (only 1.17 mm), large particles can get stuck and from an obstruct during the measurements. This effect was noticeable when testing the 250-300 μm samples. Peaks and sudden drops on the Fann viscometer dial were observable, there were also two cases where grain crushing sounds could be heard during the high shear measurements.

Each batch of drilling fluid is prepared using the same drilling fluid recipe. However due to the many ingredient measurements and the mixing performed, it is possible that small difference were present between the drilling fluid batches. This uncertainty is limited by performing various zero measurements. The results showed no or negligible differences between the drilling fluid batches.

The vibrational experiments performed in this thesis do not represent the same conditions that will be present inside the pressurized settling tank. The experiments are performed with an open fluid surface while the drilling fluid will be enclosed inside the pressurized tank. This difference can reduce the obtainable viscosity reduction inside the pressurized tank, because shearing the fluid in an enclosed pressurized tank will be much more difficult. The concept of creating additional shear by vibrations depends on generating pressure differences to allow fluid motion which then result in additional shear reducing the fluid viscosity. Since the compressibility of the drilling fluid is poor and since it will be enclosed and pressurized, it will be difficult to create these pressure differences. The situation can be compared to a bottle which is completely filled with fluid. When the bottle is shaken the fluid inside will remain motionless. A promising solution for this problem is to have a compressible medium inside the tank, which enables fluid motion imposed by the vibrations.

4.3.8. Pressure filtration experiment results

The pressure filtration experiments are performed starting using the fine filters with gradually increasing pressures and are followed up by filters with larger pores. The obtained results for the various filters and pressure combinations did not show many differences. Nearly all experiments resulted in a clogged filter medium, which prevented the flow through the filter. The obtained results of the various tests are presented and discussed in this section.

4.3.8.1 The filtration results

During almost all performed experiments, the filter medium clogged due to the formation of a cake on top of the filter medium. This was expected, since filter cake forming during the filtration of clay suspensions is a known phenomenon in the drilling industry. The cake forming characteristics of clay suspensions are commonly used during drilling operations in order to seal the borehole walls and prevent the inflow of formation fluids. Clogging of the various filters was therefore not surprising. Finding a filter medium and pressure combination, allowing the separation of the fine particles without clogging the filter was therefore the main challenge.

Table 20 presents the results of the various pressure filtration experiments. Since all experiments ended up clogging the filters, no flow rate measurements were obtainable. In the single case where flow through the filter was possible, resulted in high flow rates which were also not measureable with the setup. The flow rate in this case was sufficient to empty the fluid reservoir of 250 ml within 2-3 seconds.

Table 20: Filtration results - x = clogged filter, r = ripped filter, o = flow through filter, '-' = not performed combination

Filter [μm]	Particle concentration and size [% vol.] [mm]	Applied pressure [bar]					
		0.25	0.5	1	2	4	6
20-25	0%	x	r	r	-	-	-
20-25	9% 150-212	x	r	r	-	-	-
20-25	17% 150-212	x	r	-	-	-	-
20-25	9% 250-300	x	r	r	-	-	-
20-25	17% 250-300	x	r	-	-	-	-
63	0%	x	x	x	x	-	-
63	9% 150-212	x	x	x	x	-	-
63	17% 150-212	x	x	x	x	-	-
63	9% 250-300	x	x	x	x	-	-
63	17% 250-300	x	x	x	x	-	-
105	0%	-	x	x	x	-	-
105	9% 150-212	-	x	x	x	-	-
105	9% 250-300	-	x	x	x	-	-
250	0%	-	-	o	-	-	-
250	9% 150-212	-	-	x	x	x	x
250	9% 250-300	-	-	x	x	x	x

The obtained experiment results can be compared to the sand screen criteria described by Coberly and Saucier mentioned in section 2.7. Evaluating the Coberly and Saucier criteria with realistic assumptions of D₅₀ and D₉₀, results in the required filter openings as presented in Table 21. Comparing these results with the experiment results, shows that the Coberly and Saucier criteria gives an underestimation of the filter opening. This effect can be related to the sealing properties of the bentonite clay.

Table 21: Filter openings required to retain sand particles based on Coberly and Saucier

		Filter openings required to retain sand particles [μm]		
		No additional particles d ₅₀ = 20 & d ₉₀ = 50 [μm]	150-212 μm particles d ₅₀ = 40 & d ₉₀ = 150 [μm]	250-300 μm particles d ₅₀ = 50 & d ₉₀ = 250 [μm]
Coberly (1937)	2 · d ₉₀	100	300	500
Saucier (1974)	5~6 · d ₅₀	100~120	200~240	250~300

4.3.8.2 Filter medium strength

The experiments are performed starting with a pressure difference of 0.25 bars and the pressure difference is gradually increased up to 6 bars. These pressures formed no problems for the relative strong steel and nylon wire filters, while the weaker Whatman filter papers ripped at pressure differences of 0.5 bars or greater. The rip occurred at the centre of filter, since the filter apparatus provided less support to the filter medium at this location. Because of this issue, the experiments performed with the fine Whatman filter papers were limited to a pressure difference of 0.25 bars. An example of a ripped filter is shown in Figure 55.



Figure 55: Ripped Whatman filter paper

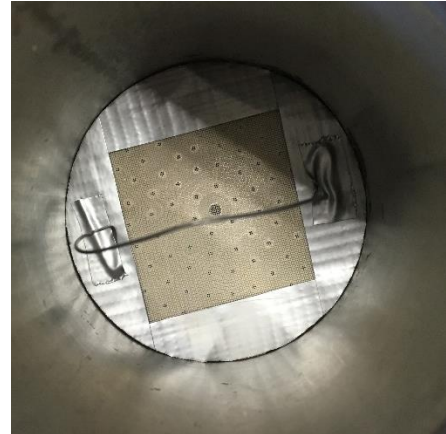


Figure 56: 250 μm filter inside the pressure filtration apparatus

4.3.8.3 The filter cake

There was no significant difference in the measured filter cake thicknesses. All filter cakes had a non-homogenous thickness varying between $\sim 1\text{-}2\text{ mm}$ over the filter surface. The filter cake created on top of the fine Whatman filter papers were stickier than the other filter cakes and had a slippery surface. The cakes formed on the 63, 105 and 250 μm filters had a non-homogeneous cake composition. The top part of these filter cakes was also sticky with a slippery surface, however the interface between the cake and filter was grainier and less sticky. This made cleaning of these filters very easy by backwashing them, which was not possible with the Whatman paper filters. Figure 57 till Figure 59 present various filter cakes obtained from the pressure filtration experiments.



Figure 57: Filter cake – 20-25 μm filter with no additional particles at 0.25 bar



Figure 58: Filter cake – 63 μm filter with 17% 150-212 μm particles at 1 bar



Figure 59: Filter cake – 250 μm filter with 9% 150-212 μm particles at 6 bar

The pressure filtration experiment performed with the 250 μm filter and drilling fluid without additional particles, resulted in no filter cake build-up. As shown in Figure 61, during this experiment almost no particles remained on top of the filter medium.



Figure 60: Filter cake - 250 filter with no additional particles at 1 bar



Figure 61: Filter cake - 250 filter with no additional particles at 1 bar close up

4.3.8.4 Influence of pressure difference

According to Darcy's law, mentioned in section 2.7, an increase in pressure difference will result in a greater flow rate through the filter medium. This is however only valid when the viscosity, filter cake thickness and filter resistance stay constant during the filtration process, which was not the case in the pressure filtration experiments. During the filtration experiments, the filter thickness and the filter cake resistance increase over time due to the forming of a filter cake.

One of the interesting concerns was the influence of pressure on the filter cake resistance. The filter cake is a compressible medium with certain porosity and permeability. Applying an increased pressure difference over the filter, compresses the filter cake reducing the filter cake porosity and thereby the permeability. The experiments performed by Engelhardt (1954) indicate that this relation is exponential for clay suspensions. This relation indicates that a relative small increase in pressure difference can result in a significant reduction of the filter cake permeability.

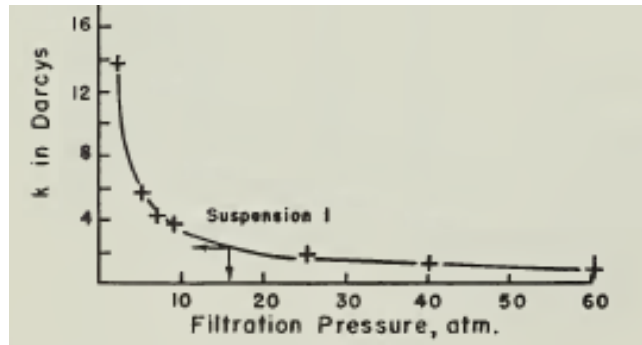


Figure 62: Filter cake pressure versus permeability based on Engelhardt (1954) [54]

During the preparation of each test, flow through the filter medium was present until the pressure filter was closed or a pressure was applied on the sample. After applying pressure, the filter clogged instantaneously causing no flow conditions. However, when the pressure was released flow through the previously clogged filter was possible again. These observations indicate that the filter cake was compressing by the applied pressure and thereby reduced the filter cake permeability.

4.3.8.5 Influence of particle size and concentration

As in the vibration experiments, various particle sizes and particle concentrations were mixed in the drilling fluid to understand the influence of these factors on the filtration process. However, since all experiments ended up clogging the filters, no results were obtained indicating a specific difference between the various test samples.

4.4. Chapter conclusion

Various experiments have been performed to study the influence of vibrations on the drilling fluid viscosity and the applicability of pressurized filtration. The results obtained from the experiments, which are presented and discussed in this chapter were promising and useful for increasing the separation tank efficiency. The conclusions can be summarized as follows:

Vibrational experiments:

- The applied vibrations reduce the apparent viscosity of the drilling fluid. The reduction effect is at its greatest when the drilling fluid is at a low shear state and reduces with increasing shear rate. This is related to the reducing shear-thinning behaviour of the drilling fluid with increasing shear rate and the decreasing influence of the additional shear created by the vibrations at high shear rates.
- The obtained apparent viscosity reductions vary for the various test cases depending on the shear state, vibration intensity, vibration setup, particle concentration and particle sizes. The apparent viscosity reductions obtained for the low shear states (5 and 10 [1/s]), which represent the shear rates in the settling tank are presented Figure 48 in section 4.3.7.2. The largest apparent viscosity reduction of 82% is obtained for a drilling fluid sample containing 17% vol% 250-300 μm particles in the vertical test setup at a shear rate of 5 [1/s] and a vibration intensity of 3g (50 Hz and 0.6 mm).
- The addition of 150-212 and 250-300 μm particles to the drilling fluid at volume concentrations of 9% and 17% increased the apparent viscosity respectively with ~10% and ~20%. However, the

additional particles had no significant influence on the obtainable viscosity reduction in the low shear region. The differences between the relative apparent viscosity reductions were in most cases within ~5%.

- The amplitude and frequency experiments showed that vibrations with a low frequency and large amplitude are more efficient. The two tested cases resulted in a ~10% greater relative apparent viscosity reduction in the low shear region. However, at higher shear rates the influence of different combinations frequency and amplitude became negligible. The frequency experiments also showed that the relation between vibration intensity and the obtainable viscosity reduction is not linear. With increasing vibration intensity, the efficiency of the vibrations decreases.
- The 10 sec gel strength measurements indicate that the drilling fluid sample have a reduced or no gel strength build up when exposed to vibrations. Samples containing larger particles at higher concentrations show no gel strength build up, while samples containing smaller particles at lower concentrations show a reduced gel strength build up.
- The various verification experiments showed that the settling of the added particles was negligible during the experiments. The samples containing 150-212 and 250-300 μm particles showed a maximum specific gravity reduction of respectively ~4% and ~7%. These specific gravity reduction resulted in negligible apparent viscosity changes in the low shear region.
- Verification experiments performed with 0.1 Pa·s Fann calibration fluid and a 10% glycerol solution, indicate that the vibrations did not influence the Fann measurements apparatus. The apparent viscosity reductions could therefore indeed be related to the shear-thinning effect of the drilling fluid.
- The lower apparent viscosity reductions obtained from the horizontal setup compared to the vertical setup are discussed and related to two phenomenon. The first one being the presence of hysteresis loops in the consistency curve of the tested samples due to thixotropic shear history dependent behaviour of drilling fluids. And secondly the different methods of introducing the vibrations to the fluid sample, resulting in the creation of different additional shear stresses in the drilling fluid.
- The vibrational experiments do not represent the same conditions that will be present in the pressurized settling tank. Obtaining similar viscosity reductions inside the pressurized settling tank will be challenging, since shearing the fluid will become difficult.

Pressure filtration experiments:

- During the pressure filtration experiments filter cake formed on top of the various filter mediums, which instantaneously clogged the filters. Among the tested samples, filtration was only possible for the clean drilling fluid sample filtered at 1 bar using a 250 μm filter medium. These results indicate that separation of fine particles by pressure filtration is not possible.
- Since practically all experiments ended up with a clogged filter medium, no significant differences were obtained for the various samples containing different concentrations of particle sizes.
- The filter cakes obtained from the experiments had a thickness of ~1-2 mm, varying over the filter surface. All obtained filter cakes had a slippery surface and were sticky when removed. The filter cakes formed on top of the 63, 105 and 250 μm filters had a non-homogeneous cake composition, consisting of a less sticky and grainy interface on top the filter medium.
- The paper filters used during the experiments ripped at pressure differences of 0.5 bars. This indicates that the tensile strength and support of the filter medium is important. Especially when the filters are realized in full scale this problem will become significant.
- The results of the pressure filtration experiments are discussed and related to two phenomenon: The first one is the formation of the cake filter. Since the permeability of the cake filter is much lower than the filter medium, the substantial part of the filtration process takes places on top of the filter cake. The openings of the filter medium are therefore only important for the initial filter cake forming and does not influence the remaining filter process. And secondly the influence of the pressure difference on filter cake permeability. A high pressure difference compresses the filter cake, reducing its permeability and thereby clogging the filters. This characteristic of drilling fluids and filter cakes is known in literature and is often used to seal the borehole walls during various drilling operations.

5. Modelling

The information obtained in the previous chapters has been combined to model the proposed settling tank using the computational fluid dynamics package of COMSOL Multiphysics 5.2. This chapter presents a brief overview of the COMSOL model, model assumptions and the simulation results obtained from the 2D and 3D simulations. By performing various simulations, the obtainable settling tank efficiency is evaluated including the achievable viscosity reduction due to vibration and an effective tank design.

5.1. The COMSOL model

The COMSOL Multiphysics software package is a Galerkin finite element method based solver. The software package includes a graphical user interface and a set of predefined modules, which can be used for the modelling of common applications. The wide variety of predefined equations, solvers and the option to modify almost everything, allows COMSOL users to combine and expand modules to simulate multiple types of physics together. The computational fluid dynamics (CFD) module is used to perform the 2D and 3D simulations of the settling tank.

The CFD module in COMSOL consists of several modelling tools that can be used to simulate fluid flow. The single-phase flow model with particle tracing and the dispersed two-phase fluid flow models are considered for the simulation of the settling tank. After performing several simple simulations with both models, the dispersed two-phase fluid flow model (mixture model) was chosen as the base for the 2D and 3D simulation.

Multiple simple simulations performed with the laminar flow model and a stationary solver, indicated that a laminar approach was not suitable for the fluid flow in the settling tank. The occurrence of turbulent flow conditions near the inlet and short circulations in the settling zone of the tank resulted in unstable and not converging models. The use of a turbulent flow model with time dependent solver was therefore necessary to obtain convergence and solve the Navier–Stokes flow equations. The chosen flow model for the 2D and 3D simulations is the Reynolds-averaged Navier–Stokes (RANS) based k-ε turbulent flow model.

The two-phase fluid flow model or so-called mixture model has been slightly modified to include non-Newtonian fluid behaviour. This is accomplished by transferring the equations for shear rate and shear rate related viscosity from the single-phase model to the mixture model. The power-law model was selected as a relationship between the shear rate and apparent viscosity.

A combination of 2D and 3D simulations are used to analyse the efficiency of the settling tank. The 2D models are used as fast preliminary simulations to come up with an effective tank design, whereas the 3D simulations are used for a more realistic approach.

The general input parameters that were used for the fluid and particle properties are presented in Table 22 and are similar to the input parameters used in the preliminary calculations in section 2.2.2. Additional parameters such as the K and n values for the power-law viscosity model are derived from the average Fann measurements that are taken from the reference drilling logs presented in Appendix C. The power-law parameters are calculated using the equations (63) and (64), which are valid for Fann measurements performed with the standard rotor-bob-spring combination (R1-B1-F1):

$$n = \frac{\log \theta_{Fann,600} - \log \theta_{fann,300}}{\log \omega_{Fann,600} - \log \omega_{Fann,300}} = 3.32 \cdot \log \frac{\theta_{Fann,300}}{\theta_{Fann,600}} \quad (63)$$

$$K = \frac{\tau}{\dot{\gamma}^n} \cdot 0.48 = \frac{\theta_{Fann,600}}{1022^n} \cdot 0.48 \quad (64)$$

Where: ω_{Fann} = Fann rotor speed [r/min], θ_{Fann} = Fann dial reading at the indicated rotor speed [lb/100 ft²], n = flow behaviour index [-] and K = flow consistency index [Pa·s]

Table 22: COMSOL input parameters

Component	Parameter	Values	Unit
Particles	Diameter	1, 3 and 5	[mm]
	Specific weight	2650	[kg/m³]
	Particle concentration	10	[%]
Fluid	Inflow	1000, 2000 and 3000	[L/min]
	Specific weight	1300	[kg/m³]
	Apparent viscosity	Power-law fluid $K = 0.75$ and $n = 0.55$	[Pa·s]

5.2. 2D and 3D model geometry

The tank geometries used in the 2D and 3D simulations are slightly different from each other. The 2D tank geometry used in the simulations is similar to the previously used tank dimensions for the preliminary calculations in section 3.2. This includes a rectangular settling tank with the dimensions presented in Table 23 and an inlet/outlet pipe diameter of 15 cm.

The geometry of the 3D tank differs slightly from the 2D tank and is based on a separate study performed at Huisman by students from Avans Hogeschool Breda [21]. The students designed among others a realistic outer geometry of the settling tank, which has been adopted in the 3D simulations. The geometry consists of a cylindrical tank with the dimensions presented in Table 23. Compared to the 2D tank, the diameter of inlet and outlet pipes are reduced from 15 cm to 5 inch (approx. 12.7 cm). This was necessary to satisfy the standardized pipe diameters used at Huisman.

The dimension of the internal tank elements are not mentioned here, since many combinations of different shapes and dimensions are used during the simulations. If the dimensions are essential, they are included alongside the presented results.

Table 23: 2D and 3D settling tank dimension

2D rectangular Tank	Length	5000	[mm]
	Height	2500	[mm]
	Width	2000	[mm]
3D cylindrical Tank	Length	5900	[mm]
	Diameter	2150	[mm]

5.3. Model assumptions and uncertainty

In order to model the settling tank, various assumptions were necessary to simplify and solve the problem. This section discusses these assumptions briefly and gives an indication of the introduced uncertainty in the simulations.

Simplifying the 3D settling tank problem into a 2D model required various assumptions regarding to the tank width, which drastically changed the inflow and outflow conditions in the 2D simulations. The first assumption included the reduction of the inflow velocity as compensation for the tank width. The second assumption was related to the conversion of the real inflow pipe to the 2D model. This required modelling of the inflow pipe as an inflow plane over the full width of the tank. Since the inflow plane has a much larger flow surface than the real inflow pipe, the inflow velocity had to be reduced. These reductions were required to obtain the correct simulation of the flow velocity in the settling zone of the model. However, reducing the inflow velocity also results in less turbulence near the inlet and therefore advantageous inflow conditions. The 2D model shows therefore a relative poor simulation of the inflow and outflow conditions that would be present in the real settling tank.

Meshing of the model geometry is important and can influence the accuracy of the simulations significantly. The Finite Element Method approach used by COMSOL to solve the model performs calculations on the mesh points and interpolates the results over the space in between. Using a finer mesh with more calculation points increases the accuracy of the simulation, but this also increases the calculation time since more calculations needed to solve the complete model. Finding a balance between the accuracy of the simulation and the computation time is always difficult.

The meshes used for the 2D and 3D models are created using the build-in physics-controlled meshing function of COMSAL. This option in COMSOL creates a mesh based on the expected activity in each section of the geometry. Since both tank geometries are relatively simple, a relative coarse mesh was enough to acquire stable simulation results within a reasonable computation time. The used meshes for 2D and 3D models are presented in Figure 63. As can be seen from both meshes COMSOL automatically refines the mesh around critical sharp edges and walls, whereas the elements in the centre of the tank remain coarse. This approach allows the model to be accurate at critical locations of the geometry, while saving on calculation time at locations where less activity takes place and therefore less accuracy is acceptable. This optimization is especially effective in the 3D mesh, since the geometry contains 35 times more elements as the 2D geometry. The 2D mesh presented in Figure 63 consists of 6205 domain and 343 boundary element, while the 3D mesh consists of 215907 domain, 16686 boundary and 1479 edge elements.

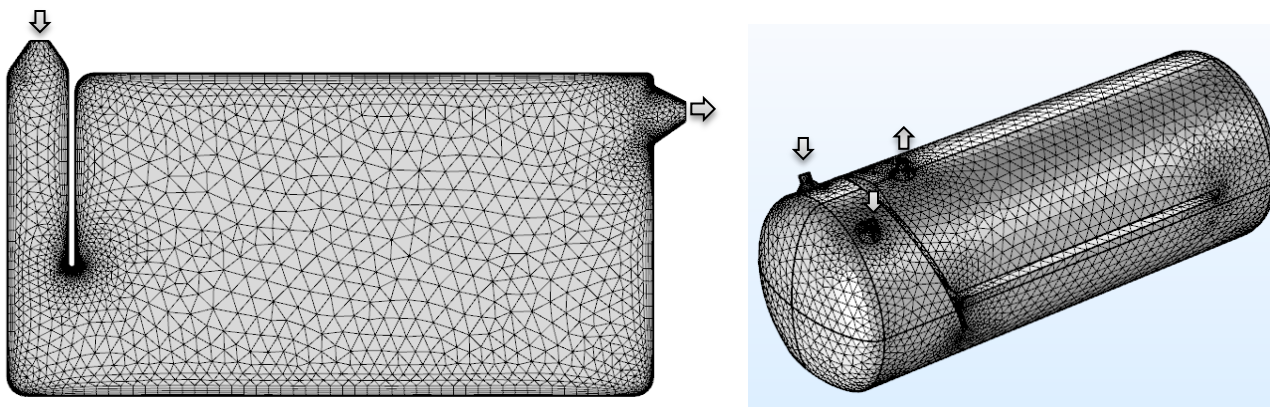


Figure 63: 2D and 3D meshes

To optimize the mesh and acquire faster computation times, small modifications were made to the tank geometries. The modifications include smoothing of various sharp edges and introducing smoother cone shaped inlet/outlet connections. These changes reduced the amount of locally created anomalies, resulting in a more stable model with a faster computation time.

Other uncertainties in the simulations are related to the accuracy, initial values and defined limits of the various formulations used by COMSOL. The default settings of these formulations are maintained during the simulations, since they represent a valid approach for common flow problems according to the COMSOL manual. The only modifications made that were made are limited to a slightly higher input value for the minimum shear rate definition of $\dot{\gamma}_{min} = 2 \text{ 1/s}$. This modification prevents the use of negligible small shear rate values in the power-law viscosity model, which otherwise would lead to very high apparent viscosities of the drilling fluid.

The RANS equation used by COMSOL to simulate the fluid flow, assumes that the fluid is incompressible. This is an assumption that is often made when modelling liquids, because it allows the simplification of the Navier-Stokes equation. The assumption can be seen as a valid approximation, since the compressibility of fluids is relatively much less than the compressibility of gasses at relative low pressures. Since pressure influences are neglected in the model, the simulations are performed at atmospheric pressures.

The influence of temperature on the drilling fluids viscosity is not included in the COMSOL models. As mentioned in section 2.4.7, fluctuations in temperature effects the drilling fluid viscosity and thereby the settling of particles.

To increase the model stability and computation time, accurate initial conditions are defined for the flow velocities and pressure fields in the settling tank. This allowed the model to converge faster at the start of each simulation.

The k- ϵ turbulence model is one of the commonly used models to simulate turbulent flow conditions. This two parameter model is a very popular model for industrial applications due to its good convergence and relatively low memory requirements. To lower the computation requirements, this model makes use of wall functions to simulate the start of turbulent flow near the walls in the so-called buffer or transition zone. This method reduces the accuracy in this thin zone, but increases the overall computation time of the model. Since the buffer zone is not significant compared to the size of the settling tank, the reduced accuracy is acceptable.

The various walls or boundaries of the system are defined with no fluid slip conditions. Boundaries that fulfilling the function of a sludge zone (particle discharge) are defined with a dispersed phase outlet condition. This allows continuous discharge of the settled particle at the bottom of the tank. This assumption is relatively advantageous, since in reality the method used for the removal of the settled particles will create flow disturbances at the interface.

5.4. Simulation results

This section of the chapter presents and discusses the 2D and 3D simulation results, which are obtained from various simulations. The 2D and 3D simulation results are considered separately to focus the contribution of each type of simulation.

5.4.1. 2D simulations

The 2D simulations are performed to understand the influence of various tank designs on the settling efficiency of the separation tank. A selected set of the considered tank designs are attached in Appendix B. The considered tank designs consist of multiple horizontal and vertical settling designs with varying: baffles, screens, inlets and outlet combinations. Designs of already existing wastewater treatment tanks are also considered in the simulations by scaling them down to the size of a 20ft container.

The figures below represent the simulation results for one of the many tanks designs. The presented results are obtained for a simulation after 10 minutes of constant inflow. The used inflow rate was fixed at 3000 L/min with a 10% concentration of 3 mm particles. The presented figures include the following: the flow velocities, particle concentrations, shear rate, apparent viscosity and the average particle concentration in the flow that is leaving the tank.

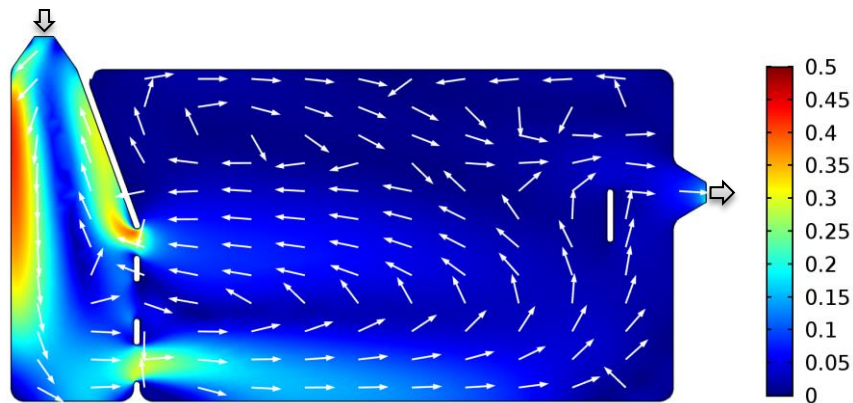


Figure 64: 2D simulation - Flow velocity [m/s] and flow field

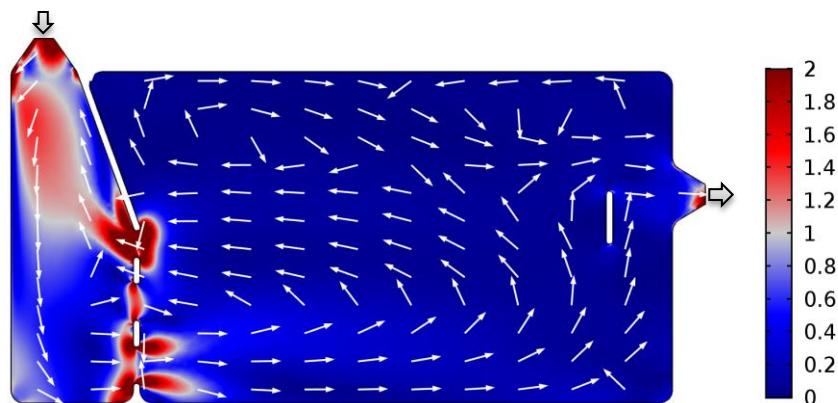


Figure 65: 2D simulation - Shear rate [1/s] and flow field

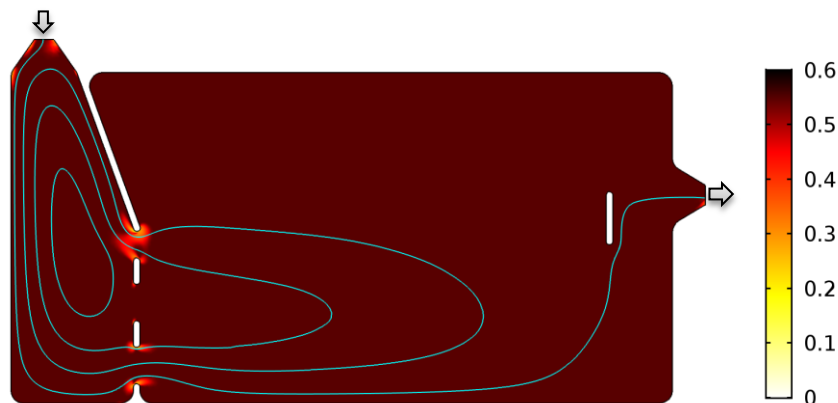


Figure 66: 2D simulation - Apparent viscosity [Pa·s] and stream lines

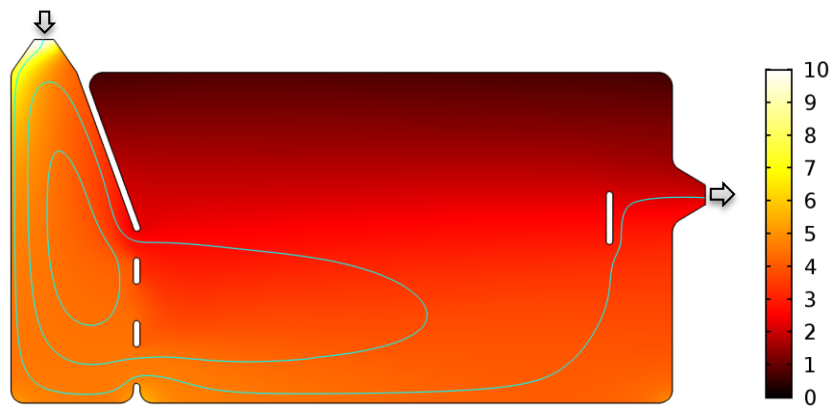


Figure 67: 2D simulation - Particle concentration [%] and stream lines

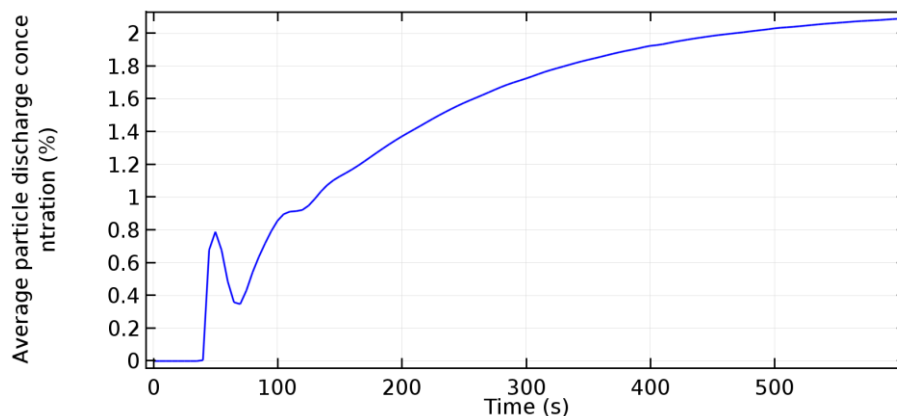


Figure 68: 2D simulation - Average particle discharge concentration at the outlet [%]

The different figures provide a wide range of information about the flow conditions and the settling efficiency of the tank. Figure 64 for example, points out that the flow conditions are not optimal in the settling zone of the tank. The flow field indicates the existence of short circulations, which decrease the efficiency of the settling tank. The flow velocities on the other hand are low, which is advantageous for settling. The low flow velocities result in low shear rates as presented in Figure 65. The high shear rates are limited to sharp corners and locations with a relatively high flow velocity. The variation in shear rates influences locally the apparent viscosity of the drilling fluid as shown in Figure 66. When all these influences are combined the settling of particles can be followed by particle concentration distribution plot shown in Figure 67. The high particle concentration in the settling zone and near the outlet, suggests a poor settling tank performance. This can be confirmed by plotting the average concentration of particles in the fluid leaving the tank as shown in Figure 68. This figure indicates that the drilling fluid leaving the tank still has an average particle concentration of $\pm 2\%$ vol% of 3 mm particles.

The various other 2D simulations are evaluated similarly as the example above. The results from these evaluations can be briefly summarized as follows:

- When horizontal inlets are used, a density difference between the inflow and the fluid in tank causes the occurrence of density flows. The density flow points downwards while the inflow direction is horizontal, this causes flow disturbance near the inlet and leads often to short circulations. Vertical inlets are less sensitive to this phenomenon, since the inflow direction is similar to the direction of the density flow for these cases. The influence of density flow is significant in the 2D simulations, since the inflow velocities are low due to the model assumptions. In reality, the inflow velocities will be much greater and more turbulent, which will result in a smaller influence of momentum driven flows.
- Placing inlets and outlets near the bottom of the tank leads to high velocities near the sludge zone interface. These high velocities are undesired, since they can cause the resuspension of settled particles.

- Baffles located near the inlet forcing the inflow downwards are effective, since they reduce the settling distance of particles to the sludge zone. A shorter settling distance results in a faster settling time, increasing the settling tank efficiency. However, the baffles also reduce the available flow section in the tank, which results in an increased flow velocity and flow disturbances in the sedimentation zone of the tank. These flow conditions reduce the settling efficiency locally and are especially critical near the sludge zone interface. A long baffle length can result in high and turbulent flows conditions underneath the baffle, causing resuspension of particle at the sludge zone interface.
- Baffles placed at different angles are found to be more efficient than vertically placed baffles, since they gradually increase the available flow section and therefore gradually reduce the flow velocity. However, the area left behind the baffle is often unused and causes significant flow disturbances in the settling zone. When curved baffles are used instead of straight ones, the flow velocity reduction happens more progressively. However, the space behind the curved baffle also causes greater flow disturbances in the settling zone.
- The use of perforated screens with various large openings (no pressure build up), which were aimed to control flow patterns, did not result in satisfying results. The occurring turbulence and short circulations could not be isolated to the inlet zone, nor did the screens function as flow diffusers. The screens were not able to control the flow without creating a pressure difference over the screen. The additional shear created at the screens was limited but significant enough to locally reduce the drilling fluid viscosity. Since the use of the screens can cause various practical problems considering maintenance, the screens were undesired and not future considered in the tank designs.
- The scaled versions of the wastewater treatment tanks are efficient settling tank designs, dealing with most of the problems encountered in the 2D simulations. However, due to the smaller size, new design problems arise and various designs do not function the same way as intended with the full-scale wastewater settling tanks. Most issues arise at the much shorter sedimentation zone, which is almost 10 times shorter compared to a full-scale wastewater treatment tank.
- The vertical settling tank designs showed promising separation performances for large cuttings. However, the efficiency of the system decreases with smaller particles, as the difference between the particle settling velocities and upwards flow velocity becomes smaller. Particles that are not settling fast enough are carried upwards to the outlet by the upwards flow or are pushed by other particles.
- The tanks including a combination of vertical and horizontal settling design showed promising separation efficiency. These designs are practical and effective, since the large will settle in the vertical section whereas the small particles can settle in the horizontal section. This is advantageous, since large particles settle at higher velocities causing turbulent conditions, which reduce the settling efficiency of the smaller particles. However, due to the limited tank dimensions, the horizontal settling section becomes too short to settle the smaller particles.

The information obtained from the numerous 2D simulations is evaluated and it is chosen to continue with the baffled two-floor settling tank design. This tank design makes great use of the available tank space and considers the various discussed issues. The design is future optimized by performing a sensitivity analysis on the dimensions of the internal tank elements. The plots regarding the sensitivity analysis are attached in Appendix B. The selected final tank design is shown in the figures below for a case with an inflow rate of 3000 L/min and a 10% vol% concentration of 3 mm particles.

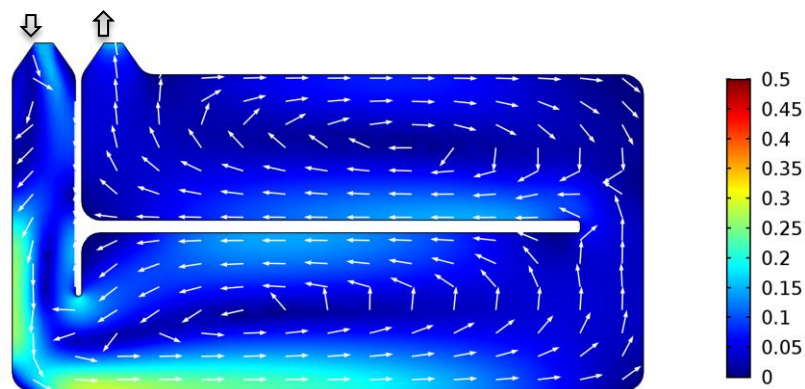


Figure 69: 2D simulation of the final baffled two-floor tank - Flow velocity [m/s] and flow field

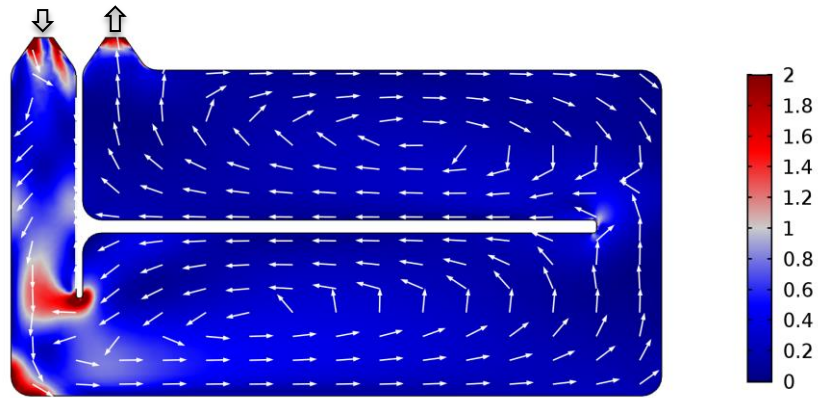


Figure 70: 2D simulation of the final baffled two-floor tank – Shear rate [1/s] and flow field

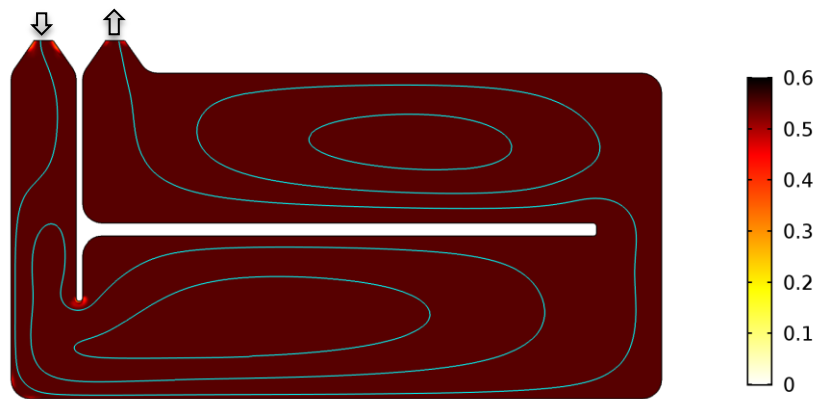


Figure 71: 2D simulation of the final baffled two-floor tank – Apparent viscosity [Pa·s] and stream lines

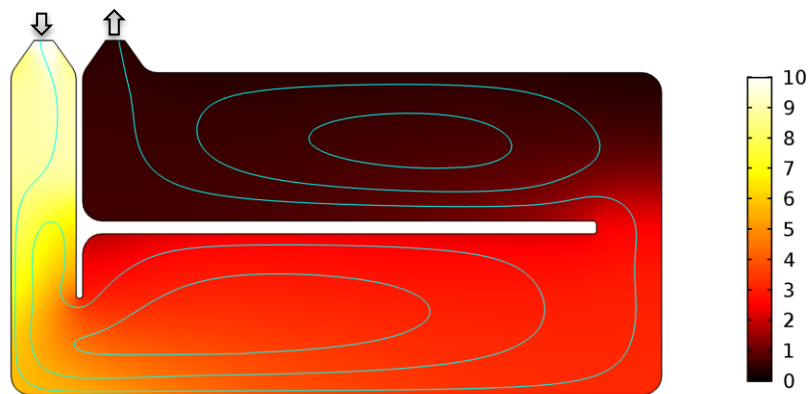


Figure 72: 2D simulation of the final baffled two-floor tank - Particle concentration [%] and stream lines

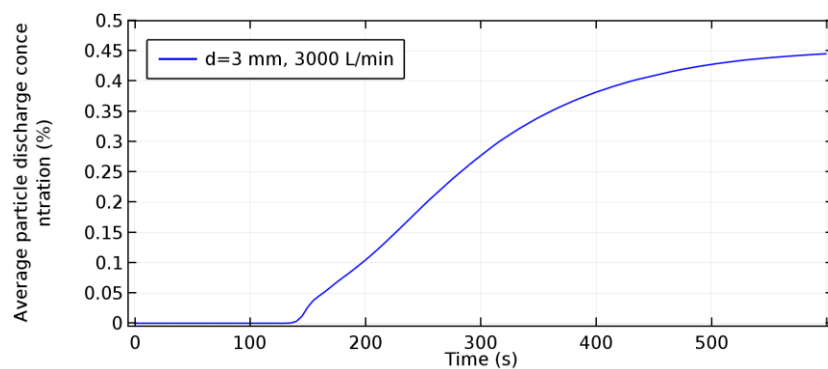


Figure 73: 2D simulation of the final baffled two-floor tank - Average particle discharge concentration at the outlet [%]

As the figures indicate the baffled two-floor tank designs performs better than the previously presented example. This design is however more complex since it uses two decks to settle the particles, which requires additional equipment inside the tank.

The flow velocity and flow field plot presented in Figure 69 indicates that the tank still contains short circulations. The circulations are however, more stable and the results indicate that the circulations are probably influencing the settling process positively. The same figure also shows a relative high flow velocity near the bottom sludge zone, which can cause resuspension of the fine particles. This problem does not occur on the top sludge zone.

Since there are no screens in the tank design, the high shear stresses are limited to the few sharp edges as can be seen in Figure 70. The consistent shear profile in the tank results in an almost constant apparent viscosity in the tank as shown in Figure 71. The occurring shear is not significant enough to influence the viscosity and increase the settling efficiency of the tank.

The particle concentration plot in Figure 72 points out that the particle concentration in the fluid on the second layer is much less, than on the bottom layer. This result points out that bottom layer works efficient, while the residuals can settle on the second layer. Evaluating the average particle discharge concentration presented in Figure 73, shows that a constant outflow concentration is reached after 10 minutes. The remaining concentration of 3 mm particles in the outflow is 0.45% vol%, which is much less than the previously obtained 2%.

The obtained efficiency from the baffled two-floor tank design is reasoned to be sufficient. The design is future evaluated using 3D simulations to reduce the assumptions that were necessary in the 2D model.

5.4.2. 3D simulations

The 3D simulations are performed to decrease the inaccuracies of the 2D model by reducing the assumption at the inlet and outlet zones of the tank. By doing so, a more realistic simulation of the settling tank efficiency could be obtained. To study efficiency and capabilities of the selected design further on, a sensitivity analysis is performed using the 3D model, with varying inflow rates and particle diameters.

As mentioned in section 5.2, the outer tank design of the 3D model is based on a separate study performed by students from the Avans Hogeschool Breda and consists of a cylindrical tank instead of a rectangular one. The internal tank design is kept similar to the baffled two-floor tank from the 2D simulations. To account for the space taken by the sludge removal system, a section of 250 mm in high is removed from the bottom part of the tank. Since the inflow in the 3D model is concentrated, more turbulence was expected in the inlet zone. To provide the inflow jet more space to dissipate energy, the vertical baffle is placed at an angle of 20 degrees. An overview of the 3D tank design is presented in Figure 74. Table 24 includes the dimensions of the internal tank elements and provides a cross section with the dimensions.

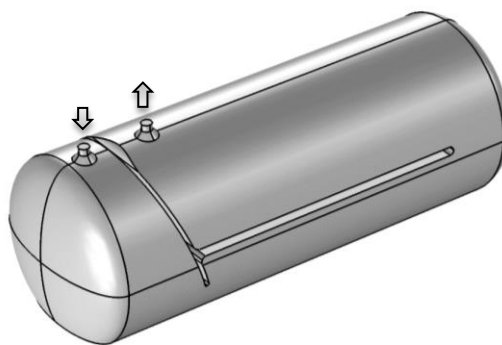


Figure 74: 3D simulations - 3D tank design overview

Table 24: Dimensions of internal elements 3D model

Vertical baffle	Length	1500	[mm]
	Angle	20	[°]
	Distance between baffle and bottom of the tank	500	[mm]
Horizontal floor	Length	3500	[mm]
	Distance between floor and bottom of the tank	925	[mm]
	Width of the flow space on the side of the floor	1100	[mm]

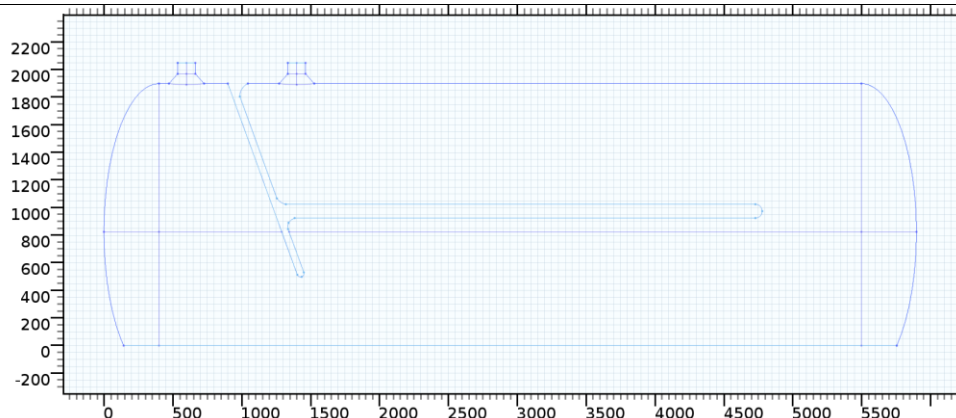


Figure 75: 3D simulations - 3D tank design cross section with dimensions [mm]

5.4.2.1 Single and double inlet results

The first 3D simulation has been performed using only one inlet pipe with an internal diameter of 5 inch (approx. 12.7 cm). These simulations revealed the occurrence of a jet flow at the inlet, which was reaching the bottom of the settling tank. This resulted in high flow velocities at the sludge zone, which could lead to resuspension of the settled particles. To prevent this from happening it was chosen to distribute the inflow between two inlet pipes, instead of using diffuser plates. The use of diffuser plates would result in a high rate of wear on the plates due to the combination of high velocities and large particle concentrations.

The results of the single and double inlet simulations are presented in Figure 76 and Figure 77 for a period of 10 minutes with a constant inflow rate of 3000 L/min. The drilling fluid used in these simulations had a power law based viscosity and consisted of 10% vol% concentration of 3 mm particles.

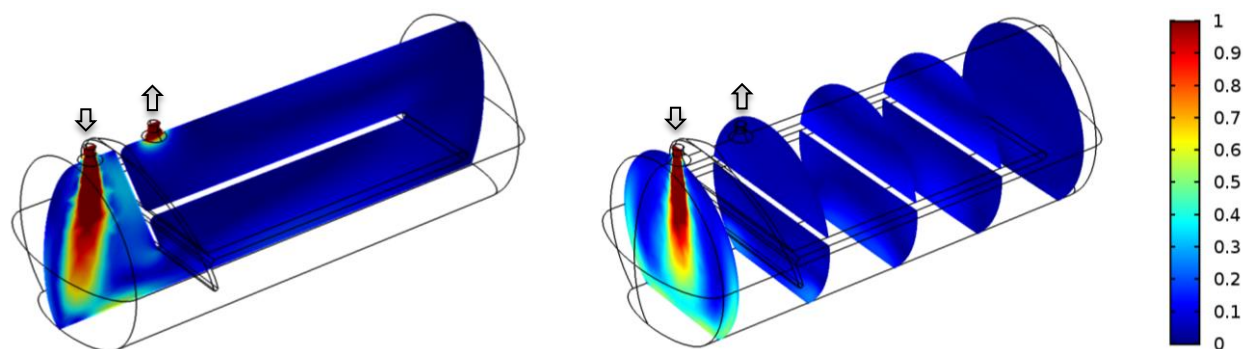


Figure 76: 3D simulations - Single inlet flow velocity [m/s] side and multi-plane view

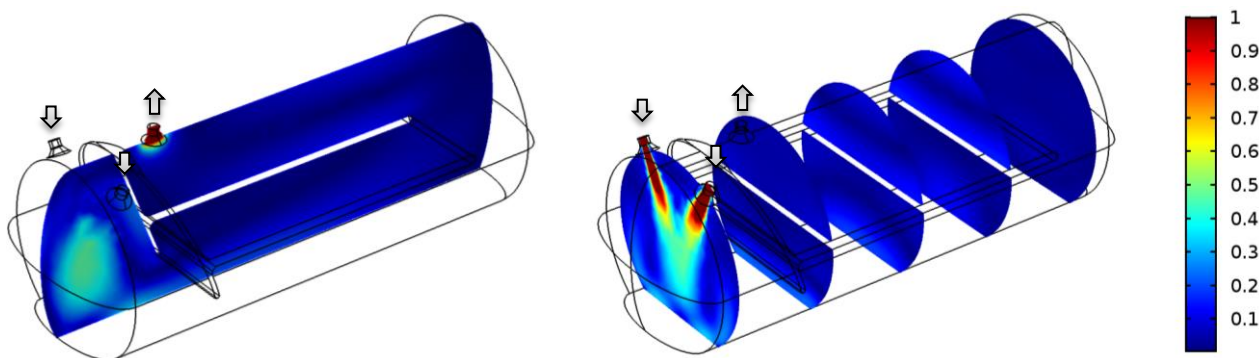


Figure 77: 3D simulations - Double inlet flow velocity [m/s] side and multi-plane view

As the figures indicate, the double inlet design results in lower flow velocities near the sedimentation bed compared to the single inlet option. Since the lower velocities are favoured, the double inlet option is chosen to be evaluated further on.

5.4.2.2 3D simulation results for a power-law based viscosity

To study the separation efficiency of the double inlet settling tank design, multiple simulations have been performed for varying inflow rates and particles sizes. A selected set of the obtained particle concentration plots are presented in the figures below. The remaining parameter combinations are attached in Appendix B.

Similar to the previous simulations, a power-law based viscosity is used to describe the relation between shear rate and viscosity. The presented results are obtained after 10 minutes of constant inflow with a 10% vol% concentration of particles. The inflow rate and particle sizes were changed throughout simulation.

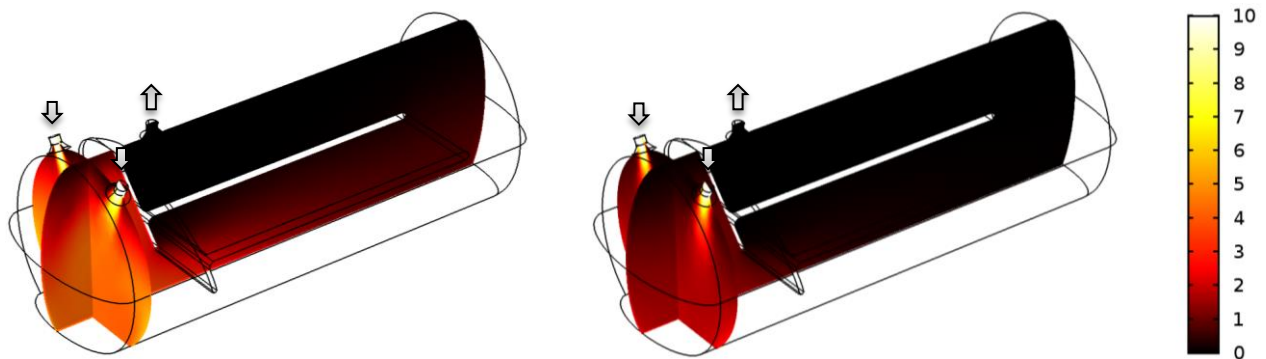


Figure 78: 3D simulation power-law - Particle concentrations [%] for an inflow of 3000 and 1000 L/min and particles of 5 mm

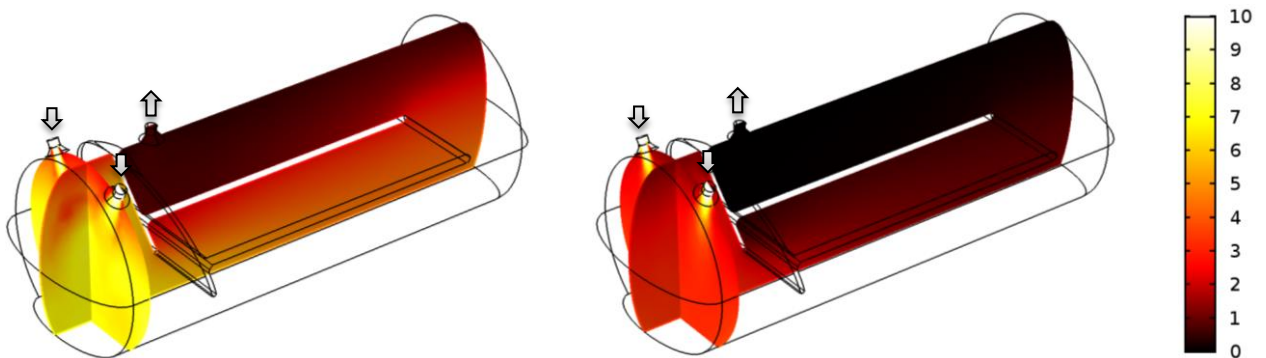


Figure 79: 3D simulation power-law - Particle concentrations [%] for an inflow of 3000 and 1000 L/min and particles of 3 mm

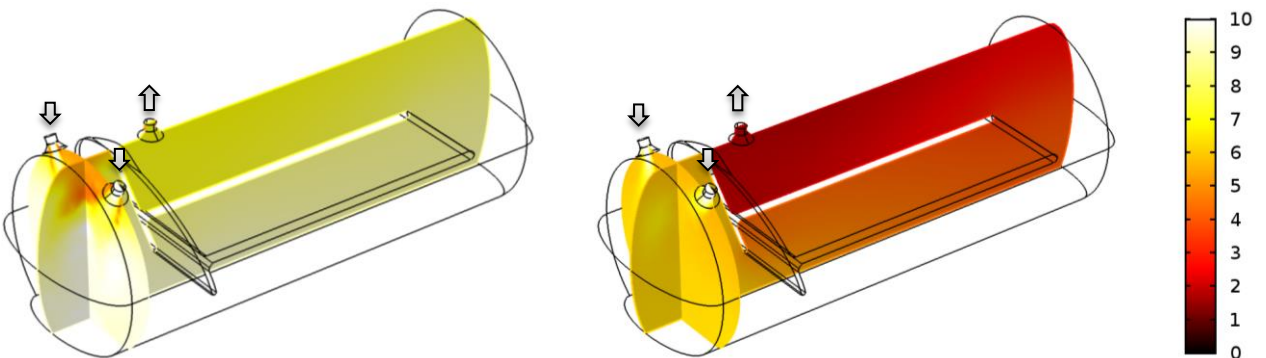


Figure 80: 3D simulation power-law - Particle concentrations [%] for an inflow of 3000 and 1000 L/min and particles of 1 mm

The presented figures indicate that the efficiency of the separation tank reduces with decreasing particle size and with increasing inflow rate. These results match the previously obtained results from the preliminary calculations. It is also noticeable that the plots of the 3D simulation case with an inflow rate of 3000 L/min and 3 mm particles are almost identical to the previously obtained 2D simulation results. To validate this suggestion, the average particle concentration in the outflow of the tank is plotted in Figure 81.

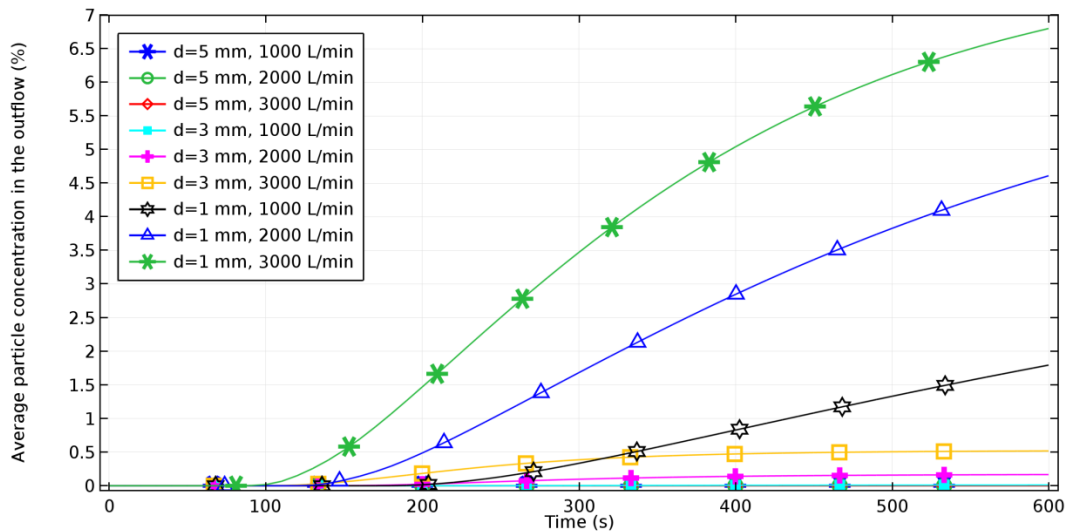


Figure 81:3D simulation Power-law - Average particle discharge concentrations at the outlet [%]

When Figure 81 is compared to Figure 73, it can be confirmed that the results of the 3D simulation case with 3000 L/min and 3mm particles is practically similar to the 2D simulation results of the baffled two-floor tank. However, the average particle concentration reaches the equilibrium faster in the 3D simulation compared to the 2D. The results can also be presented as the removal ratio over time, see Figure 82.

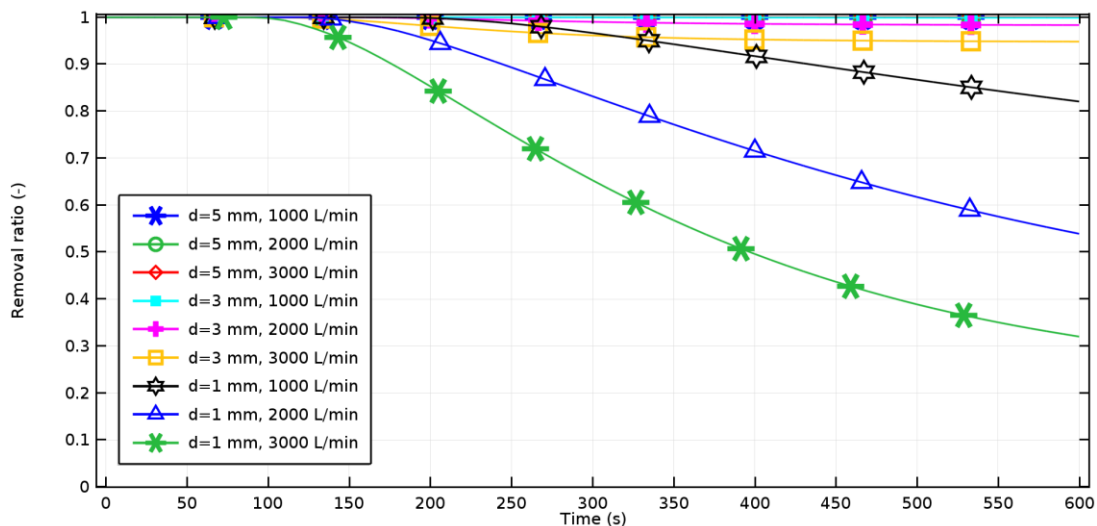


Figure 82:3D simulation Power-law - removal ratio [-]

With the information in Figure 81 and Figure 82, it is possible to evaluate the separation efficiency of the selected settling tank design. The simulation cases point out, that particles greater than 5 mm will settle and a negligible concentration will be left in the discharge flow. The 3 mm particles also settle for low inflow rates, however when the inflow rates are increased they do not settle completely, which results in a remaining particle concentration of 0.5% vol% in the outflow. The fine particles are the most problematic to settle and this can be confirmed from the graphs. For every considered inflow rate, a significant concentration of 1 mm particles remains in the outflow. The steep slopes of the 1 mm curves also indicate that the particle concentration in the outflow has not reached equilibrium. The presented concentrations for the 1 mm particles will therefore increase even more when a longer time scale than 10 minutes is considered.

5.4.2.3 3D simulation results with the influence of vibrations

In the previous chapters, it has been proven that vibrations can reduce the viscosity of the drilling fluid to increase the settling rate of particles. To study the influence of vibrations on the achievable separation efficiency of the double inlet settling tank design, an additional set of 3D simulations were performed.

To implement the influence of vibrations in the COMSOL model, the existing model had to be modified by implementing another physics module. This would make the more complicated but more importantly, it would increase the computation time significantly. Since the 3D model already takes a significant amount of computation time to solve, this option is avoided. A more simple method to implement the influence of the vibrations to the simulations was possible through directly inputting a reduced viscosity as the drilling fluid viscosity. This option assumes that vibrations reduce the viscosity in all sections of the tank with the same amount, which introduces uncertainty into the model.

The influence of the vibrations is implemented in the model through replacing the drilling fluids shear depended power-law viscosity by a fixed and reduced apparent viscosity. Since the shear rates are low and constant in the settling zone of tank, the influence of shear depended viscosity becomes insignificant. Replacing the shear depended viscosity with a fixed viscosity is therefore acceptable, since it does not introduce a significant uncertainty.

The fixed viscosity value of 0.2 Pa·s is selected for the simulations by considering the highest apparent viscosity obtained from the reference drilling fluids and reducing it by the influence of the vibrations. The highest apparent viscosity obtained from the reference drilling fluids was 0.6 Pa·s at a shear rate of 5 1/s. This viscosity value is reduced by 66% based on the achievable viscosity reductions, which were obtained from the experiments presented in chapter 4. A greater viscosity reduction of 80% could have been chosen, however to obtain dependable results a slightly lower viscosity reduction is considered. This low viscosity reduction, also accounts for the uncertainty created by the implementation method of the vibrations.

Since the fixed viscosity is only applied on the drilling fluid, other process in the model were not affected. The influence of a varying particle concentration for example, was still able to modify the apparent viscosity of the drilling fluid containing a certain amount of suspended particles.

The simulations are performed similar to the previous simulations, with varying inflow rates and particles sizes. A selected set of the obtained particle concentration plots are presented in the figures below. The remaining parameter combinations are attached in Appendix B. The presented results are obtained after 10 minutes of constant inflow with a 10% vol% concentration of particles. The inflow rate and particle sizes were changed throughout simulation.

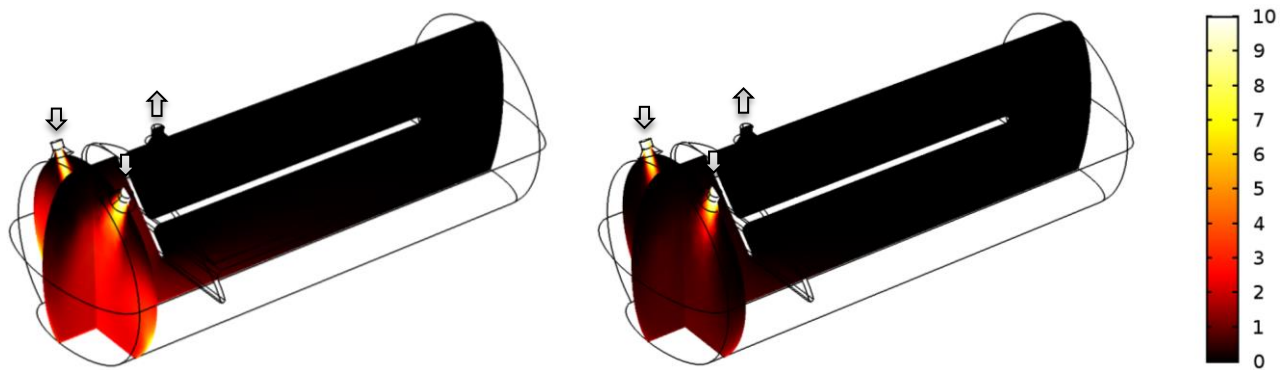


Figure 83: 3D simulation fixed viscosity - Particle concentrations [%] for an inflow of 3000 and 1000 L/min and particles of 5 mm

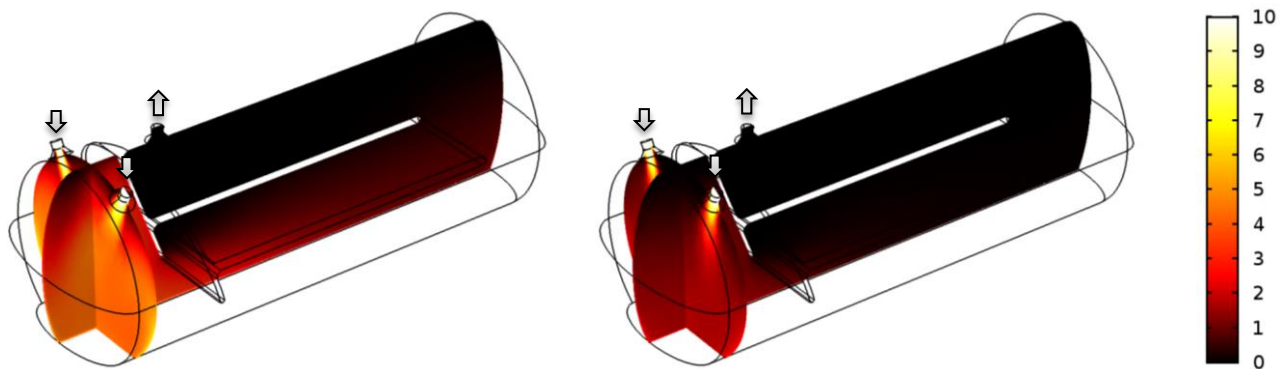


Figure 84: 3D simulation fixed viscosity - Particle concentrations [%] for an inflow of 3000 and 1000 L/min and particles of 3 mm

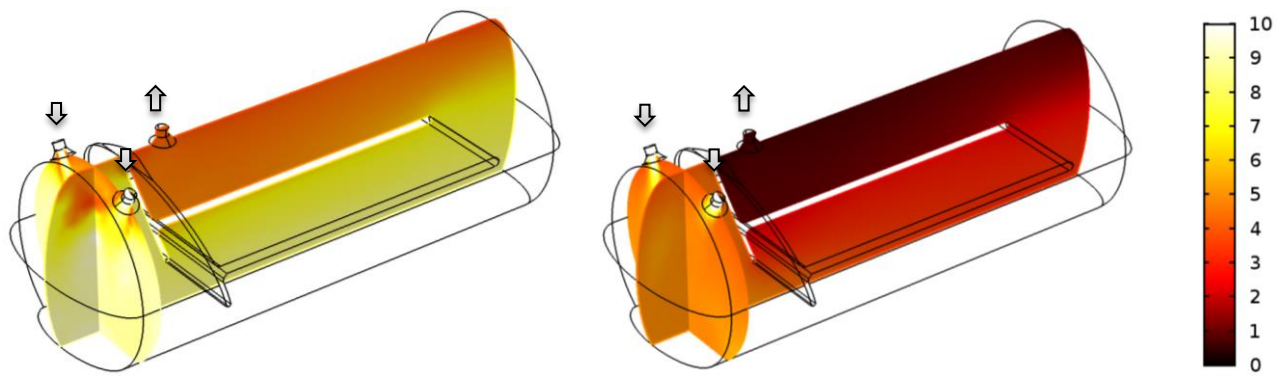


Figure 85: 3D simulation fixed viscosity - Particle concentrations [%] for an inflow of 3000 and 1000 L/min and particles of 1 mm

When the presented results are compared to the previously obtained power-law simulation results, differences can be noticed in the particle concentration plots. The results suggest that the particles settle faster for the fixed viscosity simulation case. This was already expected, since a lower viscosity increases the settling velocity of particles, as proven by the preliminary calculations presented in chapter 3. The particle concentration plots of the 5 mm particles point out that these particles settle almost directly after entering the tank, while the 1 mm particles stay in suspension for much longer. To evaluate the tank efficiency future, the average particle concentrations in the outflow of the various simulations are plotted in Figure 86 and the removal ratio over time in Figure 87.

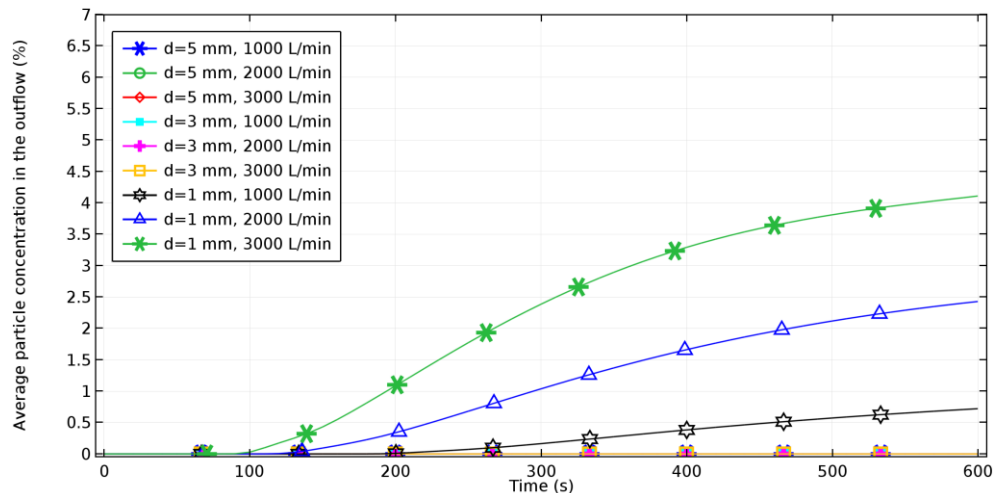


Figure 86: 3D simulation fixed viscosity - Average particle discharge concentrations at the outlet [%]

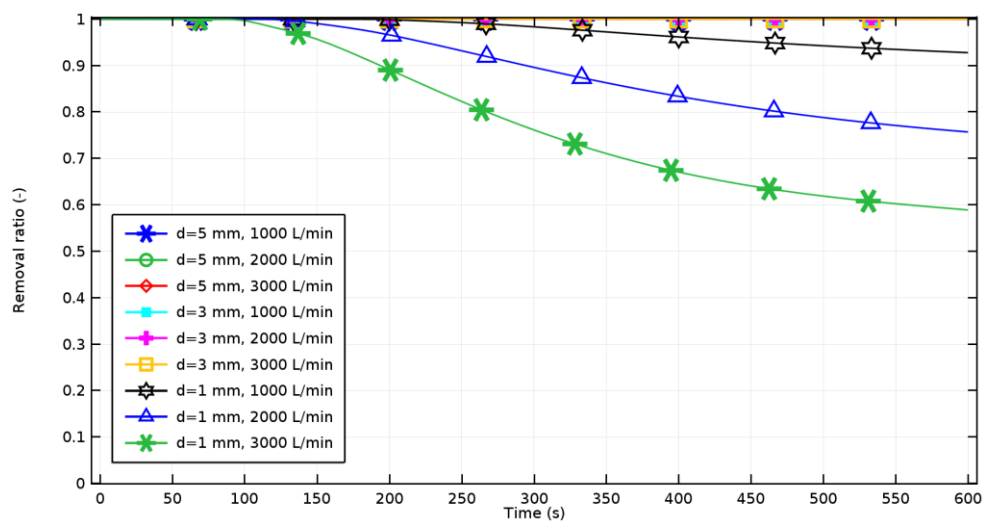


Figure 87: 3D simulation fixed viscosity - removal ratio [-]

By comparing Figure 86 and Figure 87 to Figure 81 and Figure 82, it can be observed that the separation efficiencies of the fixed viscosity simulations are more satisfying compared to the power-law simulations. The noticeable differences between the simulations can be summarized as follows:

- The particles settle faster in the fixed viscosity simulations due to the reduced viscosity. This results in a greater separation efficiency of the settling tank.
- The fixed viscosity simulations point out that the 3 mm particles settle completely for all considered inflow rates. For the power-law simulations, this was only possible when the inflow rate was reduced to the smallest value of 1000 L/min.
- The less steep curves in
- Figure 86, point out that a stable outflow concentration of 1 mm particles will be reached sooner for the fixed viscosity simulations.

Figure 86

- Figure 86 also points out that the separation of the 1 mm particles is more efficient in the fixed viscosity simulations. When the smallest inflow rate of 1000 L/min is considered, the remaining concentration of 1 mm particles in the outflow becomes $\pm 1\%$ vol%.

5.5. Chapter conclusion

Various 2D and 3D simulations have been performed to study the achievable separation efficiency of the settling tank. This is accomplished by evaluating numerous 2D simulations to find an effective tank design, which is then evaluated using 3D simulations. The separation efficiency of the selected tank design is assessed in the 3D simulations for cases with and without vibrations. The results obtained from the simulations can be summarized as follows:

- The 2D simulations point out that the settling tank dimensions and the internal tank design are important factors that have an influence on the separation efficiency. The separation efficiency can be improved significantly by using internal tank elements to control the settling processes in the tank.
- For relative small sized settling tanks, the separation efficiency decreases significantly due to the relative large influence of the inlet and outlet zones.
- The vertical settling tank designs are very effective for the settling of the relative large particles, however the separation efficiency decreases rapidly for smaller particles.
- Two layered settling tank designs are effective to increase the separation efficiency of relative small settling tanks. However, adding a second settling zone to the tank complicates the sludge removal systems.
- The 3D tank simulations point out that the selected tank design is able to settle particle between 3-5 mm completely for a representative case. This includes an inflow rate of 3000 L/min and a general drilling fluid described by a power-law viscosity model.
- When the influence of vibrations on the drilling fluid viscosity is included, the separation efficiency improves. The reduced viscosity makes it possible to settle particles between 1-3 mm for the representative case, with an inflow rate of 3000 L/min.

6. Conclusion and recommendation

The main conclusions of this thesis are summarized in this chapter in order to evaluate the project objective. This chapter also includes several recommendations for future research and development.

6.1. Conclusions and evaluation of the project

The project objective of this thesis is repeated below in red. In order to achieve the project objective, a literature study is performed, preliminary calculations are made, experiments are executed and simulations are assessed throughout this thesis. The results of these activities are combined in this section to evaluate the feasibility of the separation tank.

Perform a feasibility study for a pressurized solids separation tank, which uses gravitational settling and precise filtration as separation techniques to separate suspended solids down to 20 microns.

Conclusions of gravitational settling and vibrations

- Based on the results obtained from the calculations and simulations, it can be concluded that the separation efficiency of the gravitational settling tank is not sufficient to meet the particle separation requirement of 20 microns. The settling velocity of the fine particles is not sufficient to settle the particles before they reach the outlet.
- Vibrations can be used to reduce the apparent viscosity of the water based drilling fluid at the low shear range to increase the settling rate of particles. This improves the separation efficiency of the gravitational settling tank significantly, depending on the intensity of vibrations and the shear state of the WBM.
- The vibrational experiments do not represent the same conditions that will be present in the pressurized settling tank. Obtaining similar viscosity reductions inside the pressurized settling tank will be challenging and requires attention, since the application will be more difficult.
- The settling tank dimensions and the internal design of the tank have a significant influence on the settling process. An effective design can improve the separation efficiency by reducing the influence of the inlet/outlet zones and by increasing particle retention time.
- Based on the simulations, settling of particles is achievable for diameters greater than 3 mm and 1 mm respectively for cases without and with vibrations, these results are obtained for a 20ft two-layered settling tank, a common water based drilling fluid viscosity and inflow rates of 1000-3000 L/min containing particle concentrations of 10% vol%.

Conclusions of pressure filtration

- Based on the filtration experiments, it can be concluded that pressure filtration is not a suitable method to separate fine particles from the water based drilling fluid.
- Filter cake builds up on top of the fine filter medium, which causes the filters to clog. Since the filter cake forms instantaneously, no filtration is possible.
- The pressure difference applied over the filter system compresses the filter cake decreasing its permeability. This makes the use of high pressure differences inefficient.

Feasibility of the solids separation tank

As the evaluation of the individual separation methods point out, the application of the pressurized solids separation tank to separate particle down to 20 microns is not feasible. Gravitational settling does not meet the separation requirements and pressure filtration is not effective to separate the fine particles.

However, the separation of particles by gravitational settling is a promising separation technique, especially when vibrations considered. The method is capable of separating a large quantity of the cuttings generated during drilling process. Only the fine sized cuttings smaller than 1 mm remain in the drilling fluid, which needs to be further separated by other methods like filtering.

The proposed combination of gravitational settling and pressure filtration might not be feasible, but there are definitely other combinations possible to achieve the separation requirement. By future developing the settling tank design and performing additional research on other separation methods to separate the fine sized particles, the project objective is achievable.

The verified effects of vibrations on the drilling fluid can be used to improve the separation efficiency of other separation techniques or be used as a starting point for the development of a completely different separation application.

6.2. Recommendations

This section includes the recommendations for future development of the separation tank and provides several recommendations for future research.

- The dimensions of the settling tank can be increased to obtain a longer particle retention time in the settling tank. This will provide the particles more time to reach the sludge zone.
- The internal design of the settling tank can be further optimized to reduce the influence of the inlet/outlet and to provide improved settling conditions in the settling zone.
- Separation by gravitational settling in a tank, can be combined with the following mud treatment equipment to achieve the separation requirement of the project:
 - A combination with fine screen shale shakers is possible to separate fine particles down to 74 microns. The linear shaking motion of the shale shakers will probably reduce or prevent the formation of a filter cake on top of the fine filter screen.
 - A combination with a mud cleaner setup is suggested for weighted muds to separate fine particles down to 74 microns. Since the drilling fluid is pressurized in the settling tank, no additional pumps will be necessary to feed the drilling fluid into the hydrocyclones units of the mud cleaner.
- Additional influences such as the influences of temperature and pressure on the settling velocity can be implemented in the ideal horizontal settling tank model. This will provide more information to study the influence of these factors on the settling velocity of particles.
- The results obtained from the vibrational experiments can be improved by using a more accurate viscometer or by considering a different spring, bob, rotor configuration for the Fann viscometer. The use of a different bob and rotor configuration with a larger shear gap, will also allow the analysis of larger cuttings.
- The additional shear in the drilling fluid created by the vibrations can be measured to study the relation between vibration intensity and additional shear in the drilling fluid.
- Continuous temperature measurements during the vibration experiments are advised to obtain more information about the influence of temperature.
- It is recommended to investigate the applicability of vibration to reduce or prevent the filter cake formation during the pressure filtration experiments.
- To separate the fine particles from the drilling fluid, the application of self cleaning filters can be considered. Self cleaning filters make use of backwashing or mechanical scraping to clean the filters, which can improve the filtration performance. However, since filter cake forms instantaneously during pressure filtrations, a high cleaning frequency is probably required. This will reduce the performance and also separate a significant amount of the drilling fluid components.
- The results from the simulations need to be validated by performing full scale or small scale experiments with a settling tank. The COMSOL model used for the simulations is commonly used for gravitational settling problems, but it is unknown if the model is validated.
- A wider range of particle sizes can be considered in the simulations to obtain more information, which can improve the estimation of the separation efficiency of the separation tank.
- The simulations can be expanded by implementing temperature to study the influence of temperature on the separation efficiency.
- The modelling of the vibrations can be improved by using a vibration source instead of applying the influence through the fluid viscosity. This will result in a more representative simulation, however this will increase the computation time significantly.
- The sludge zone boundary condition in the simulations can be improved to allow resuspension of particles when the flow velocity on the boundary reaches the resuspension creation.

References

- [1] Abdou, M.I., El-Sayed Ahmed, H., (2011), *"Effect of Particle Size of Bentonite on Rheological Behaviour of the Drilling Mud"*, Petroleum Science and Technology.
- [2] American Association of Drilling Engineers (1999), *"Shale Shakers and Drilling Fluid Systems"*, Gulf Professional Publishing.
- [3] American Association of Drilling Engineers, *"Shale shakers and drilling fluid systems"*, Gulf Professional Publishing.
- [4] American Petroleum Institute. (2003), *"Recommended Practice for Field testing Water-based Drilling fluids"*, American Petroleum Institute.
- [5] American Petroleum Institute. (2010), *"API Specification 13A 18th Edition Specification for Drilling Fluids"*, American Petroleum Institute.
- [6] Ansley, R. & Smith, T. (1967), *"Motion of Spherical Particles in a Bingham Plastic"*, AIChE Journal
- [7] ASME Shale Shaker Committee. (2005), *"Drilling Fluids Processing handbook"*, Gulf Professional Publishing.
- [8] Astrakhan, I.M., Gadiev, S.M. (1979), *"Influence of vibrations of non-Newtonian Fluid flow"*, Plenum Publishing Corporation
- [9] Bekkour, K., Leyama, M., Benchabane, A., Scrivener, O. (2005) *"Time-Dependent Rheological Behaviour of Bentonite Suspensions"*, The Society of Rheology, Inc.
- [10] Bird, R.B., Stewart, W.E., Lightfoot, E.N. (2007), *"Transport Phenomena second edition"*, John Wiley & Sons Inc.
- [11] Bouse, E.E., Carrasquero, J.E., Corpoven, S.A. (1992), *"Drilling Mud Solids Control and Waste Management"*, Society of Petroleum Engineers.
- [12] Briscoe, B.J., Luckham, P.F., Ren S.R. (1994), *"The Properties of Drilling Muds at High Pressures and High Temperatures"*, The Royal Society Publishing
- [13] Brown, P.P. and Lawler, D.F. (2003), *"Sphere Drag and Settling Velocity Revisited"*, Journal of Environmental Engineering, ASCE
- [14] Caenn, R., Darley, H.C.H., Gray, G.R. (2011), *"Composition and Properties of Drilling and Completion Fluids, 6th Edition"*, Elsevier Inc.
- [15] Cheng, H., Chao, Z., Ming L., Anchao, W., Fabin, X. (2016), *"Research and Application of Micronized Barite Drilling Fluid in HPHT Wells of the Western South China Sea"*, Science Publishing Group.
- [16] Cheng, N.S. (1997), *"A simplified settling velocity formula for sediment particle"*, Journal of Hydraulic Engineering
- [17] Cheng, N.S. (2008), *"Comparison of formulas for drag coefficient and settling velocity of spherical particles"*, Elsevier Inc.
- [18] Chhabra R.P. (1993), *"Bubbles, drops, and particles in non-newtonian fluids"*, CRC Press, Inc.
- [19] Chhabra, R.P. and Richardson, J.F. (2008), *"Non-Newtonian Flow and Applied Rheology: Engineering Applications"*, Elsevier Inc.
- [20] Coberly, C.J. (1937), *"Selection of Screen Openings for Unconsolidated Sand"*, American Petroleum Institute.
- [21] De Clerck, J., Kers, M., Neve, R., Van de Wouw, Kevin., D'haen, J., Van Langevelde, D., De Rijk, L. (2016), *"Pressurized mud treatment system"*, Huisman Well Equipment
- [22] De Moel, P.J., Verberk, J.Q.J.C., Van Dijk, J.C. (2007), *"Drinking Water: Principles And Practice"*, World Scientific Publishing Company
- [23] Deshpande, N.S., Barigou, M. (2001), *"Vibrational ow of non-Newtonian uids"*, Elsevier Inc.
- [24] Fang, G. (1992), *"An Experimental Study of Free Settling of Cuttings in Newtonian and Non-Newtonian Drilling Fluids: Drag Coefficient and Settling Velocity"*, Society of Petroleum Engineers.
- [25] Fann Instrument Company. (2013), *"Model 35 Vicsometer Instruction Manual"*, Fann Instrument Company.
- [26] Frad, A., Omland, T.H, Saasen, A. (2007), *"Shale Shaker's Effect on Drilling Fluids Rheological Properties"*, Annual Transactions of the Nordic Rheology Society vol 15.
- [27] Health and Safety Executive. (2000), *"Drilling Fluids Composition and use within the UK Offshore Drilling Industry"*, Health and Safety Executiv.
- [28] Holstein, E.D., Lake, L.W. (2007), *"Petroleum engineering handbook Volume V, Reservoir engineering and petrophysics"*, Society of Petroleum Engineers

- [29] Karim, B., Leyama, M., Benchabane, A., Scrivener, O. (2005), "*Time-Dependent Rheological Behaviour of Bentonite Suspensions*", Journal of Rheology
- [30] Krieger, I. M. and Dougherty, T. J. (1959), "*A mechanism for Non-Newtonian Flow in Suspensions of Rigid Spheres*", The Society of Rheology
- [31] Kristensen, A. (2013), "*Flow properties of water-based drilling fluids*", Norwegian University of Science and Technology.
- [32] Lam, C. and Jefferis, S.A. (2014), "*Interpretation of Viscometer Test Results for Polymer Support Fluids*", American Society of Civil Engineers.
- [33] Lapin, S., Matveev, K., Zaeem, M.A. (2010), "*The Effect of Vibration on Flow Rate of Non-Newtonian Fluid*", ResearchGate
- [34] Li, W., Kiser, C., Richard, Q. (2005), "*Development of A Filter Cake Permeability Test Methodology*", American Filtration & Separations Society.
- [35] Lick, W.J. and Huang, H. (2003), "*Resuspension, Flocculation, and Transport of Drilling Muds and Fine-grained Sediments*", Coastal Research Center.
- [36] McCourt, A. and Copeland, R. (2007), "*10 tips to improve drilling fluid performance*", Drilling Contractor.
- [37] Miedema, S.A. and Vlasblom, W.J. (1996), "*Theory for Hopper Sedimentation*", 29th Annual Texas A&M Dredging Seminar
- [38] Nas, S., Torolde, J.S., Wuest, C. (2009), "*Offshore Managed Pressure Drilling Experiences in Asia Pacific*", Society of Petroleum Engineers.
- [39] Rajitha, P., Chhanra, R.P., Sabiri, N.E., Comiti, J. (2005), "*Drag on non-spherical particles in power law non-Newtonian media*", Elsevier Inc.
- [40] Richardson, J.F. & Zaki, W.N. (1954), "*Sedimentation and fluidisation. Part 1*", Trans. Inst. Chem. Eng.
- [41] Richardson, J.F., Mirza, S. (1978), "*Sedimentation of suspension of particles of two or more sizes*", Chemical Engineering Science vol 34.
- [42] Ripperger, S., Gösele, W., Alt, C. (2009), "*Ullmann's Encyclopedia of Industrial Chemistry: Filtration*", John Wiley & Sons.
- [43] Rowe, P. (1987), "*A convenient empirical relation for estimation of the Richardson-Zaki exponent*", Chemical Engineering Science
- [44] Sadat-Helbar, S.M., Amiri-Tokaldany, E., Darby, S., Shafaie, A. (2009), "*Fall Velocity of Sediment Particles*", WSEAS press.
- [45] Saucier, R.J. (1974), "*Considerations in Gravel Pack Design*", Journal of Petroleum technology.
- [46] Schiller, L., and Naumann, A. (1933), "*Über die grundlegenden Berechnungen bei der Schwerkraftaufbereitung*", Zeitschrift des Vereines Deutscher Ingenieure
- [47] Song, T. & Chiew, Y. (1997). "Settling Characteristics of Sediments in Moving Bingham Fluid", Journal of Hydraulic Engineering,
- [48] Tadjarodi, A. and Zabihi, F. (2013), "*Thermal conductivity studies of novel nanofluids based on metallic silver decorated mesoporous silica nanoparticles*", Researchgate.
- [49] Talmon, A.M., Mastbergen, D.R., Huisman, M. (2012), "*Invasion of pressurized clay suspension into granular soil*", Begell House, inc. Publishers.
- [50] Talmon, A.M., van Kesteren W.G.M., Sittoni, L., Hedblom E.P. (2014), "*Shear cell tests for quantification of tailings segregation*", The Canadian journal of chemical engineering.
- [51] Tehrani, A. (2008), "*Thixotropy in Water-Based Drilling Fluids*", Annual Transactions of the Nordic Rheology Society vol 16.
- [52] Van der Walt, J.J., Water, M. (2000), "*To baffle or not to baffle – some baffled solutions*", WISA 2000 Biennial Conference
- [53] Van Rhee, C. (2002), "*On the sedimentation process in a trailing suction hopper dredger*", Delft University of Technology.
- [54] Von Engelhardt, W. (1954), "*Filter cake formation and water losses in deep drilling muds*", Illinois geological survey library.
- [55] Willenbacher, N. and Georgieva, K. (2013), "*Rheology of disperse systems*", Wiley-VCH Verlag GmbH & Co.
- [56] Zhiyao, S., Tingting, W., Fumin, X., Ruijie, L. (2008), "*A simple formula for predicting settling velocity of sediment particles*", Water Science and Engineering.

Appendix A: Additional experiment plots

This appendix contains the consistency and apparent viscosity plots that are created from on the Fann viscosity measurements.

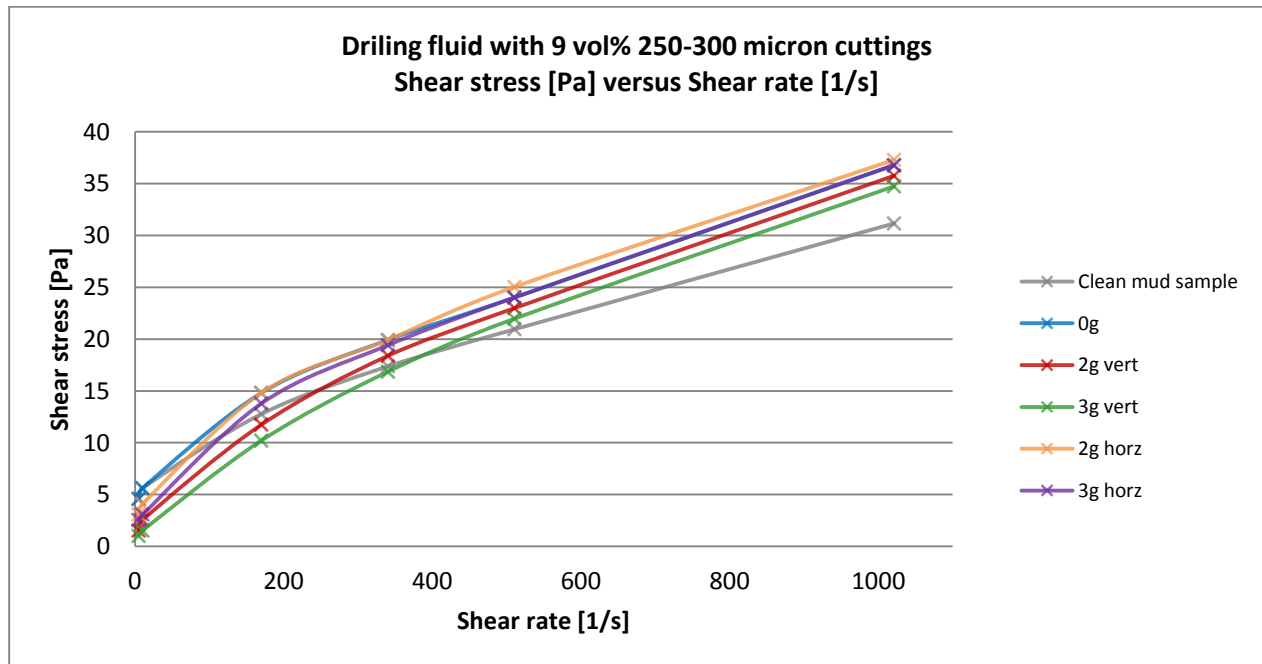


Figure 88: Drilling fluid with 9% 250-300 micron cuttings – consistency curve

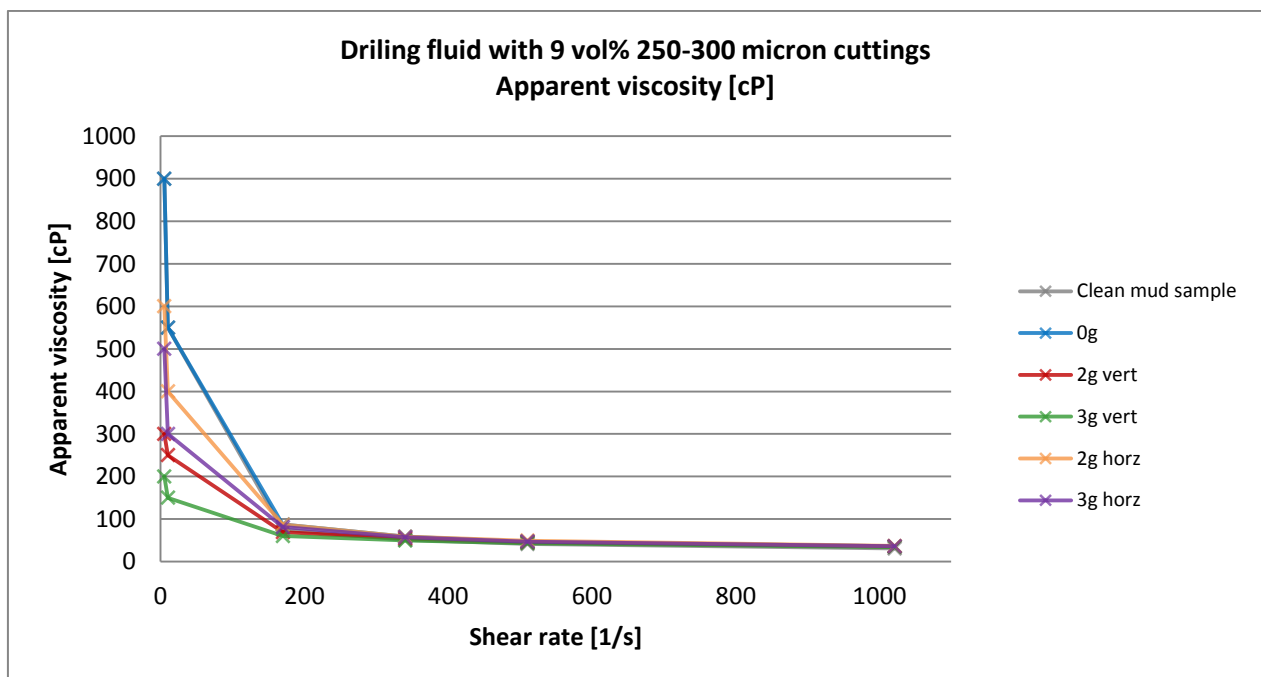


Figure 89: Drilling fluid with 9% 250-300 micron cuttings – Apparent viscosity

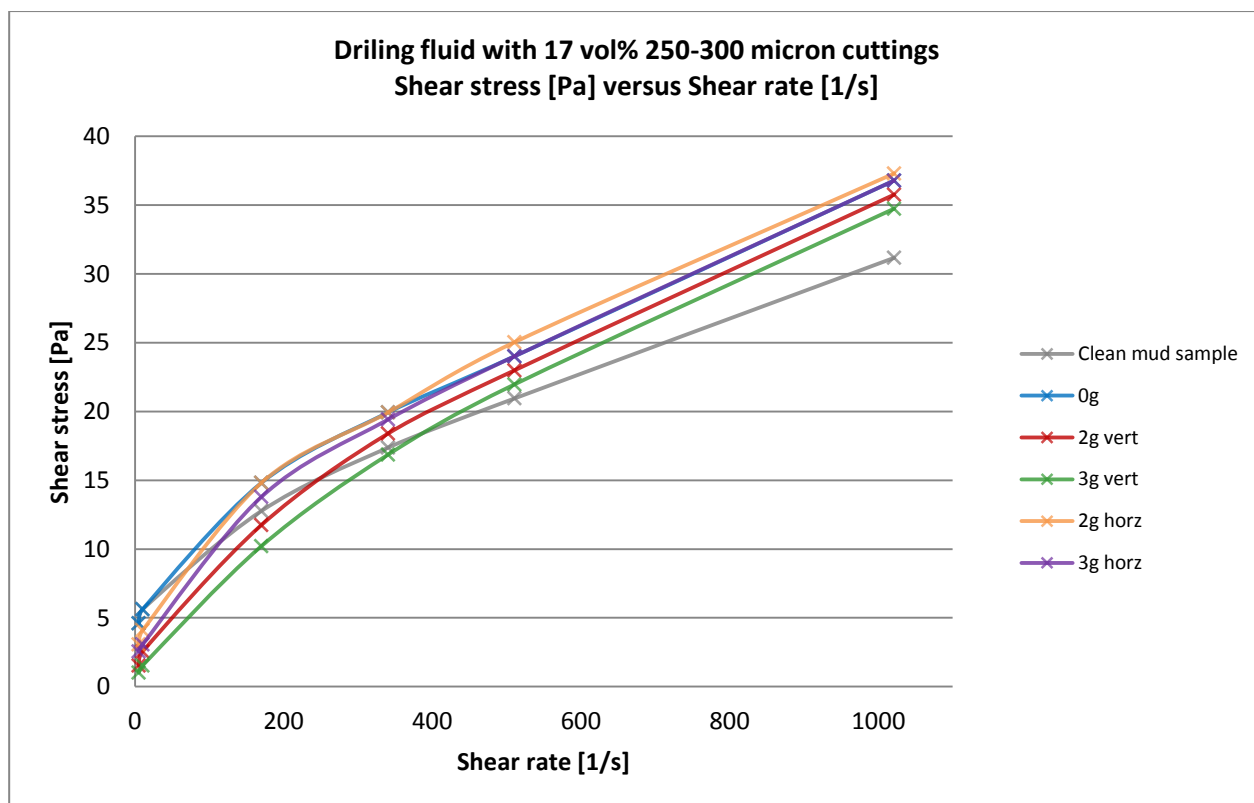


Figure 90: Drilling fluid with 17% 250-300 micron cuttings – consistency curve

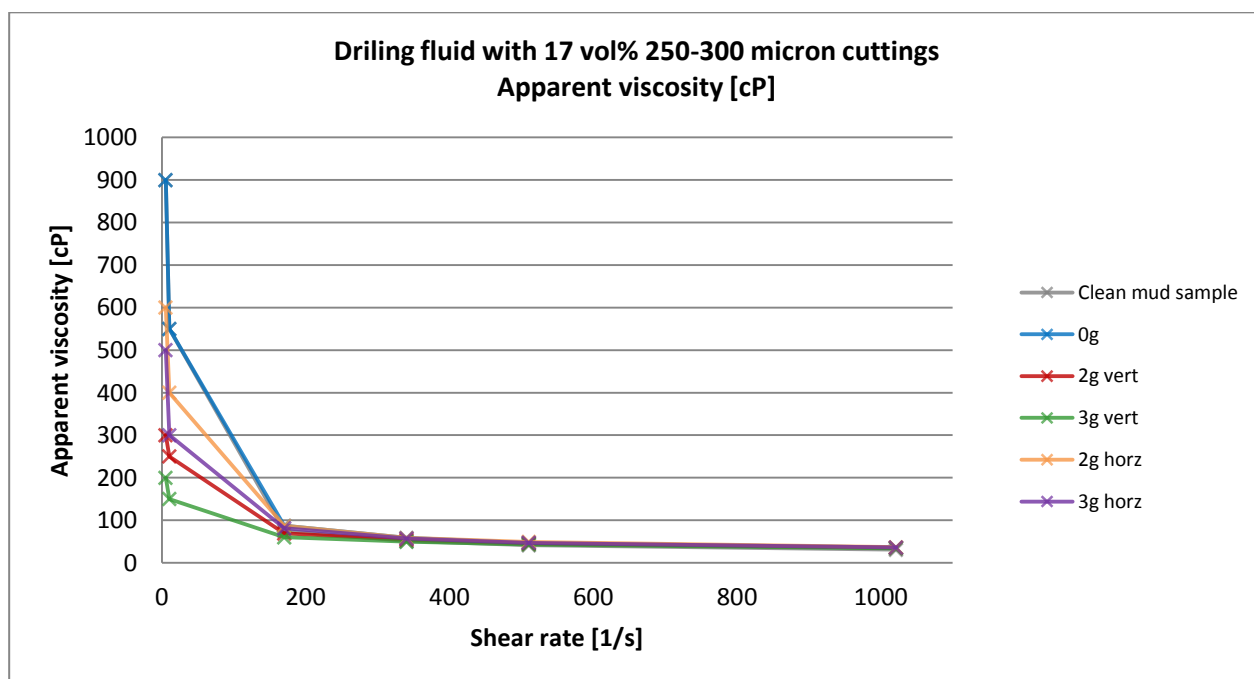


Figure 91: Drilling fluid with 17% 250-300 micron cuttings – Apparent viscosity

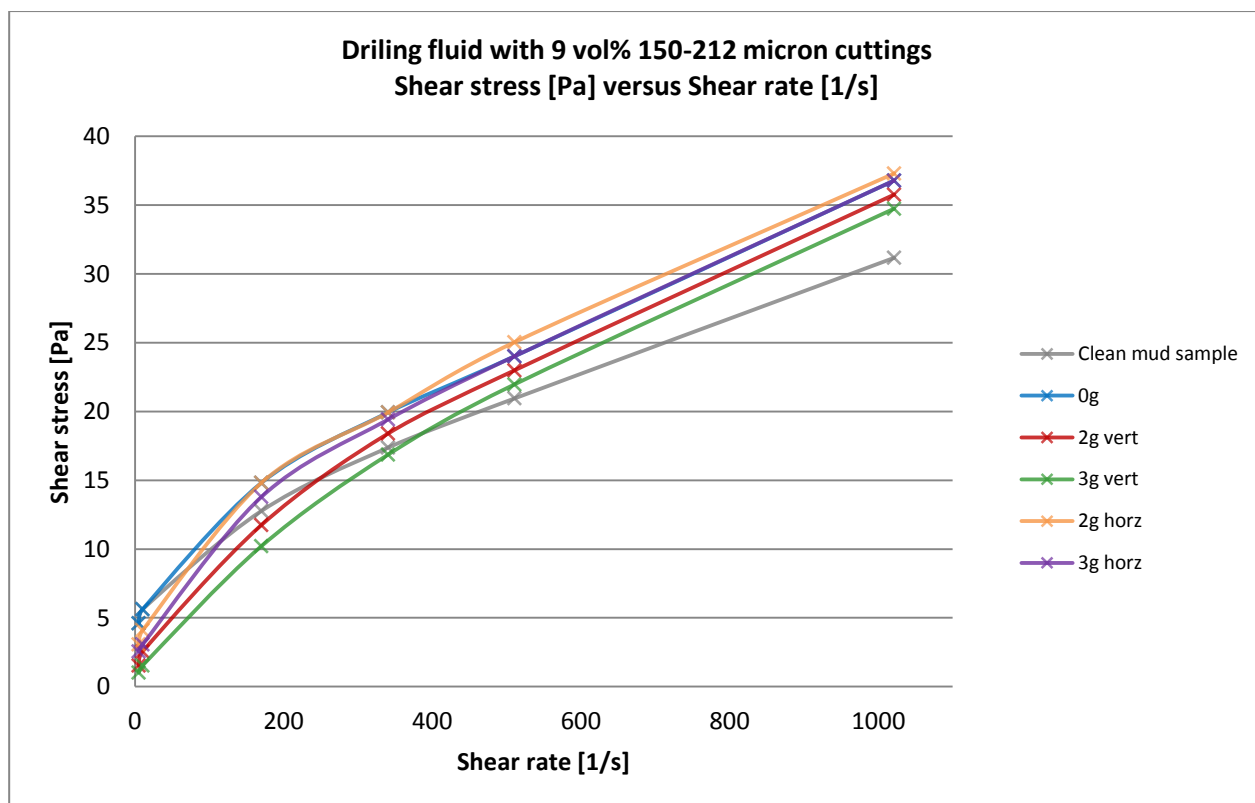


Figure 92: Drilling fluid with 9% 150-212 micron cuttings – consistency curve

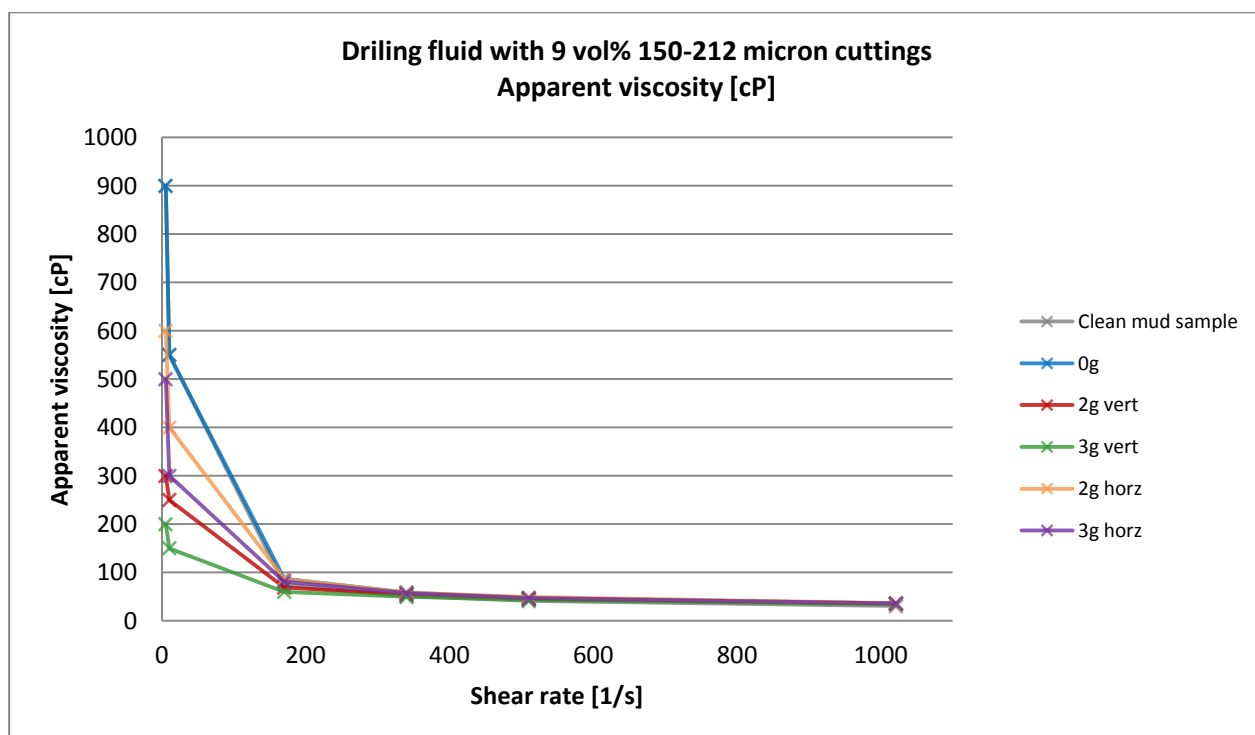


Figure 93: Drilling fluid with 9% 150-212 micron cuttings – Apparent viscosity

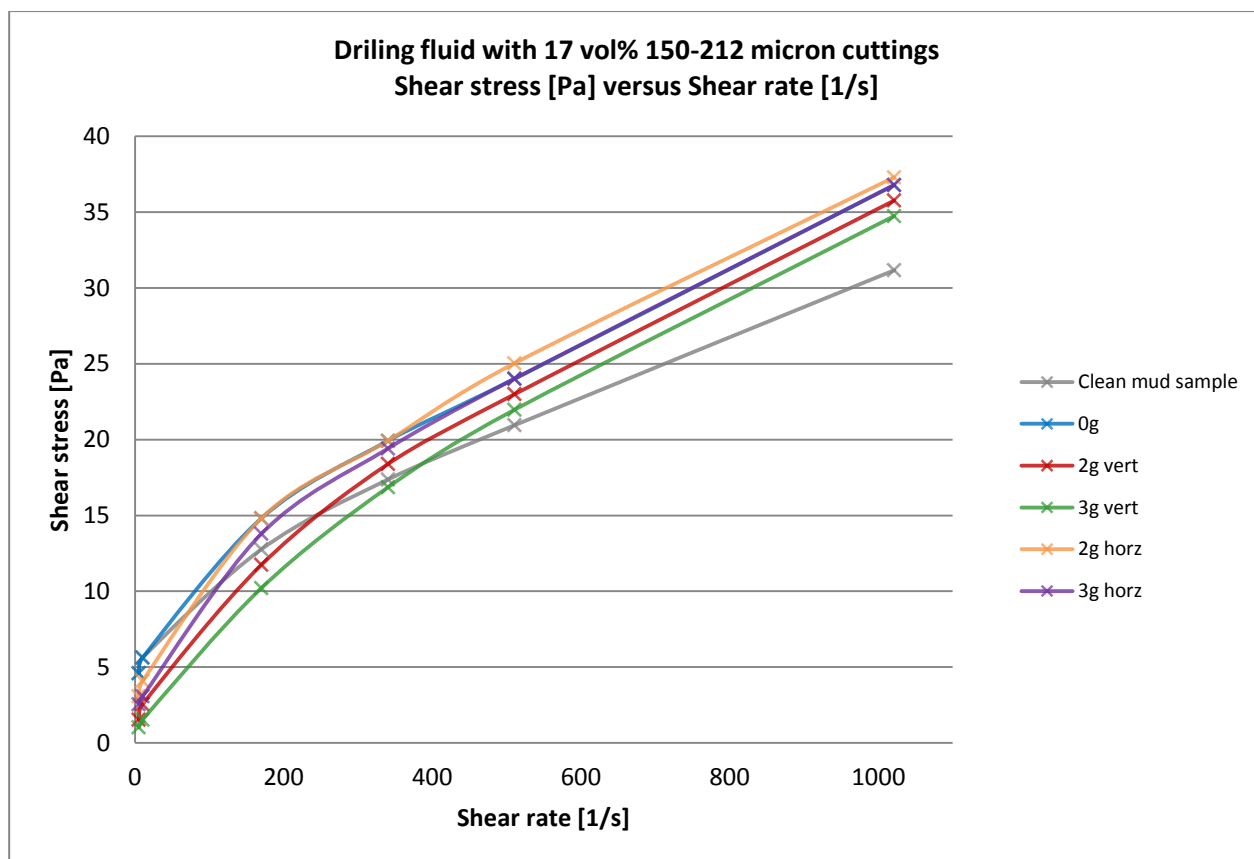


Figure 94: Drilling fluid with 17% 150-212 micron cuttings – consistency curve

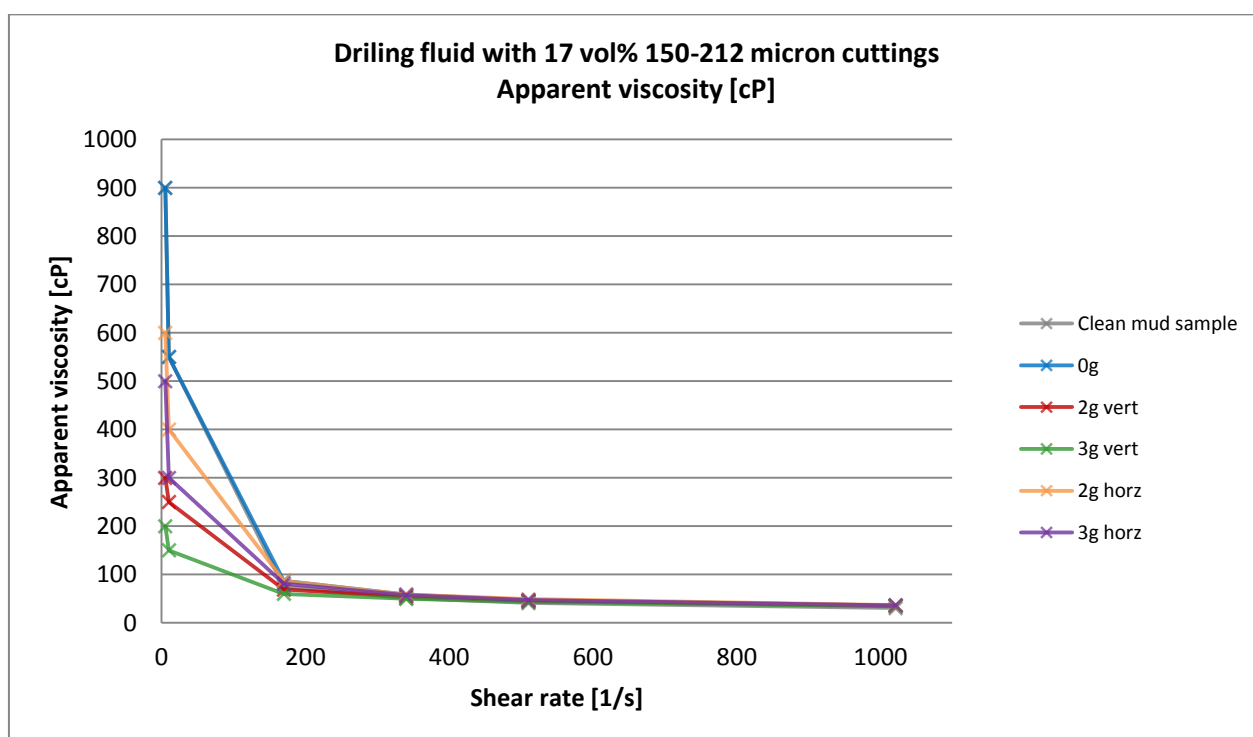


Figure 95: Drilling fluid with 17% 150-212 micron cuttings – Apparent viscosity

Appendix B: Additional simulation plots

This appendix contains additional plots that are obtained from the simulations. For practical reasons only a selected amount of plots are included in the appendix.

B.1. 2D tank designs and results

This section presents a selected set of tank designs that were considered during the 2D simulations. The particle concentration and average particle discharge concentration plots are shown for the case with an inflow rate of 3000 L/min containing 10 vol% particles with diameter of 3mm.

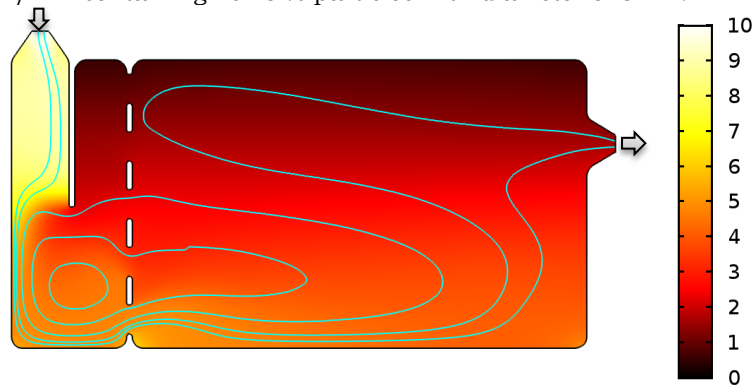


Figure 96: 2D simulation design 1 - Particle concentration [%] and stream lines

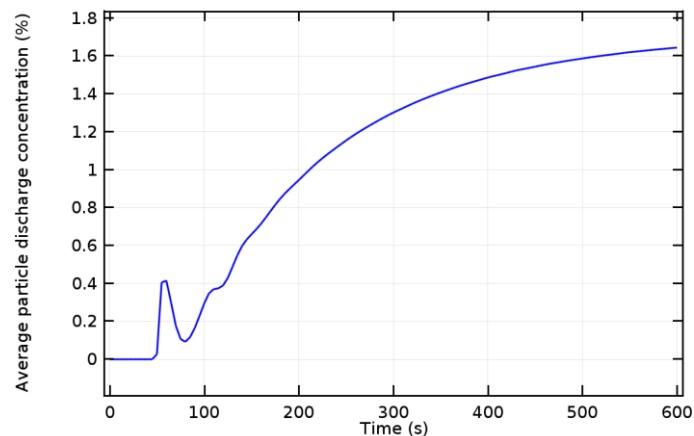


Figure 97: 2D simulation design 1 - Average particle discharge concentration at the outlet [%]

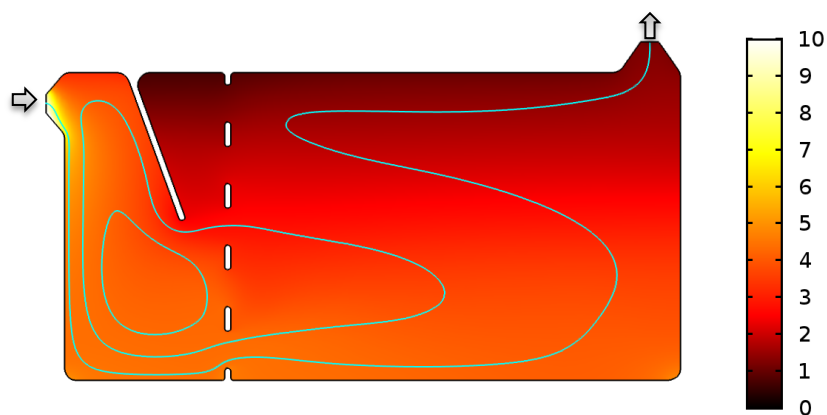


Figure 98: 2D simulation design 2 - Particle concentration [%] and stream lines

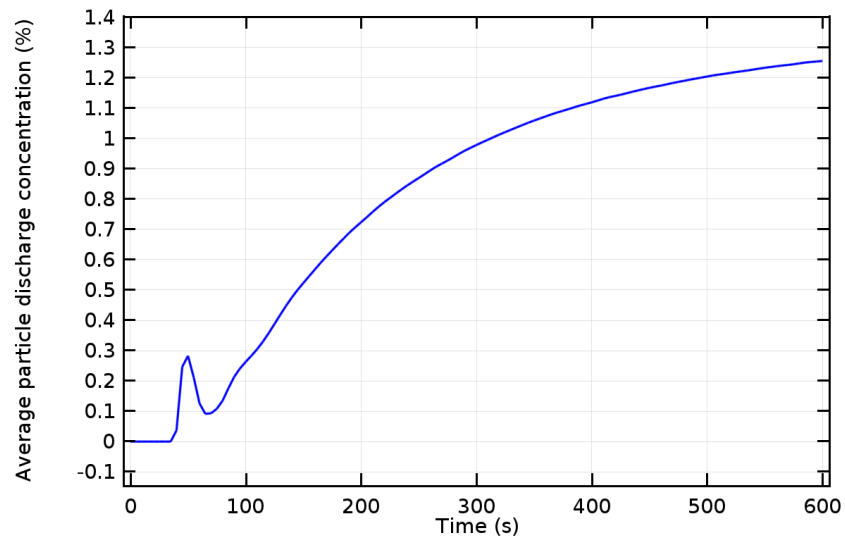


Figure 99: 2D simulation design 2 - Average particle discharge concentration at the outlet [%]

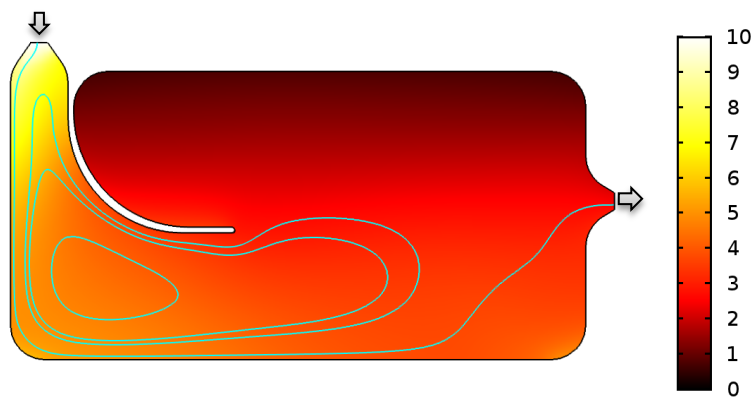


Figure 100: 2D simulation design 3 - Particle concentration [%] and stream lines

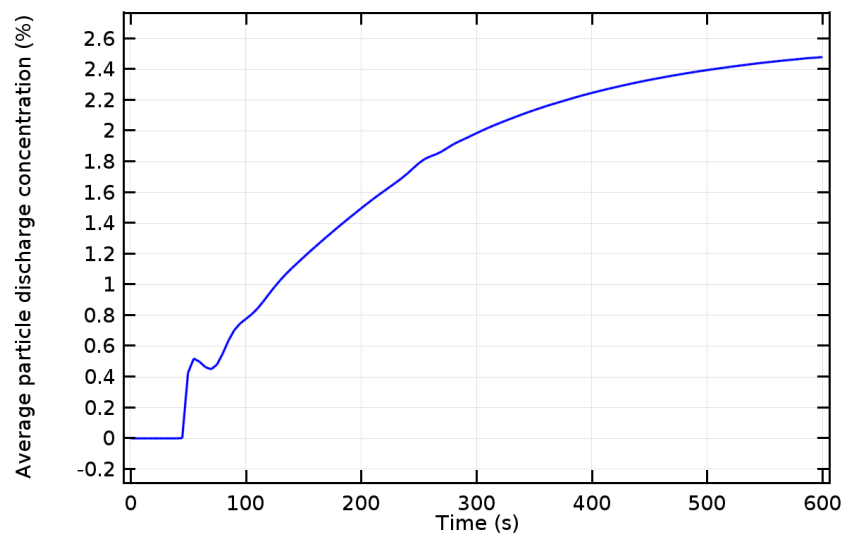


Figure 101: 2D simulation design 3 - Average particle discharge concentration at the outlet [%]

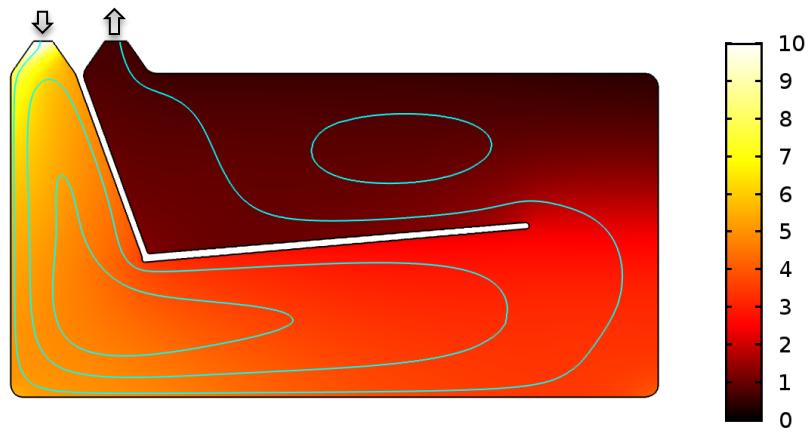


Figure 102: 2D simulation design 4 - Particle concentration [%] and stream lines

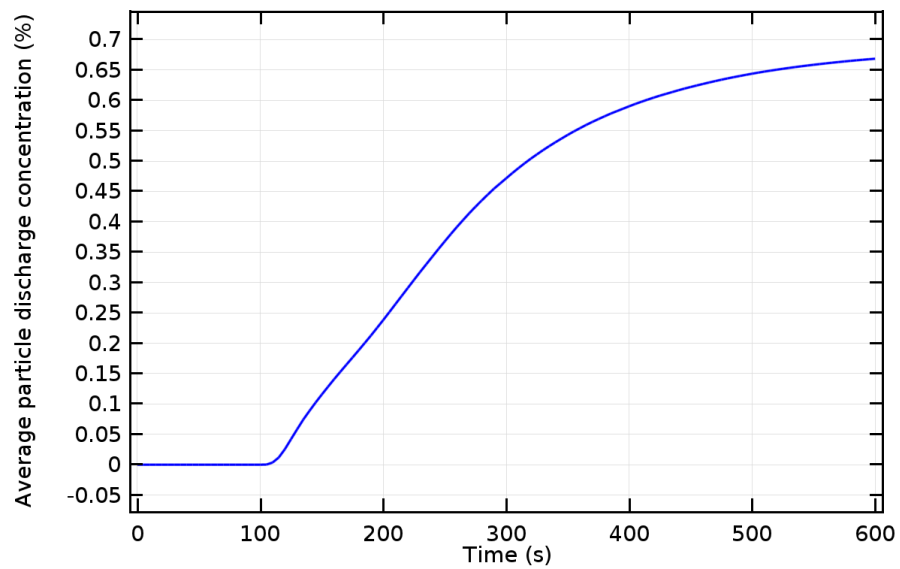


Figure 103: 2D simulation design 4 - Average particle discharge concentration at the outlet [%]

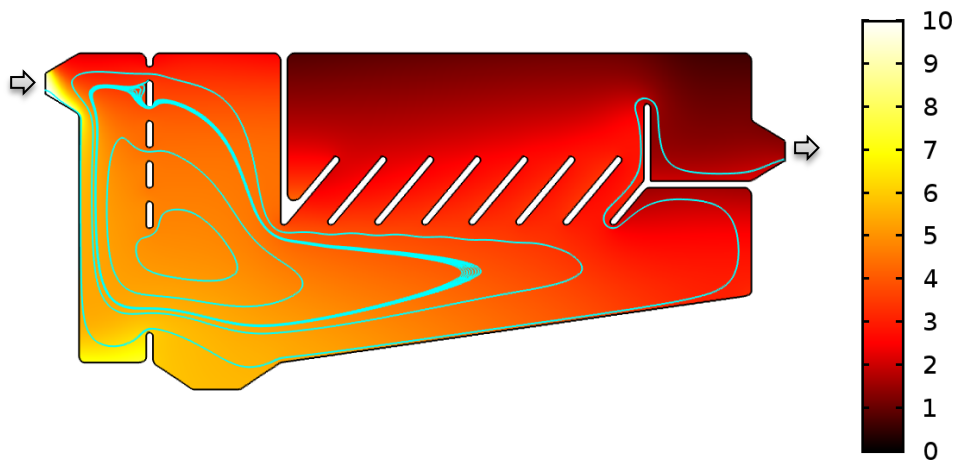


Figure 104: 2D simulation design 5 - Particle concentration [%] and stream lines

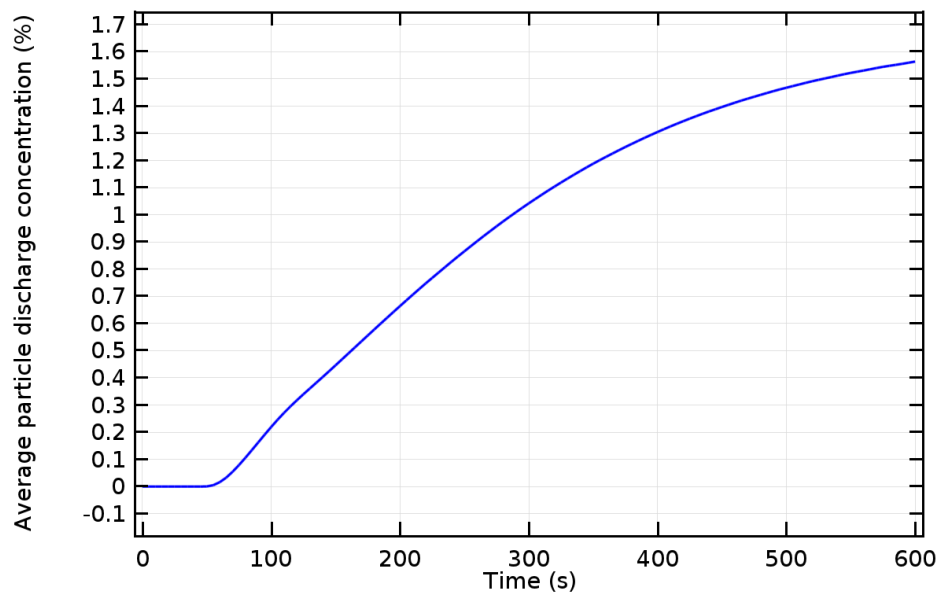


Figure 105: 2D simulation design 5 - Average particle discharge concentration at the outlet [%]



Figure 106: 2D simulation design 6 - Particle concentration [%] and stream lines

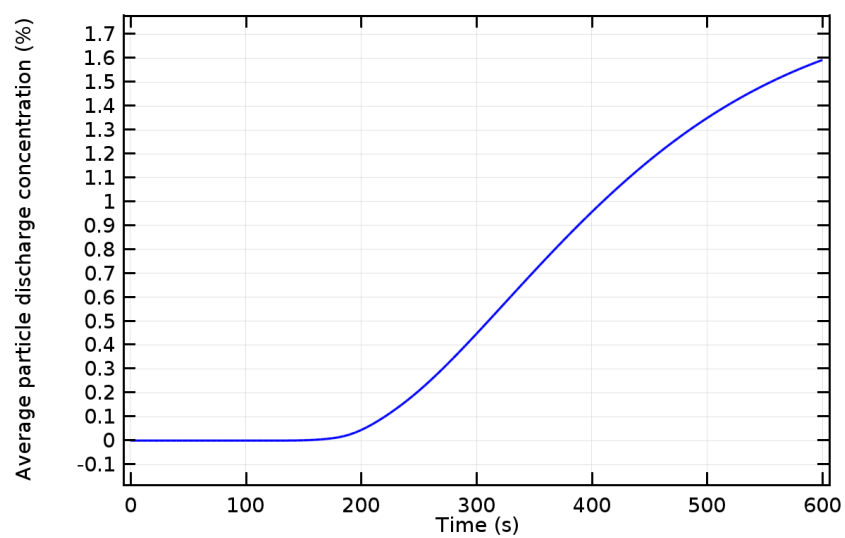


Figure 107: 2D simulation design 6 - Average particle discharge concentration at the outlet [%]

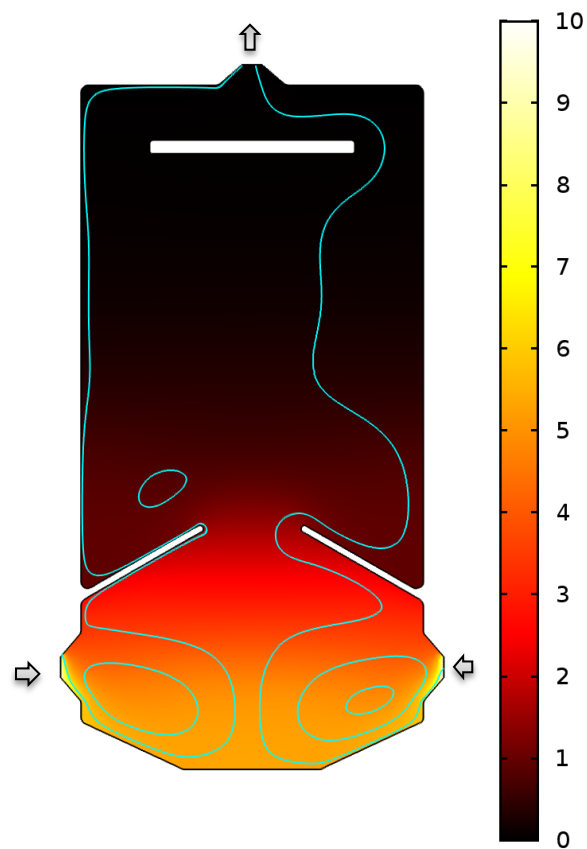


Figure 108: 2D simulation design 7 - Particle concentration [%] and stream lines

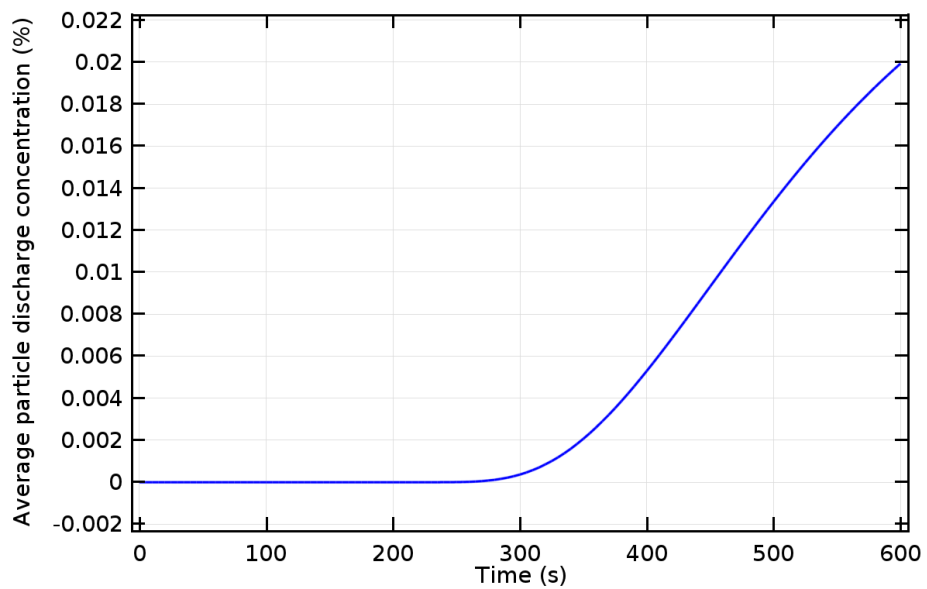


Figure 109: 2D simulation design 7 - Average particle discharge concentration at the outlet [%]

B.2. Sensitivity analysis plots

This section presents two sensitivity studies that were performed to optimize the selected tank design. The first one is used for optimizing the baffle and the second one is used for optimizing the horizontal floor which separates the tank into two layers. The designs and average particle discharge concentration plots are shown for a case with an inflow rate of 3000 L/min containing 10 vol% particles with diameter of 3mm.



Figure 110: 2D simulation baffle sensitivity – Geometry overview

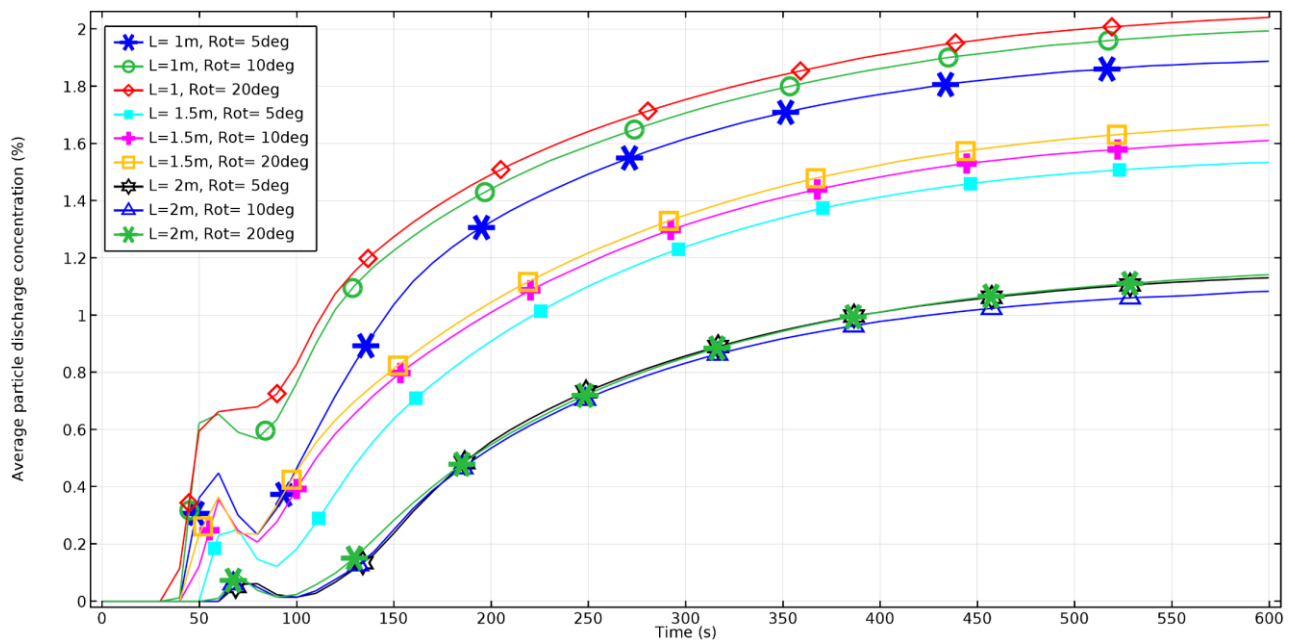
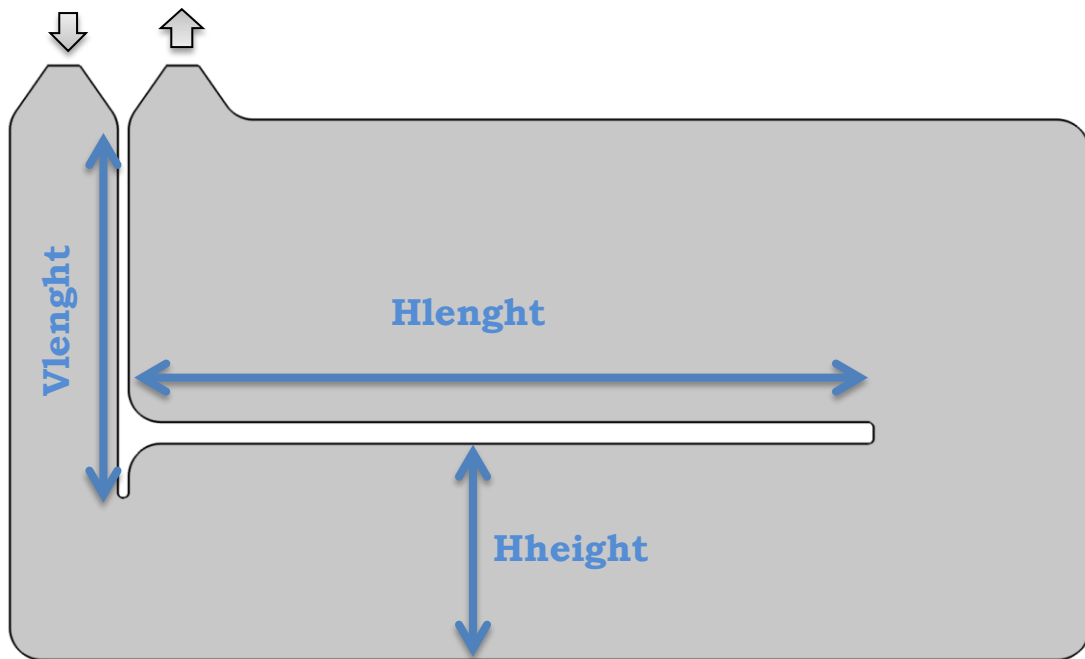
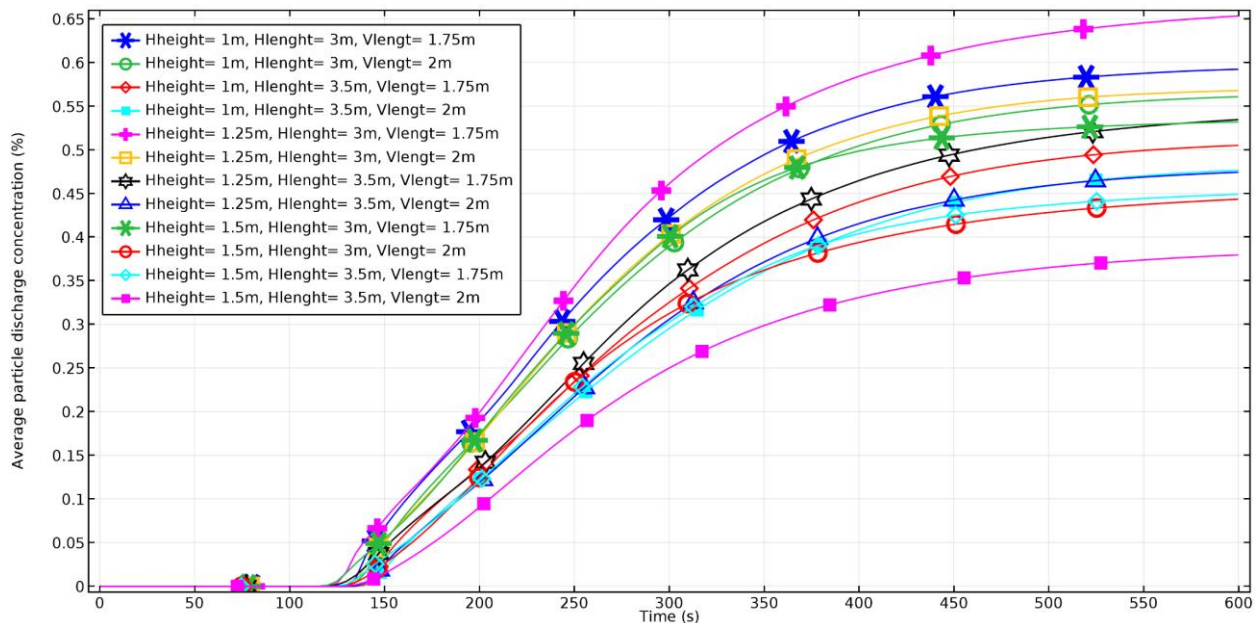


Figure 111: 2D simulation baffle sensitivity – Average particle discharge concentration at the outlet [%]



2D simulation horizontal floor sensitivity – Geometry overview

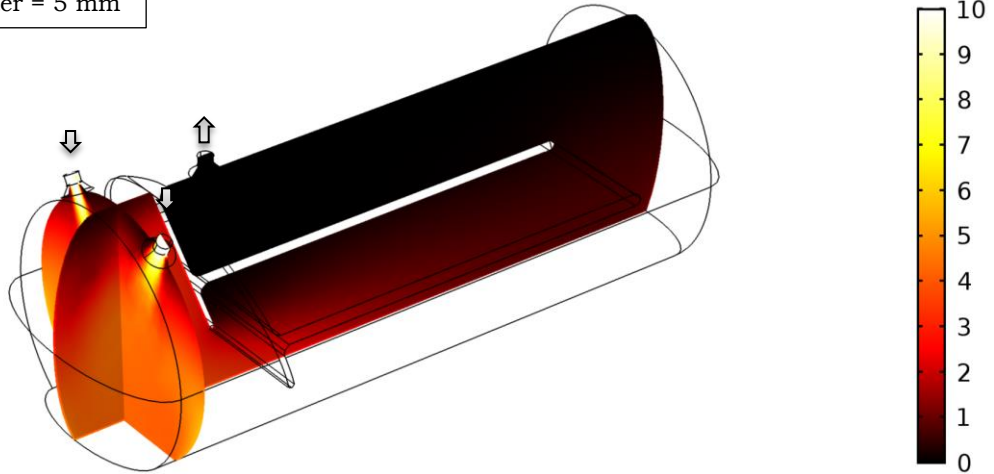


2D simulation horizontal floor sensitivity – Average particle discharge concentration at the outlet [%]

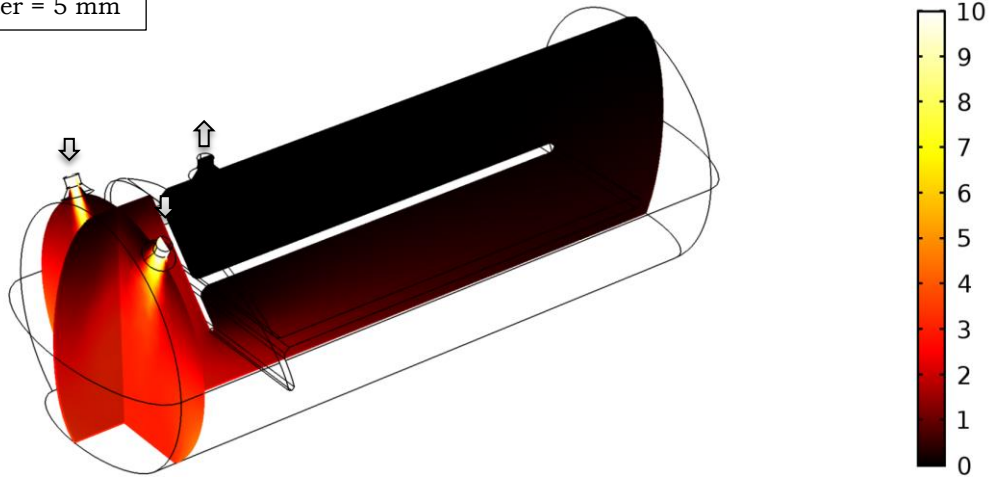
B.3. Additional 3D simulation plots

This section presents additional particle concentration plots that are obtained from the power-law and fixed viscosity 3D simulations. A few of them were already presented in section 5.4.2.2 and 5.4.2.3. The plots represent the particle concentration distribution in the tank after 10 minutes of constant inflow with 10 vol% particles.

Power-law viscosity
Inflow rate = 3000 L/min
Particle diameter = 5 mm



Power-law viscosity
Inflow rate = 2000 L/min
Particle diameter = 5 mm



Power-law viscosity
Inflow rate = 1000 L/min
Particle diameter = 5 mm

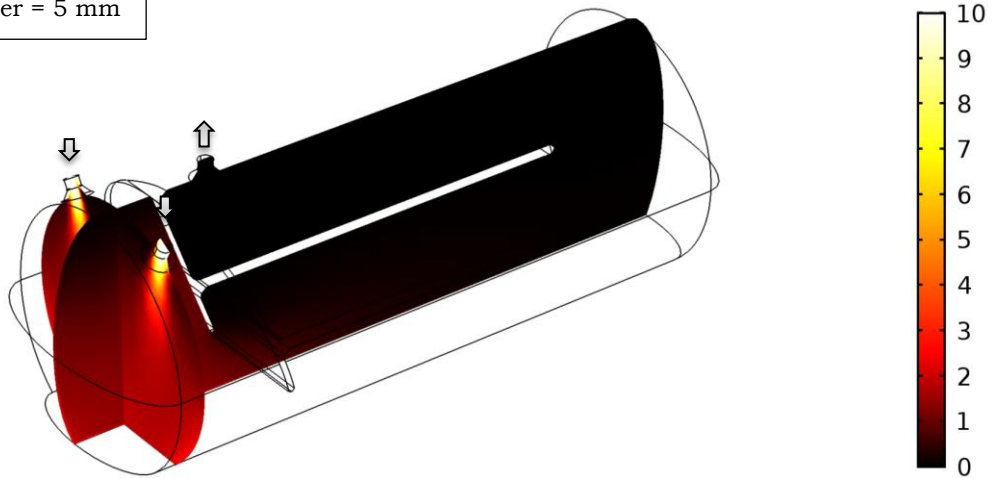
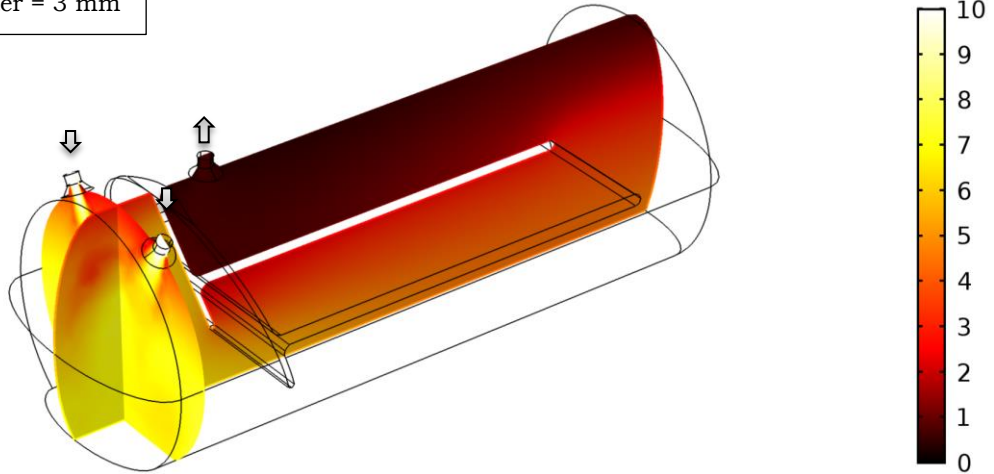
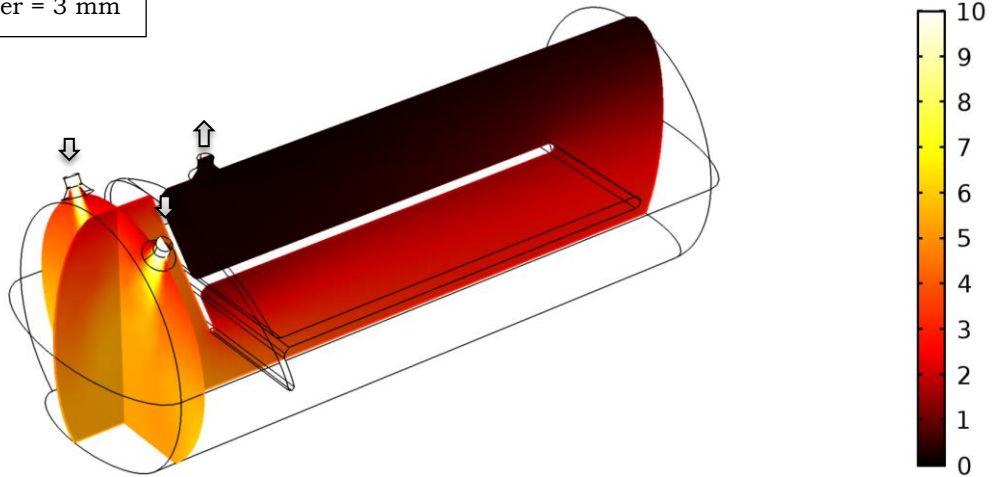


Figure 112: 3D simulation power-law - Particle concentrations [%] for particles of 5 mm

Power-law viscosity
Inflow rate = 3000 L/min
Particle diameter = 3 mm



Power-law viscosity
Inflow rate = 2000 L/min
Particle diameter = 3 mm



Power-law viscosity
Inflow rate = 1000 L/min
Particle diameter = 3 mm

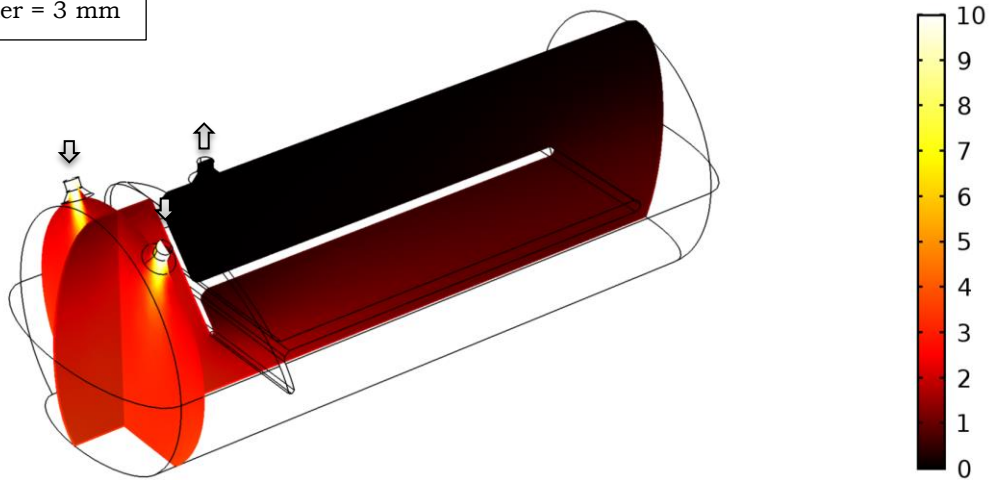
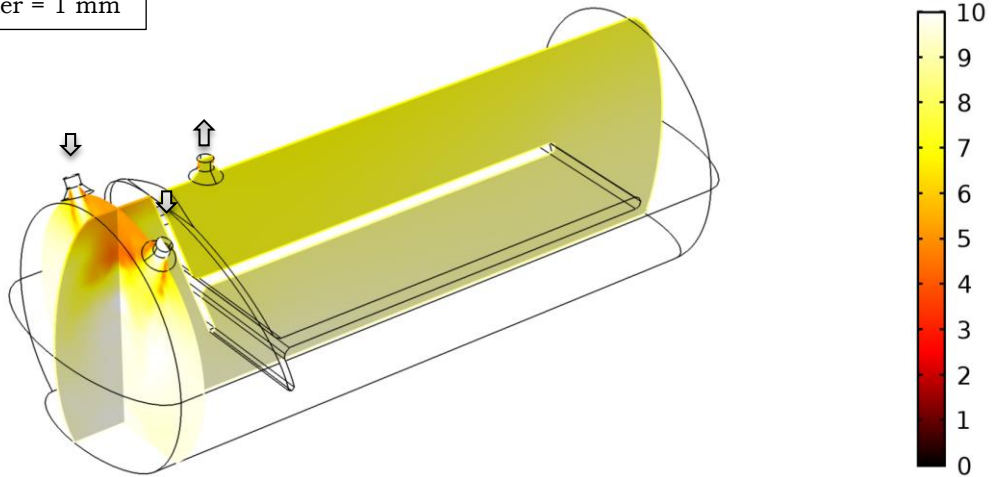
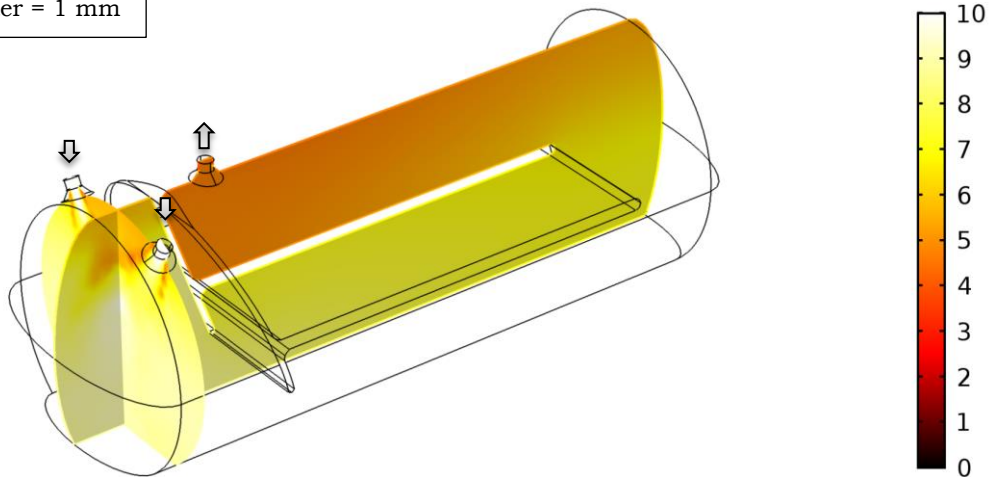


Figure 113: 3D simulation power-law - Particle concentrations [%] for particles of 3 mm

Power-law viscosity
Inflow rate = 3000 L/min
Particle diameter = 1 mm



Power-law viscosity
Inflow rate = 2000 L/min
Particle diameter = 1 mm



Power-law viscosity
Inflow rate = 1000 L/min
Particle diameter = 1 mm

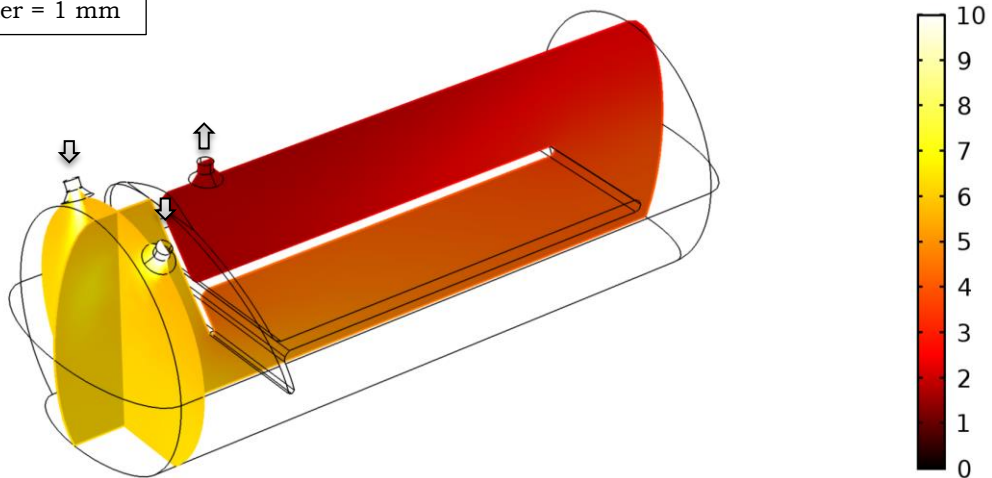
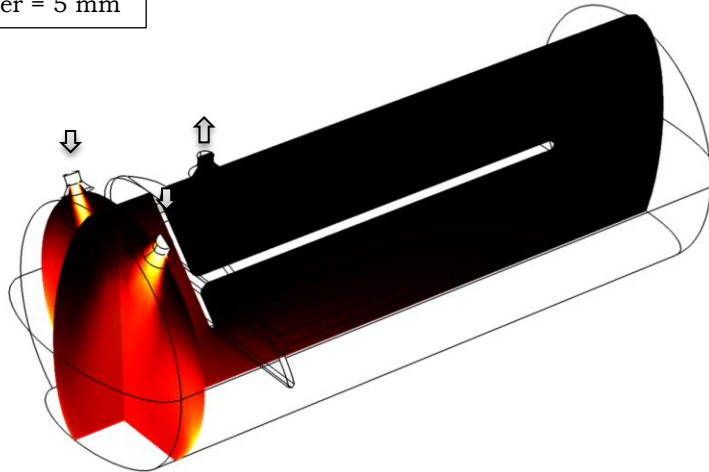
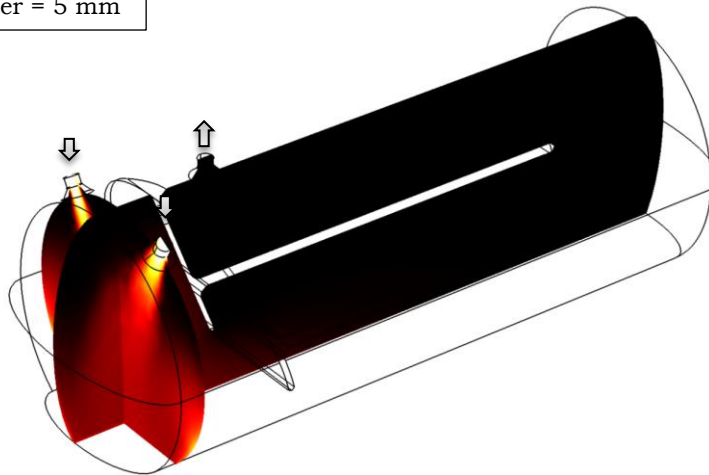


Figure 114: 3D simulation power-law - Particle concentrations [%] for particles of 1 mm

Fixed viscosity ($0.2 \text{ Pa} \cdot \text{s}$)
Inflow rate = 3000 L/min
Particle diameter = 5 mm



Fixed viscosity ($0.2 \text{ Pa} \cdot \text{s}$)
Inflow rate = 2000 L/min
Particle diameter = 5 mm



Fixed viscosity ($0.2 \text{ Pa} \cdot \text{s}$)
Inflow rate = 1000 L/min
Particle diameter = 5 mm

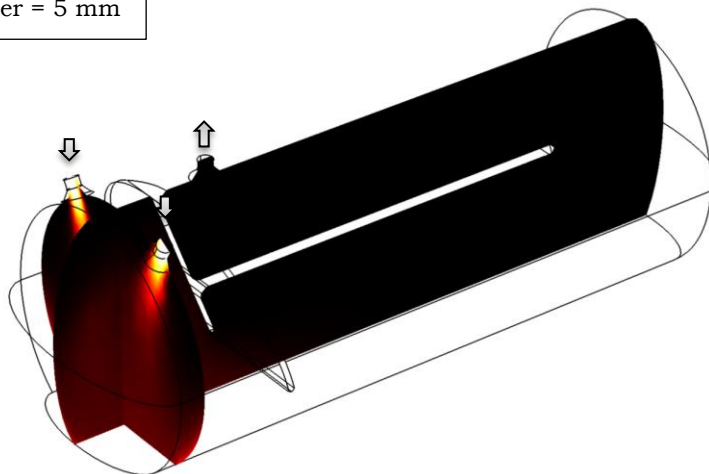
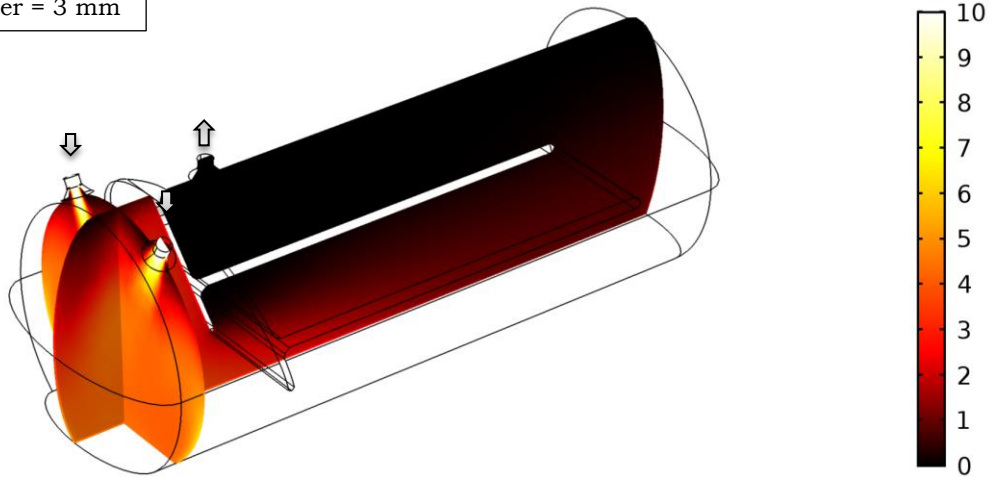
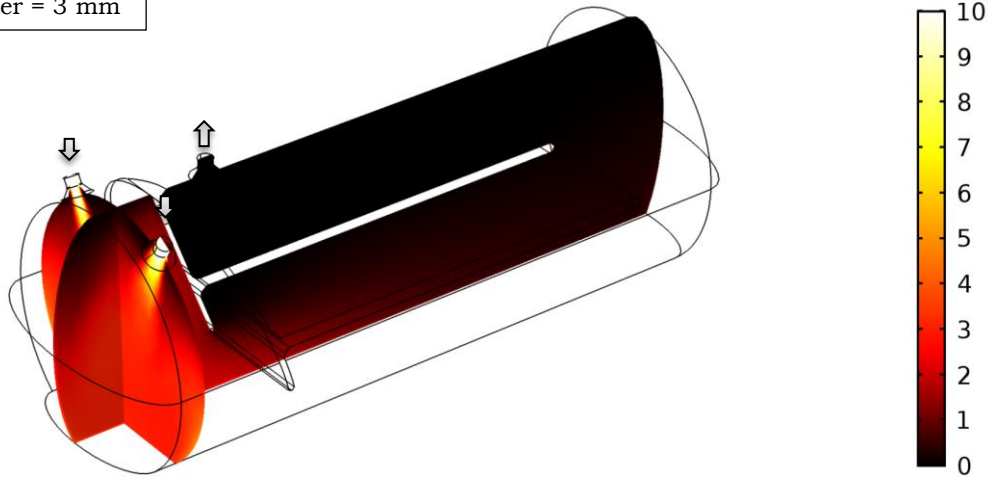


Figure 115: 3D simulation power-law - Particle concentrations [%] for particles of 5 mm

Fixed viscosity ($0.2 \text{ Pa} \cdot \text{s}$)
Inflow rate = 3000 L/min
Particle diameter = 3 mm



Fixed viscosity ($0.2 \text{ Pa} \cdot \text{s}$)
Inflow rate = 2000 L/min
Particle diameter = 3 mm



Fixed viscosity ($0.2 \text{ Pa} \cdot \text{s}$)
Inflow rate = 1000 L/min
Particle diameter = 3 mm

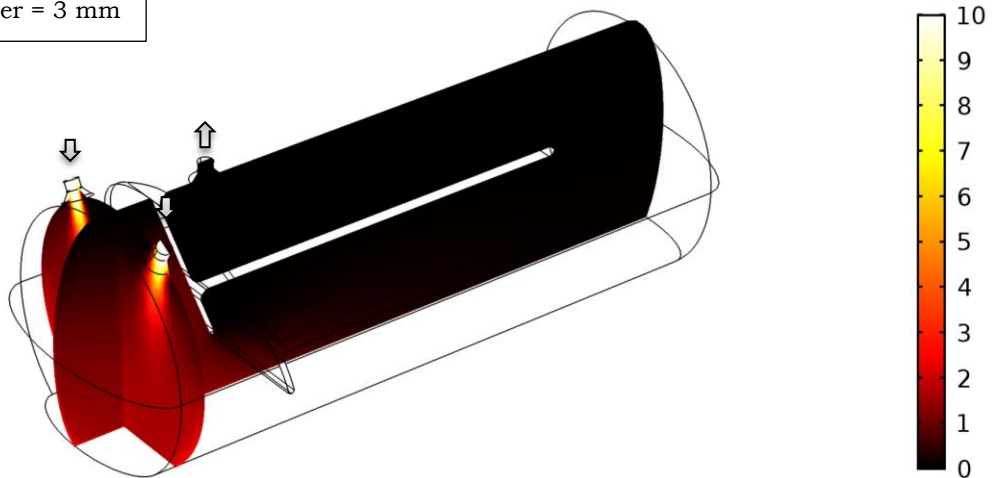
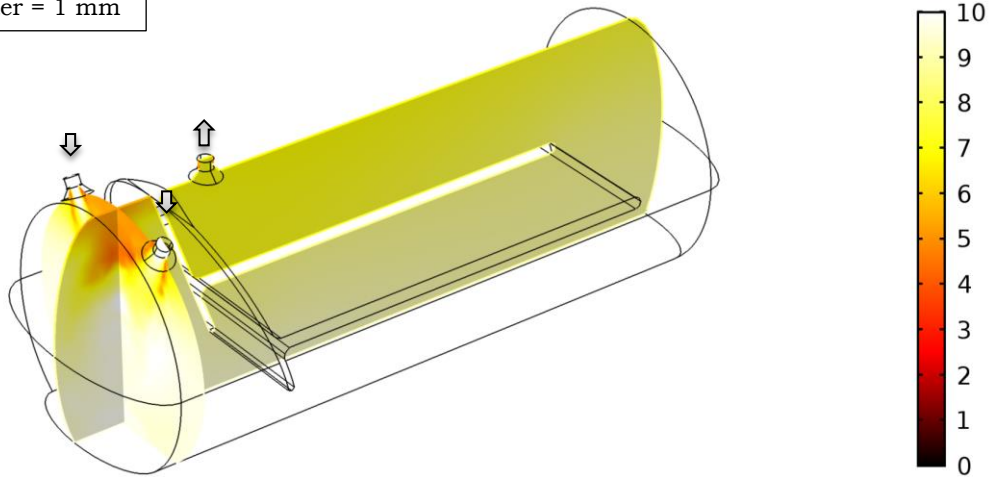
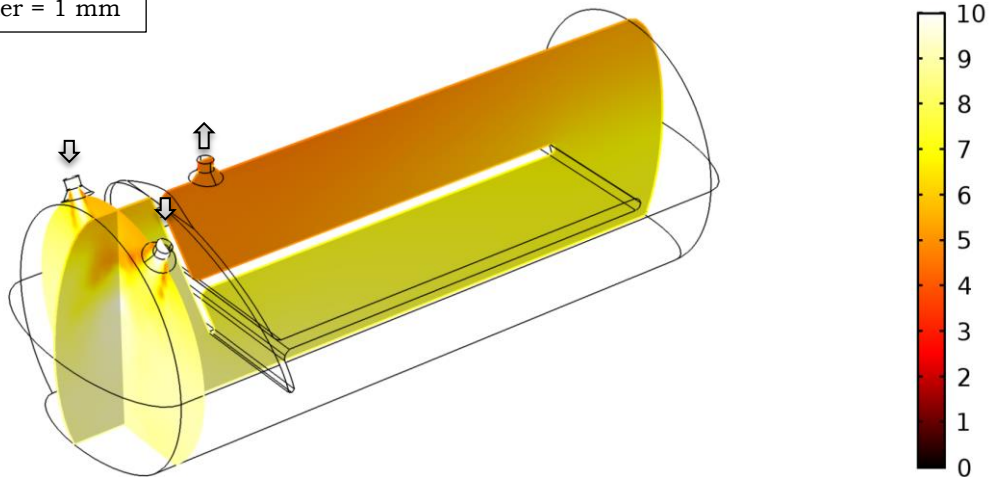


Figure 116: 3D simulation power-law - Particle concentrations [%] for particles of 3 mm

Fixed viscosity ($0.2 \text{ Pa} \cdot \text{s}$)
Inflow rate = 3000 L/min
Particle diameter = 1 mm



Fixed viscosity ($0.2 \text{ Pa} \cdot \text{s}$)
Inflow rate = 2000 L/min
Particle diameter = 1 mm



Fixed viscosity ($0.2 \text{ Pa} \cdot \text{s}$)
Inflow rate = 1000 L/min
Particle diameter = 1 mm

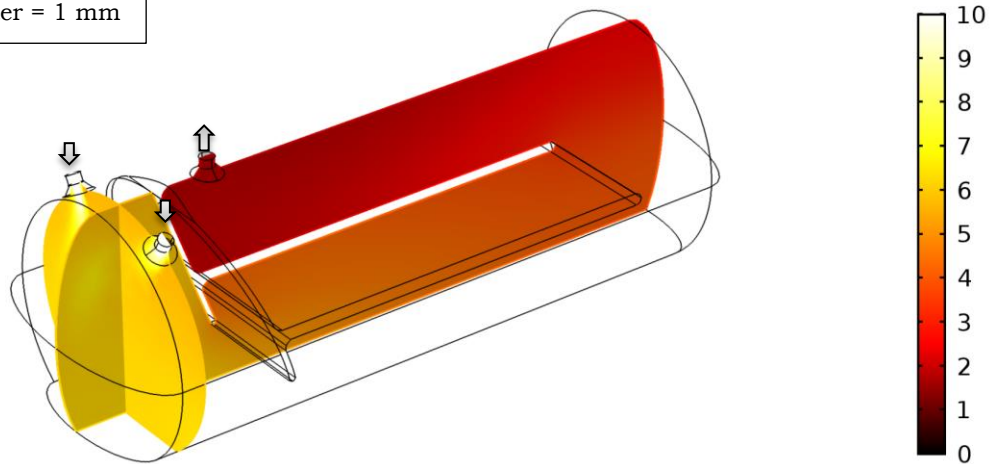


Figure 117: 3D simulation power-law - Particle concentrations [%] for particles of 1 mm

Appendix C: Reference drilling logs

This appendix contains the reference drilling logs that are used to obtain representative drilling fluid parameters.

Casing			Drill String			Bit Information			Pumps			
OD	ID	Shoe MD	OD	ID	Length	Bit Depth			Model	Pump 1	Pump 2	
24 in	22 in	223,7 m	DP	5 in	4,276 in	191,86 m	Bit Size	17,5 in	Liner Size	6,5 in	6,5 in	
			HWDP	5 in	3,25 in	81 m	Type	Tricone	Stroke Length	14 in	14 in	
			Collars	8,25 in	2,5 in	28 m	Model	3 Cone 17 1/2"	Efficiency %	96	96	
			Collars	8,25 in	3 in	18 m	Jets	20, 20, 20, 20	I/str	21,92	21,92	
			Jar	8,25 in	2,81 in	9,4 m	TFA	1,227 in³	SPM	77	78	
			Collars	8,25 in	2,835 in	27 m	Jet Velocity	72 m/s	I/min	1688	1710	
			Collars	9,5 in	3,11 in	18 m	Jet Impact Force	1048 lbf	Circulation			
Open Hole			FIT / LOT			Bit HHSI	0,97 W/m³	B/U Time	22 min	Down Time	1 min	
nominal	actual	Depth MD				Bit Press Drop	31 bar	B/U Strokes	3471	Down Str	131	
17,5 in	18,35 in	400 m				ECD @ Shoe	1,15 SG	AV max	2,84 m/s	Δp Bit	31 bar	
						ECD @ Bit	1,16 SG	AV min	0,24 m/s	Δp Pipe	56 bar	
										Δp Total	101 bar	
Properties			1	2	3	4	Specifications					
Fluid Type	Glycol Drill							Glycodrill				
Sample Source	Rinne							Fluid Treatments				
Time	13:00:00											
Depth	m		418									
Flowline Temp	°C		37									
Mud Weight	SG		1,15 @ 35 °C				1,1 - 1,2					
Funnel Viscosity	sec/qt											
Plastic Viscosity	cP		16 @ 33 °C									
Yield Point	lbf/100 ft²		19				25 - 50					
FANN 600 / 300 rpm	*deflection		51 / 35									
FANN 200 / 100 rpm	*deflection		26 / 19									
FANN 6 / 3 rpm	*deflection		6 / 5									
10 sec / 10 min gel	*deflection		6 / 15									
30 min gel	*deflection											
pH			11									
API Fluid Loss	ml/30min		4,8				< 5					
HTHP Fluid Loss	ml/30min											
HTHP Press / Temp	bar / °C											
Cake API / HTHP	mm		0,4 /									
Pm	ml		1,5									
Pr / Mr	ml		0,4 / 1,2									
Total Hardness	*dH											
Calcium Hardness	mg/l											
Chlorides	mg/l		39000									
Retort Oil / Water	%		0 / 92									
Corr. Water Content	%		95,06									
Corr. Solids Content	%		4,94									
Sand Content	%		0,2									
MBT	kg/m³		28				< 30					
Glykolgehalt	%		3									
KCl (K+)	mg/l		39000									

Casing			Drill String			Bit Information			Pumps					
OD	ID	Shoe MD		OD	ID	Length	Bit Depth	1372 m	Model	Pump 1	Pump 2			
24 in	22 in	223,7 m		5 in	3,228 in	1128,31 m	Bit Size	12,25 in	Liner Size	6,5 in	6,5 in			
13,375 in	12,416 in	1241 m		HWDP 5"	5 in	3 in	45,43 m	Type	Tricone	Stroke Length	14 in	14 in		
			Accelerator	6,5 in	2,75 in	10,04 m	Model	Insert Bit 12 1/4"	Efficiency %	96	96			
			HWDP 5"	5 in	3 in	46,02 m	Jets	20, 20, 20, 15	I/str	21,92	21,92			
			JAR	6,75 in	2,75 in	10 m	TFA	1,093 in³	SPM					
			HWDP 5"	5 in	3 in	81,93 m	Jet Velocity	0 m/s		0	0			
			DC 6 3/4	6,75 in	2,81 in	27,74 m	Jet Impact Force	0 lbf						
Open Hole			FIT / LOT			Circulation								
nominal	actual	Depth MD	FIT				Bit HHSI	0 W/m³	B/U Time	0 min	Down Time	0 min	Tot.Cir Time	0 min
12,25 in	12,55 in	1372 m		1251 m	1,45 SG		Bit Press Drop	0 bar	B/U Strokes	0	Down Str	0	Total Circ Str	0
							ECD @ Shoe	AV max	AV max		Δp Bit	0 bar	Δp Annulus	0 bar
							ECD @ Bit	0 SG	AV min		Δp Pipe	0 bar	Δp Total	0 bar
Properties			1	2	3	4	Specifications							
Fluid Type			Active Mud		Active Mud		Glycodrill							
Sample Source			Flowline		Flowline		Fluid Treatments							
Time			09:30:00		14:30:00		Increase PK 65H concentration to 12,5 kg/m³, and Aluminumsulfate 2 times 10%. Use Shaker 3 as mud cleaner. Dressed to 200 API							
Depth			m		1367		1410							
Flowline Temp			°C		55		63							
Mud Weight			SG		1,16 @ 54 °C		1,14 @ 55 °C		1,1 - 1,2					
Funnel Viscosity			sec/qt											
Plastic Viscosity			cP		22 @ 50 °C		17 @ 50 °C							
Yield Point			lbf/100 ft²		25		24		15 - 25					
FANN 600 / 300 rpm			*deflection		69 / 47		58 / 41							
FANN 200 / 100 rpm			*deflection		38 / 26		37 / 23							
FANN 6 / 3 rpm			*deflection		7 / 6		7 / 5							
10 sec / 10 min gel			*deflection		8 / 22		7 / 18							
30 min gel			*deflection											
pH					9,5		9,5							
API Fluid Loss			ml/30min		3,5		3,8		< 5					
HTHP Fluid Loss			ml/30min											
HTHP Press / Temp			bar / °C											
Cake API / HTHP			mm		0,2 /		0,2 /							
P _m			ml		1		1							
Pr / Mr			ml		0,6 / 1,2		0,7 / 1,4							
Total Hardness			*dH		180		180							
Calcium Hardness			mg/l		1285		1285							
Chlorides			mg/l		38000		37500							
Retort Oil / Water			%		0 / 91		0 / 91,5							
Corr. Water Content			%		93,92		94,4							
Corr. Solids Content			%		6,08		5,6							
Sand Content			%		0,2		0,2							
MBT			kg/m³		49		43		< 30					
Glycol content			%		3,4		3,4		3 - 4					
KCl (K+)			mg/l		39200		38900							
KCl			%		7,14		7,09							

Casing			Drill String			Bit Information			Pumps								
OD	ID	Shoe MD	OD	ID	Length	Bit Depth	860 m	Model	Pump 1	Pump 2							
24 in	23 in	220 m	Drillpipe	5 in	4,276 in	790 m	17,5 in	Liner Size	6,5 in	6,5 in							
			HWDP	5 in	3,031 in	0 m	Type	Tricone	Stroke Length	14 in	14 in						
			Collars 6,75"	6,75 in	2,835 in	0 m	Model	sert Roller Cone	Efficiency %	96	96						
			Collars 8,25"	8,25 in	2,835 in	0 m	Jets	20, 20, 0	I/str	21,92	21,92						
			Accelerator	8,268 in	3,031 in	0 m	TFA	0,614 in³	SPM	75	72						
			Jar	8,268 in	2,992 in	0 m	Jet Velocity	136 m/s	I/min	1644	1579						
			Collars 8,25"	8,25 in	2,874 in	14,33 m	Jet impact Force	1819 lbf	Circulation								
Open Hole			FIT / LOT			Bit HHSI	3,19 W/m²	B/U Time	47 min	Down Time	2 min						
nominal	actual	Depth MD				Bit Press Drop	106 bar	B/U Strokes	6850	Down Str	348						
17,5 in	17,93 in	869 m				ECD @ Shoe	1,11 SG	AV max	0,46 m/s	Ap Bit	106 bar						
						ECD @ Bit	1,11 SG	AV min	0,21 m/s	Ap Pipe	23 bar						
									Ap Total								
									142 bar								
Properties			1	2	3	4	Specifications	Mud System									
Fluid Type			Glycol Drill		Glycol Drill	Glycol Drill											
Sample Source			Flowline		Flowline	Fluid Treatments											
			15:00:00		04:00:00	Added old AMC Drill carb mud to the system for fluid additions Treated with KCl and Glycol for inhibition, Pac ULV for fluid loss. Started to increase KCl concentration to 60 kg/l. Screened up shaker 3 to 4 x API 170. Replaced KCl.											
Flowline Temp			735		855												
Mud Weight			1,09 @ 20 °C		1,11 @ 40 °C							1,04 - 1,15					
Funnel Viscosity			sec/qt														
Plastic Viscosity			cP														
Yield Point			lb/100 ft²									15 - 30					
FANN 600 / 300 rpm			°deflection														
FANN 200 / 100 rpm			°deflection														
FANN 6 / 3 rpm			°deflection														
10 sec / 10 min gel			°deflection														
30 min gel			°deflection														
pH			10		10,1												
API Fluid Loss			ml/30min		4,2							< 5					
HTHP Fluid Loss			ml/30min		4,8												
HTHP Press / Temp			bar / °C														
Cake API / HTHP			mm		0,2 /												
P _n			ml		1												
P _r / M _r			ml		0,6 / 0,7												
Total Hardness			°dH		80												
Calcium Hardness			mg/l														
Chlorides			mg/l		26300												
Retort Oil / Water			%		0 / 95							0 / 94,5					
Corr. Water Content			%		97,14							96,8					
Corr. Solids Content			%		2,86							3,2					
Sand Content			%		0,75							0,75					
MBT			kg/m³		28							28					
Glycol content			%		3,5							3,5					
r ₁ (-)			mg/l		203,92							122,76					
K ₁ (+)			mg/l		27600							30000					
KCl			%		5,1							5,53					
Ca++			mg/l		0							0					
Mg++			mg/l		347,2							347,2					
						0											
						0											
Annulus Hydraulics			1	2	3	4	5	6	7	8	9						
Section length			m	220	570	14,33	29,07	2,44	10,87	2,37	10,92						
Annulus veloc.			m/s	0,21	0,36	0,42	0,46	0,46	0,46	0,46	0,46						
Critical velocity			m/s	1,36	1,4	1,45	1,47	1,47	1,48	1,48	1,47						
Critical rate			l/min	20799	12657	11173	10359	10311	10283	10283	10339						
Re annulus				188	430	513	571	575	577	577	573						
Re lam				2797	2797	2797	2797	2797	2797	2797	2797						
Re turb				3597	3597	3597	3597	3597	3597	3597	3597						
Flow type				lam	lam	lam	lam	lam	lam	lam	lam						
Pressure loss			bar	0,05	0,22	0,01	0,02	0	0,01	0	0,01						
Solids Analysis																	
LGS / HGS			%	2,9 / 0		3,2 / 0											
LGS / HGS			kg/m³	74 / 0		83 / 0											
ASG			SG	3,050		3,380											
Drilled Solids			% / kg/m³	1,8 / 46		2,1 / 55											
Brine SG			SG	1,032		1,035											
Bent EQ			% / kg/m³	1,1 / 28		1,1 / 28											
Volume Increase Factor																	
Drilling Parameters			Directional Survey														
Surf RPM			61 rpm	Flow Rate	3223 l/min	Survey MD	826 m										
Torque			0,61 kN-m	SPP	145 bar	Survey TVD	821,8 m										
WOB			1,5 MT	avg ROP	9,31 m/hr	Inclination	18,13 °										
max. DH Temp			49 °C			Azimuth	274,1 °										
						Horiz. Displ.											
Solids Control Equipment																	
Shaker			Hrs.	Screens													
1- VSM 300			15	20	20	20	45	45	100	100							
2- VSM 300			15	20	20	30	45	45	100	100							
3- VSM 300			15	20	20	20	170	170	170	170							
Centrifuge			Hrs.	Other Equipment													
Centrifuge 1			15	Desander													
Centrifuge 2			15	Desilter													
Flockstation			15														


Casing			Drill String			Bit Information			Pumps										
OD	ID	Shoe MD	OD	ID	Length	Bit Depth		Model	Pump 1	Pump 2									
24 in	23 in	207 m	DP	5 in	3,23 in	870,29 m	1135 m	Liner Size	6,5 in	6,5 in									
13,625 in	12,415 in	825,6 m	HWDP	5 in	3 in	195,03 m	12,25 in	Stroke Length	14 in	14 in									
			String Stabilizer	12,2 in	2,8 in	2,45 m	Type	PDC	96	96									
			DC	8,25 in	2,8 in	27,9 m	Model	MDSIS16	21,92	21,92									
			Roller Reamer	12,25 in	2,8 in	1,97 m	Jets	13, 13, 13, 13, 13, 13, 13	70	67									
			Short NMDC	8 in	3,23 in	11,03 m	TFA	0,907 in³	1535	1469									
			Tools	8,636 in	2,797 in	26,33 m	Jet Velocity	86 m/s											
							Jet Impact Force	1116 lbf											
Open Hole			FIT / LOT			Circulation													
nominal	actual	Depth MD	FIT			Bit HHSI	2,51 W/m²	B/U Time	25 min	Down Time	2 min	Tot.Cir Time	60 min						
12,25 in	12,85 in	1135 m		835 m	1,5 SG	Bit Press Drop	44 bar	B/U Strokes	3382	Down Str	264	Total Circ Str	8252						
						ECD @ Shoe	1,17 SG	AV max	6,58 m/s	Δp Bit	44 bar	Δp Annulus	6,71 bar						
						ECD @ Bit	0 SG	AV min	0,71 m/s	Δp Pipe	167 bar	Δp Total	230 bar						
Properties		1	2	3	4	Specifications		Mud System											
Fluid Type		Active Mud	Active Mud	Active Mud	Active Mud	Glycoldrill													
Sample Source		Rinne	Rinne	Rinne	Rinne	Fluid Treatments													
Time		02:30:00	12:00:00	16:00:00	21:00:00	SCE continuously in use in flocc mode. Activ system is Treated wiht Glycol and Pac ULV.													
Depth	m	1027	1070	1086	1123														
Flowline Temp	°C	49	53	53	53														
Mud Weight	SG	1,16 @ 45 °C	1,16 @ 50 °C	1,16 @ 51 °C	1,16 @ 50 °C														
Funnel Viscosity	sec/qt																		
Plastic Viscosity	cP	19 @ 45 °C	19 @ 50 °C	18 @ 50 °C	17 @ 50 °C														
Yield Point	lb/100 ft²	23	21	23	23														
FANN 600 / 300 rpm	*deflection	61 / 42	59 / 40	59 / 41	57 / 40														
FANN 200 / 100 rpm	*deflection	35 / 25	34 / 25	35 / 25	33 / 23														
FANN 6 / 3 rpm	*deflection	7 / 5	7 / 5	7 / 5	6 / 4														
10 sec / 10 min gel	*deflection	6 / 16	6 / 14	6 / 15	6 / 14														
30 min gel	*deflection																		
pH		10,4	10,2	10,2	9														
API Fluid Loss	ml/30min	3	3,2	3,8	4														
HTHP Fluid Loss	ml/30min																		
HTHP Press / Temp	psi / °C																		
Cake API / HTHP	mm	0,1 /	0,1 /	0,1 /	0,1 /														
P _n	ml	2,5	2,2	2,2	2														
P _r / M _r	ml	0,4 / 0,8	0,2 / 0,7	0,1 / 0,7	0,2 / 0,6														
Total Hardness	*dH	100	110	110	110														
Calcium Hardness	mg/l	714	714	714	714														
Chlorides	mg/l	62125	62125	63900	63900														
Retort Oil / Water	%	0 / 90	0 / 90	0 / 90	0 / 88														
Corr. Water Content	%	94,41	94,43	94,5	92,48														
Corr. Solids Content	%	5,59	5,57	5,5	7,52														
Sand Content	%	0,2	0,2	0,2	0,2														
MBT	kg/m³	35,75	35,75	35,75	35,75														
Glykolgehalt	%	3,4	3,2	3,2	3,2														
KCl (K+)	mg/l	46000	46950	45800	48800														
KCl	%	8,16	8,33	8,11	8,64														
Annulus Hydraulics		1	2	3	4	5	6	7	8	9	Drilling Parameters		Directional Survey						
Section length	m	825,6	44,69	195,03	2,45	27,9	1,97	11,03	9,67	1,75	Surf RPM	110 rpm	FlowRate	3004 l/min	Survey MD	1114 m			
Annulus veloc.	m/s	0,77	0,71	0,71	6,09	1,02	6,58	0,98	0,8	0,98	Torque	8000 N-m	SPP	122 bar	Survey TVD	1048,24 m			
Critical velocity	m/s	0,74	0,7	0,7	8,48	1,19	9,19	1,13	0,86	1,13	WOB	6,6 t	avg ROP	5,42 m/Std	Inclination	42,47 °			
Critical rate	l/min	2890	2960	2960	4184	3518	4192	3476	3219	3476	max. DH Temp				Azimuth	32,8 °			
Re annulus		4559	4451	4451	3149	3744	3143	3790	4092	3790	Horiz. Displ.					253,39 m			
Re lam		2100	2100	2100	2100	2100	2100	2100	2100	2100	Solids Control Equipment								
Re turb		2900	2900	2900	2900	2900	2900	2900	2900	2900	Shaker		Hrs.		Screens				
Flow type	turb	turb	turb	turb	turb	turb	turb	turb	turb	turb	1- VSM 300	18	20	20	30	120	120	140	140
Pressure loss	bar	0,45	0,02	0,09	1,09	0,05	1,11	0,02	0,01	0	2- VSM 300	24	20	20	20	100	100	120	120
											3- VSM 300	24	30	40	40	170	170	170	170
Solids Analysis		1	2	3	4	5	6	7	8	9	Centrifuge		Hrs.		Other Equipment		Hrs.		
LGS / HGS	%	5,6 / 0	5,6 / 0	5,6 / 0	5,5 / 0	7,5 / 0					Centrifuge 1	24	Desander	6					
LGS / HGS	kg/m³	145 / 0	145 / 0	145 / 0	143 / 0	196 / 0					Centrifuge 2	24	Desilter	24					
ASG	SG	2,600	2,610	2,600	2,180						Flockstation								
Drilled Solids	% / kg/m³	4,2 / 110	4,2 / 109	4,2 / 109	4,1 / 107	6,1 / 160													
Brine SG	SG	1,075	1,075	1,075	1,076	1,077													
Bent EQ	% / kg/m³	1,4 / 36	1,4 / 36	1,4 / 36	1,4 / 36	1,4 / 36													
Volume Increase Factor		1,05	1,05	1,05	1,05	1,05													

Appendix D: Drilling fluid component data sheets

This Appendix contains the technical data sheets of the drilling fluid components that are used for the preparation of the test samples.

D.1. Cebo-gel Wyoming API bentonite

PRODUCT
DATA



Cebo Wyoming API

Use
For the production of drilling fluid for use in oil- and gas well drilling and in horizontal directional drilling.

For optimal efficiency the **mixing water** of the slurry should have the following properties:
Conductivity : $\leq 1000 \mu\text{S/cm}$
pH : 4.5 - 9

Description
The basis for Cebo Wyoming API is a high-quality natural sodium bentonite from Wyoming (U.S.A.). A characteristic is the low YP/PV ratio.

Typical values

Parameter	Method	Required	Typical Value
600 Reading at 64 gram/litre	API 13A-section 9	30 min.	35
Dry sieve analysis through 150 μm	OCMA DFCP-4	98% min.	99 %
YP/PV ratio	API 13A-section 9	3 max.	2
Wet sieve analysis	API 13A-section 9	4% max.	3 %
Filtrate volume	API 13A-section 9	15 ml. max.	13 ml

Chemical and physical properties

Composition	High-quality natural sodium bentonite
Colour	Grey beige
Form	Soft powder

Cebo Holland BV
Westerduinweg 1
NL-1976 BV IJMUJIDEN
P.O. Box 70
NL-1970 AB IJMUJIDEN
The Netherlands

Tel.: +31-255-546262
info@cebo.com
www.cebo.com

In so far as we can ascertain the above-stated information is correct. However, we are unable to provide any guarantees with regard to the results that you will achieve with this. This specification is provided on the condition that you determine yourself to what degree it is suitable for your purposes.

Page 1 of 2

PRODUCT DATA



Cebo Holland

Slurry properties

Cebo Wyoming API mixed with distilled water in various concentrations.

Parameter	Method	40 kg/m ³	50 kg/m ³	60 kg/m ³	70 kg/m ³
Liquid limit ball number	Kugelharpengerät DIN 4126	1	3	4	6
Density	Mud balance	1.03 g/ml	1.03 g/ml	1.04 g/ml	1.04 g/ml
Filtrate water loss	DIN 4127	9.0 ml	7.5 ml	6.5 ml	5.5 ml
Marsh funnel API	API RP 13B 2 (1 litre outflow)	35.5	38	44	55

Packaging

- 1000 kg packed in 25 kg bags on a pallet with shrink film

Cebo Holland BV
Westerduinweg 1
NL-1976 BV IJMUJIDEN
P.O. Box 70
NL-1970 AB IJMUJIDEN
The Netherlands

Tel.: +31-255-546262
info@cebo.com
www.cebo.com

Revision date :04.01.2016
Document nr :WY01IP

In so far as we can ascertain the above-stated information is correct. However, we are unable to provide any guarantees with regard to the results that you will achieve with this. This specification is provided on the condition that you determine yourself to what degree it is suitable for your purposes.

Page 2 of 2

D.2. Xanthan gum

SHANGHAI TRUSTIN CHEMICAL CO., LTD.
RM 2001, NO.58, CHANGLIU ROAD, PUDONG NEW
AREA, SHANGHAI CITY, CHINA 200135

Technical Data Sheet

PRODUCT NAME:	XANTHAN GUM
CAS NO.:	11138-66-2
PACKING:	25KG kraft paper bags

Description of the Product

Xanthan Gum, which is mainly made from starch and can easily dissolve in water, is a high molecular weight polysaccharide produced by fermentation with *Xanthomonas Campestris* under the conditions of special nutrient medium, PH, O₂-supply and temperature, then purified, dried and milled into white-like or light-yellow free-flowing powder.

The main compositions of Xanthan Gum are D-glucopyranose, D-mannose and D-glucuronic acid. The molecular structure of Xanthan Gum is as below.

1. Outstanding viscosity-enhancing property and solubility in water.
2. Unique pseudo-plasticity rheological property of xanthan gum makes it high-efficient emulsifier and stabilizer.
3. Excellent stability to large of temperature and PH change.
4. Satisfying compatibility with acid, alkaline, brine, enzyme, surface active agent, antiseptic, oxidant and other thickener.
5. Perfect synergistic action when compounding with guar gum, locust bean gum and other gums.

Technological Index

Project Indicators	Industrial Grade
Appearance	Cream-white powder
Particle size(mesh)	40 Mesh
Loss on drying %	≤15
Ashes %	≤13
Viscosity(1% KCL,cps)	>1200
Shearing Ratio	≥6.0
PH (1% solution)	6.0 - 8.0
Halotolerance(speed 3)	≥12.5

Features:

- . Without clotting when put in water.
- . High viscosity when low shearing.
- . Low viscosity when high shearing.
- . Non-thixotropy.
- . It is compatible to high concentration electrolyte, e.g. salt. Surface active agents of

SHANGHAI TRUSTIN CHEMICAL CO., LTD.
RM 2001, NO.58, CHANGLIU ROAD, PUDONG NEW
AREA, SHANGHAI CITY, CHINA 200135

the anionic.

- . Stability in different pH conditions.
- . Stable performance at high temperature.
- . Stable in high viscosity operation
- . Even use the relative low-speed rotors, it is easy dissolved.
- . Control fluid flow on the bevel and vertical plane.
- . Prevent phase segregation of suspension liquid and emulsion.
- . Ensure that the free liquidity of the product shelf life.
- . Enhance the stability of the foam.

Application:

Xanthan Gum can be widely used in more than twenty fields, such as food, pharmaceutical, fine chemical, agriculture, oil drilling and exploitation, and so on. Comparing with other kinds of gum, xanthan gum has many advantages.

Acting as thickener and stabilizer, industrial grade Xanthan Gum can be applied to many industrial fields, such as oil drilling, pesticide, pottery & porcelain, printing & dyeing, paint, paper-making, mine-extraction, and so on.

It is specially produced as mud additive for oil drilling. Being an environment friendly and high efficiency mud additive, it has an excellent tolerance to a wide range of temperature, PH and salinity. It can extremely increase the mud penetration rate and suspension ability to the drilling-cuttings. Meanwhile, it can also reduce the pressure loss during drilling, stabilize the well-bore, prevent the damage to oil formation, and improve the efficiency of drilling, work-over and completion.

Package:

25kg kraft paper bag

Storage:

Stock in dry, ventilated, moisture-proof, sunlight-proof place.

D.3. M6 Silverbond quartz flour (barite replacer)

SilverBond®
KWARTSMEEL

KENMERKEN EN VOORDELEN

DESSEL, BELGIE

SILVERBOND® kwartsmeel wordt geproduceerd uit zuivere kwartsgrondstoffen.

Het wordt gebruikt in toepassingen die minerale vulstoffen behoeven die mechanisch performant zijn, chemisch van hoge zuiverheid en niet reactief.

SILVERBOND® is inert, heeft een neutrale pH, en zal geen chemisch reactie ondergaan of initiëren in gekatalyseerde of meer-component systemen. Evenmin zal SILVERBOND® degraderen in extreme temperaturen of omstandigheden. SILVERBOND® biedt formulators een laag specifiek oppervlak en olieabsorptie, zodat een hoge vulgraad kan behaald worden in verven en cementgebaseerde systemen, en een hoge stijfheid in elastomeren en epoxy-formuleringen.

SILVERBOND® is chemisch zuiver en fungeert als excellente isolator in elektrische en elektronische componenten, en als stabiele vulstof in thermische isolatie.

Het SILVERBOND® gamma wordt geproduceerd volgens ISO-standaarden of interne kwaliteitsprogramma's.

Het resultaat is een chemische zuiverheid en een consistent uniforme korrelgrootteverdeling voor voorspelbare prestatie, ondersteund door betrouwbare dienstverlening.

KORRELVERDELING EN FYSISCH EIGENSCHAPPEN

Gemiddelde waarden. Deze geven geen specificatie weer.

		↓				
		M6	M10	M300		Methode
controlezeef	> 63 µm	14	2		%	Alpine
	> 40 µm			1,8		
D10		5	4	3	µm	Malvern MS2000
D50		30	23	17	µm	Malvern MS2000
D90		95	60	40	µm	Malvern MS2000
soortelijk gewicht		2,65	2,65	2,65	kg/dm ³	
stortgewicht		1	0,9	0,85	kg/dm ³	
specifieke oppervlakte		0,8	0,9	0,9	m ² /g	BET
		2450	3600	4000	cm ² /g	Blaine
olieabsorptie		16,5	17,5	19	g/100 g	
hardheid		7	7	7	Mohs	
pH		7	7	7		
gloeiverlies		0,12	0,12	0,12	%	
kleur	L*	90	91	92		Minolta CM-3610d
	a*	0,87	0,74	0,62		D65/10°
	b*	4,13	3,57	3,09		
lichtbrekingsindex		1,55	1,55	1,55		

Technical Data

CHEMISCHE SAMENSTELLING (XRF) %

Gemiddelde waarden. Deze geven geen specificatie weer.



	M6	M10	M300
SiO ₂	99,5	99,5	99,5
Fe ₂ O ₃	0,03	0,03	0,03
Al ₂ O ₃	0,20	0,20	0,20
TiO ₂	0,03	0,03	0,03
K ₂ O	0,04	0,04	0,05
CaO	0,02	0,02	0,02



SIBELCO
BENELUX

Contacteer ons vrijblijvend voor verdere informatie.

www.sibelco.be

Bovenvermelde informatie is gebaseerd op gemiddelde waarden. De typische eigenschappen en chemische analyses zijn bedoeld als voorbeelden en kunnen niet beschouwd worden als vervanging voor eigen testen en onderzoek in alle omstandigheden waarbij eigenschappen en chemische samenstellingen kritische factoren zijn.

Verkoop en levering geschieden steeds volgens onze algemene verkoopsvoorwaarden.

Veiligheidsinformatieblad op verzoek • TDS.03.05.50 • 2009-10-01 • ed.01

CAS-Nr.: 14808-60-7
EINECS-Nr.: 238-878-4

De Zate 1, BE-2480 DESSEL, Belgium
Tel: +32 14 83 72 11 Fax: +32 14 83 72 12 email: sales@sibelco.be

D.4. Sieved M32 fine sand (cuttings replacer)

SILICA SAND OF MOL M31 - M32 - M34

Technical Data

After mining, the silica sands of Mol - M31, M32 and M34 - are industrially processed: sieved, washed and classified. These qualities are available moist or dried; by truck, wagon or ship; in bulk or bagged (dried sands).

The silica sands of Mol are an excellent raw material for the glass-, crystal- and ceramic industry, for foundries, for tile glues, plasters, mortars, coatings etc...

GRANULOMETRIC DATA AND PHYSICAL CHARACTERISTICS

Method : ISO-sieving



	M31	M32	M34	
D50	370	260	170	µm
AFS	45	50	75	
> 1000 µm	1			%
> 710 µm	5			%
> 500 µm	25			%
> 355 µm	53	7		%
> 250 µm	85	57	3	%
> 180 µm	98	93	30	%
> 125 µm			91	%
< 63 µm	traces	≤ 0.1	≤ 0.3	%
density	2.65	2.65	2.65	kg/dm ³
bulk density	1.6	1.5	1.4	kg/dm ³
hardness	7	7	7	Mohs
pH	7	7	7	
loss on ignition	0.15	0.15	0.15	%
colour	L* 70 a* 2.63 b* 9.58	70 2.79 9.82	72 1.93 7.76	Minolta CM-3610 D65/10°

TDS.03.05.10 2010-12-09 1/2

Sibelco Benelux
De Zate 1 - BE-2480 Dessel
tel. +32 14 83 72 11 - fax +32 14 83 72 12
www.sibelco.be

SILICA SAND OF MOL M31 - M32 - M34

Technical Data

CHEMICAL ANALYSIS (XRF) %



	M31	M32	M34
SiO ₂	99.5	99.5	99.0
Fe ₂ O ₃	0.04	0.03	0.07
Al ₂ O ₃	0.20	0.20	0.60
TiO ₂	0.03	0.03	0.06
K ₂ O	0.03	0.05	0.30
CaO	0.01	0.01	0.02



SIBELCO
BENELUX

The above given information is based on mean values. The typical properties and chemical analyses are intended as examples and are not to be considered as substitutes for actual testing and analyses in those situations where properties and chemical compositions are critical factors. Sales and supplies will always be according to our general sales conditions.

CAS-Nr.: 14808-60-7

EINECS-Nr.: 238-878-4

MSDS available on request

ed.08

TDS.03.05.10 2010-12-09 2/2

Sibelco Benelux
De Zate 1 - BE-2480 Dessel
tel. +32 14 83 72 11 - fax +32 14 83 72 12
www.sibelco.be

Appendix E: MATLAB code

This Appendix contains the MATLAB code used to perform the preliminary calculations.

E.1. Main code

Parameters

```
%-
% Tank
DIM.H = 2.5;           %[m]
DIM.B = 2;             %[m]
DIM.L = 5;             %[m]
DIM.Dbed = 0.05;       %[m] sedimentation bed thickness
%
% Fluid
PAR.G = 9.81;          %[m/s2] Gravity constant
PAR.RHof = 1300;        %[kg/m3] Specific gravity fluid
PAR.MU = 100;          %[cp] Apparent viscosity
PAR.NU = ((PAR.MU/1000)/PAR.RHof); %[m2/s] Kinematic viscosity
PAR.Q = 1000;          %[l/min] Flow
%
% Particles
PAR.ii = 1000;          %[-] Amount of particle sizes
PAR.Dmin = 0.01;        %[mm] Minimum particle diameter
PAR.Dmax = 10;          %[mm] Maximum particle diameter
PAR.D = linspace(PAR.Dmin,PAR.Dmax,PAR.ii)/1000; %[m] Particle diameter range
PAR.Cs = 0.10;          %[%] Concentration solids
PAR.RHOp = 2650;        %[kg/m3] Specific gravity particles
PAR.S = PAR.RHOp/PAR.RHof; %[-] Relative density
%
```

Calculations

```
%-
% Terminal settling velocity calculations
[StokesVts,StokesRep] = StokesVts(PAR);
[ZankeVts,ZankeRep] = ZankeVts(PAR);
[ChengVts,ChengRep] = ChengVts(PAR);
[SadatVts,SadatRep] = SadatVts(PAR);
[ZhiyaoVts,ZhiyaoRep] = ZhiyaoVts(PAR);
[SchillerVts,SchillerRep] = SchillerVts(PAR,SadatVts);
%
% Hindered settling calculations
ZankeVslip = HinderedsettlingVc(PAR,ZankeVts,ZankeRep);
StokesVslip = HinderedsettlingVc(PAR,StokesVts,StokesRep);
ChengVslip = HinderedsettlingVc(PAR,ChengVts,ChengRep);
SadatVslip = HinderedsettlingVc(PAR,SadatVts,SadatRep);
ZhiyaoVslip = HinderedsettlingVc(PAR,ZhiyaoVts,ZhiyaoRep);
SchillerVslip = HinderedsettlingVc(PAR,SchillerVts,SchillerRep);
%
%Surface loading q
VAR.Q = (PAR.Q/1000)/60;          %[m3/s]
VAR.V0 = VAR.Q/(DIM.H*DIM.B);     %[m/s] horizontal flow
VAR.q = VAR.Q/(DIM.B*DIM.L);      %[m/s] surface loading
%
```

Tank Reynolds Number check

```
%-
% Hydraulic radius tank
VAR.R = (DIM.B*DIM.H)/(2*(DIM.B+DIM.H));
% Reynolds Number tank
VAR.ReTank = (VAR.V0*VAR.R)/PAR.NU;
if VAR.ReTank < 2000
    PLOT.Re = ['The tank flow is LAMINAR Re = ', num2str(VAR.ReTank)];
    disp(PLOT.Re)
elseif 2000 <= VAR.ReTank <= 4000
    PLOT.Re = ['The tank flow is in the TRANSITION zone Re = ', num2str(VAR.ReTank)];
    disp(PLOT.Re)
elseif VAR.ReTank > 4000
    PLOT.Re = ['The tank flow is TURBULENT Re = ', num2str(VAR.ReTank)];
end
%
```

Stability of flow check

```
%-
% Froude number Fr
VAR.Fr = ((VAR.V0^2)/PAR.G)*VAR.R;
if VAR.Fr >= 1*10^-5
    PLOT.Fr = ['The tank flow is STABLE Fr = ', num2str(VAR.Fr)];
    disp(PLOT.Fr)
elseif VAR.Fr < 1*10^-5
    PLOT.Fr = ['The tank flow is UNSTABLE Fr = ', num2str(VAR.Fr)];
    disp(PLOT.Fr)
end
%
```

Bottom scour check

```
%-
% Critical scour velocity [m/s]
VAR.Vsc = sqrt((40/3)*((PAR.RHOp-PAR.RHOf)/PAR.RHOf)*PAR.G*PAR.D);
for ii = 1:PAR.ii
    if VAR.Vsc(ii) <= VAR.V0
        PLOT.Vsc = ['Bottom scour DOES occur for particles < ', num2str(PAR.D(ii))];
        break
    elseif VAR.Vsc(ii) > VAR.V0
        PLOT.Vsc = 'Bottom scour DOES NOT occur Vsc > V0';
    end
end
%
```

E.2. Functions

Stokes terminal settling velocity function

```
function [Vts,Rep] = StokesVts(PAR)
%
% Terminal settling velocity [m/s]
Vts = (1/18)*(((PAR.RHOp-PAR.RHOf)*PAR.G*PAR.D.^2)/(PAR.MU/1000));
%
% Particle Reynolds Number [-]
Rep = (Vts.*PAR.D)/(PAR.NU);
%
end
```

Zanke terminal settling velocity function

```
function [Vts,Rep] = ZankeVts(PAR)
%
% Terminal settling velocity [m/s]
Vts = ((10*PAR.NU)./PAR.D).*((1+(0.01*(((PAR.S-1)*PAR.G*PAR.D.^3)/(PAR.NU^2))))).^0.5)-1);
%
% Particle Reynolds Number [-]
Rep = (Vts.*PAR.D)/(PAR.NU);
%
end
```

Cheng terminal settling velocity function

```
function [Vts,Rep] = ChengVts(PAR)
%
% Particle parameter [-]
Dstar = (((PAR.S-1)*PAR.G)/(PAR.NU^2))^(1/3)*PAR.D;
%
% Terminal settling velocity [m/s]
Vts = ((PAR.NU*(sqrt(25+(1.2*(Dstar.^2)))-5).^1.5))./PAR.D;
%
% Particle Reynolds Number [-]
Rep = (Vts.*PAR.D)/PAR.NU;
%
end
```

Sadat et al terminal settling velocity function

```
function [Vts,Rep] = SadatVts(PAR)
%
% Particle parameter [-]
Dstar = (((PAR.S-1)*PAR.G)/(PAR.NU^2))^(1/3)*PAR.D;
%
Vts = zeros(1,PAR.ii);
Rep = zeros(1,PAR.ii);
%
for ii = 1:PAR.ii
    if Dstar(ii) <= 10
        % Terminal settling velocity [m/s]
        Vts(ii) = ((0.033*PAR.NU)/PAR.D(ii))*(((PAR.D(ii)^3*PAR.G*(PAR.S-1))/(PAR.NU^2))^0.963);
    elseif Dstar(ii) > 10
        % Terminal settling velocity [m/s]
        Vts(ii) = ((0.51*PAR.NU)/PAR.D(ii))*(((PAR.D(ii)^3*PAR.G*(PAR.S-1))/(PAR.NU^2))^0.553);
    end
    % Particle Reynolds Number [-]
    Rep(ii) = (Vts(ii).*PAR.D(ii))/(PAR.NU);
end
end
```

Zhiyao et al terminal settling velocity function

```
function [Vts,Rep] = ZhiyaoVts(PAR)
%
% Particle parameter [-]
Dstar = (((PAR.S-1)*PAR.G)/(PAR.NU^2))^(1/3)*PAR.D;
%
% Terminal settling velocity [m/s]
Vts = ((PAR.NU./PAR.D).*(Dstar.^3)).*((38.1+(0.93*(Dstar.^(12/7))))).^(-7/8);
%
% Particle Reynolds Number [-]
Rep = (Vts.*PAR.D)/PAR.NU;
end
```

Schiller and Naumann terminal settling velocity function

```
function [Vts,Rep] = SchillerVts(PAR,StokesVts)
%
% First iteration
% Particle Reynolds Number [-]
Rep1 = (StokesVts.*PAR.D)/(PAR.NU);
%
Vts2 = zeros(1,PAR.ii);
%
for ii = 1:PAR.ii
    if Rep1(ii) <= 1000
        %Drag coefficient [-]
        Cd = (24/Rep1(ii))*(1+0.15*Rep1(ii)^0.687);
    elseif Rep1(ii) > 1000
        %Drag coefficient [-]
        Cd = 0.44;
    end
    %Terminal settling velocity [m/s]
    Vts2(ii) = sqrt(PAR.D(ii)*((4*PAR.G*(PAR.RHOp-PAR.RHOf))/(3*Cd*PAR.RHOf)));
end
% Second iteration
% Particle Reynolds Number [-]
Rep2 = (Vts2.*PAR.D)/(PAR.NU);
%
Vts3 = zeros(1,PAR.ii);
%
for ii = 1:PAR.ii
    if Rep2(ii) <= 1000
        %Drag coefficient [-]
        Cd = (24/Rep2(ii))*(1+0.15*Rep2(ii)^0.687);
    elseif Rep2(ii) > 1000
        %Drag coefficient [-]
        Cd = 0.44;
    end
    %Terminal settling velocity [m/s]
    Vts3(ii) = sqrt(PAR.D(ii)*((4*PAR.G*(PAR.RHOp-PAR.RHOf))/(3*Cd*PAR.RHOf)));
end
% Third iteration
% Particle Reynolds Number [-]
Rep3 = (Vts3.*PAR.D)/(PAR.NU);
%
Vts4 = zeros(1,PAR.ii);
%
for ii = 1:PAR.ii
    if Rep3(ii) <= 1000
        %Drag coefficient [-]
        Cd = (24/Rep3(ii))*(1+0.15*Rep3(ii)^0.687);
    elseif Rep3(ii) > 1000
        %Drag coefficient [-]
        Cd = 0.44;
    end
    %Terminal settling velocity [m/s]
    Vts4(ii) = sqrt(PAR.D(ii)*((4*PAR.G*(PAR.RHOp-PAR.RHOf))/(3*Cd*PAR.RHOf)));
end
```

```

% Fourth iteration
% Particle Reynolds Number [-]
Rep4 = (Vts4.*PAR.D)/(PAR.NU);
%
Vts5 = zeros(1,PAR.ii);
%
for ii = 1:PAR.ii
    if Rep4(ii) <= 1000
        %Drag coefficient [-]
        Cd = (24/Rep4(ii))*(1+0.15*Rep4(ii)^0.687);
    elseif Rep4(ii) > 1000
        %Drag coefficient [-]
        Cd = 0.44;
    end
    %Terminal settling velocity [m/s]
    Vts5(ii) = sqrt(PAR.D(ii)*((4*PAR.G*(PAR.RHOp-PAR.RHOf))/(3*Cd*PAR.RHOf)));
end
% Fifth iteration
% Particle Reynolds Number [-]
Rep5 = (Vts5.*PAR.D)/(PAR.NU);
%
Vts = zeros(1,PAR.ii);
Rep = zeros(1,PAR.ii);
%
for ii = 1:PAR.ii
    if Rep5(ii) <= 1000
        %Drag coefficient [-]
        Cd = (24/Rep5(ii))*(1+0.15*Rep5(ii)^0.687);
    elseif Rep5(ii) > 1000
        %Drag coefficient [-]
        Cd = 0.44;
    end
    %Terminal settling velocity [m/s]
    Vts(ii) = sqrt(PAR.D(ii)*((4*PAR.G*(PAR.RHOp-PAR.RHOf))/(3*Cd*PAR.RHOf)));
    %Particle Reynolds Number [-]
    Rep(ii) = (Vts(ii).*PAR.D(ii))/(PAR.NU);
end
end

```

Richardsson & Zaki hindered settling Function

```

function [Vslip] = HinderedsettlingVc(PAR,Vts,Re)
%
Vslip = zeros(1,PAR.ii);
%
for ii = 1:PAR.ii
    if Re(ii) <= 0.2
        beta = 4.65;
    elseif 0.2 < Re(ii) <= 1
        beta = 4.35*Re(ii)^-0.03;
    elseif 1 < Re(ii) <= 200
        beta = 4.45*Re(ii)^-0.1;
    elseif Re(ii) > 200
        beta = 2.39;
    end
    Vslip(ii) = ((1-PAR.Cs)^beta)*Vts(ii);
end
%
end

```